



UNIVERSITAT DE BARCELONA

Investigation on force detection methods for optical trapping and sensing inside living cells

Josep Mas Soler

ADVERTIMENT. La consulta d'aquesta tesi queda condicionada a l'acceptació de les següents condicions d'ús: La difusió d'aquesta tesi per mitjà del servei TDX (www.tdx.cat) i a través del Dipòsit Digital de la UB (diposit.ub.edu) ha estat autoritzada pels titulars dels drets de propietat intel·lectual únicament per a usos privats emmarcats en activitats d'investigació i docència. No s'autoritza la seva reproducció amb finalitats de lucre ni la seva difusió i posada a disposició des d'un lloc aliè al servei TDX ni al Dipòsit Digital de la UB. No s'autoritza la presentació del seu contingut en una finestra o marc aliè a TDX o al Dipòsit Digital de la UB (framing). Aquesta reserva de drets afecta tant al resum de presentació de la tesi com als seus continguts. En la utilització o cita de parts de la tesi és obligat indicar el nom de la persona autora.

ADVERTENCIA. La consulta de esta tesis queda condicionada a la aceptación de las siguientes condiciones de uso: La difusión de esta tesis por medio del servicio TDR (www.tdx.cat) y a través del Repositorio Digital de la UB (diposit.ub.edu) ha sido autorizada por los titulares de los derechos de propiedad intelectual únicamente para usos privados enmarcados en actividades de investigación y docencia. No se autoriza su reproducción con finalidades de lucro ni su difusión y puesta a disposición desde un sitio ajeno al servicio TDR o al Repositorio Digital de la UB. No se autoriza la presentación de su contenido en una ventana o marco ajeno a TDR o al Repositorio Digital de la UB (framing). Esta reserva de derechos afecta tanto al resumen de presentación de la tesis como a sus contenidos. En la utilización o cita de partes de la tesis es obligado indicar el nombre de la persona autora.

WARNING. On having consulted this thesis you're accepting the following use conditions: Spreading this thesis by the TDX (www.tdx.cat) service and by the UB Digital Repository (diposit.ub.edu) has been authorized by the titular of the intellectual property rights only for private uses placed in investigation and teaching activities. Reproduction with lucrative aims is not authorized nor its spreading and availability from a site foreign to the TDX service or to the UB Digital Repository. Introducing its content in a window or frame foreign to the TDX service or to the UB Digital Repository is not authorized (framing). Those rights affect to the presentation summary of the thesis as well as to its contents. In the using or citation of parts of the thesis it's obliged to indicate the name of the author.

Memòria de tesi presentada per a l'obtenció del títol de
doctor

Programa de doctorat: FÍSICA

“Investigation on force detection methods for optical
trapping and sensing inside living cells”



UNIVERSITAT DE
BARCELONA

Dotorand: Josep Mas Soler

Directors: Dra. Estela Martín Badosa

Dr. Mario Montes Usategui

Tutor: Dr. José Luis Morenza Gil

Departament de Física Aplicada

Universitat de Barcelona

Investigation on force detection methods for
optical trapping and sensing inside living cells

Josep Mas Soler

Barcelona, Setembre de 2016

Resum en Català

Les pinces òptiques són una eina no invasiva, basada totalment en la força de la llum, que permet atrapar i manipular objectes microscòpics sense necessitat d'establir-hi contacte físic [1]. Van ser descobertes per Arthur Ashkin a la dècada del 1970, quan va observar que un feix de llum podia accelerar partícules microscòpiques, o confinar el seu moviment utilitzant un segon feix contrapropagant. Uns anys més tard va descobrir la possibilitat de crear una trampa òptica utilitzant un sol feix de llum fortament focalitzat. Aquesta configuració de feix únic és la que s'ha extès més al llarg de les últimes dècades, per la feilitat amb que es pot compatibilitzar amb tècniques de microscopia avançada, i ha trobat nombroses aplicacions en l'àmbit de la biofísica i la biomedicina [2]

El principi de funcionament es basa en l'intercanvi de moment entre la radiació i els objectes materials. Qualsevol canvi en la direcció del feix de llum (o part d'aquest) en travessar la mostra es tradueix en una força de reacció sobre l'objecte físic amb el qual ha interaccionat. La pressió de radiació no té un efecte apreciable en objectes macroscòpics, però és capaç de provocar efectes significatius en objectes microscòpics, amb poca inèrcia, fent forces de l'ordre dels picoNewtons.

Un dels avenços en el camp és la introducció d'elements dinàmics per tal de poder manipular objectes a temps real. En particular l'holografia òptica permet generar patrons de trampes arbitraris, que s'adaptin a les necessitats de cada experiment. En el capítol 2 presentem un muntatge de pinces òptiques hologràfiques i demostrem la utilitat d'un nou algoritme híbrid per a la generació d'hologrames a temps real. En resum, el mètode permet utilitzar hologrames prèviament calculats amb mètodes iteratius (lents, però molt eficients), i multiplexar-los en espai utilitzant màscares aleatòries. El resultat és que es poden moure blocs de trampes rígids a temps real, sense necessitat de re-calcular tot l'hograma, cosa que suposa un avantatge per a experiments de manipulació on intervinguin grups rígids de trampes.

A part d'atrapar i manipular objectes, les pinces òptiques també es poden fer servir per mesurar forces, de forma semblant a un dinamòmetre. Quan un objecte és atrapat per un feix gaussià focalitzat, la força que experimenta és proporcional a la distància respecte del centre de la trampa (per un cert rang de posicions). Hom pot llavors mesurar forces en funció de la posició. El principal repte és que la constant d'atrapament (el que seria la constant de la molla en un dinamòmetre tradicional) depèn de l'objecte atrapat (índex

de refracció, mida,...) i altres condicions particulars de l'experiment (longitud d'ona, obertura numèrica, aberracions del feix,...). Això fa que cada cop que es vulguin fer mesures de força amb un objecte concret calgui calibrar la constant de la trampa.

Existeixen nombrosos mètodes per fer-ho, ja sigui aplicant forces viscoses conegudes i observant el desplaçament de l'objecte atrapat, o analitzant el moviment Brownià de la partícula atrapada, però tots els mètodes estàndard estan pensats per medis purament viscosos. Això no és un impediment per experiments in vitro amb molta precisió, però suposa una barrera per fer mesures de força en entorns més complexos, com ara una cèl.lula, on no hi ha cap mètode sòlid establert per calibrar la força de la trampa.

Recentment han sorgit mètodes alternatius que es podrien potencialment aplicar en experiments in vivo. Un dells és el mètode actiu-passiu de calibració de pinces òptiques en medis viscoelàstics.[3, 4]. Aquest mètode, basat en el Fluctuation Dissipation Theorem (FDT) combina mesures passives del moviment brownià de la partícula atrapada, amb mesures actives on s'aplica una perturbació controlada (típicament sinusoidal) al mateix temps que s'analitza la resposta de l'objecte atrapat. Combinant aquestes mesures es possible no només determinar la constant d'atrapament de la trampa, sinó també les propietats viscoelàstiques del medi.

Donat que el citoplasma cel·lular té un comportament viscoelàstic, resulta natural intentar aplicar el mètode actiu-passiu en aquest entorn per tal de possibilitar les mesures de força a l'interior cel·lular. Això és el que es presenta en el capítol 3 d'aquesta tesi, on s'aplica per primera vegada el mètode actiu-passiu en vesícules lipídiques atrapades a l'interior de cèl.lules de llevat (*S. Pombe*). En aquest capítol es descriuen els diferents passos a seguir per aplicar el mètode i els detalls d'anàlisi de dades, amb diverses comprovacions per assegurar que el mètode és vàlid en un entorn biològic. Els resultats són satisfactoris, mostrant mesures de la constant d'atrapament per diferents objectes, i paràmetres viscoelàstics del citoplasma comparables a altres valors de la literatura.

Un segon mètode potencialment aplicable en cèl.lules vives és el de mesura de moments [5, 6, 7]. Aquest mètode ha estat validat en pinces de feix únic pel nostre grup, i permet fer mesures de força sense haver-se de preocupar de calibrar la trampa. La raó és que el sistema mesura el canvi total en el moment del feix, i per tant directament la força òptica. Aquest mètode ha estat validat per una gran varietat d'objectes de mides i índex de refracció diferents, i és potencialment aplicable també a l'interior cel·lular, sempre que les pèrdues de llum i la dispersió degut a les estructures de la cèl.lula no siguin un problema.

Per tal de validar la possibilitat de fer mesures a l'interior cel·lular amb aquest mètode, en el capítol 4 es presenten una sèrie d'experiments en cèl.lules A549 on s'utilitza el mètode de moments i el mètode actiu-passiu en un mateix sistema. Els resultats obtinguts per una multitud de grànuls lipídics a l'interior cel·lular mostren com la constant de calibració es del sistema es manté estable a l'interior cel·lular, i pràcticament independent de l'objecte atrapat. Amb això queda provat que el mètode de moments és vàlid a l'interior cel·lular.

Finalment, en el capítol 5, s'aborda un problema concret de biofísica cel·lular,

com és la mesura de la força màxima de motors moleculars. Aquests motors, que converteixen energia química en treball mecànic a l'interior de les cèl·lules, han estat àmpliament estudiats *in vitro*, però poques vegades s'han pogut fer mesures de força en el seu entorn natural (la cèl·lula) per falta d'una tècnica de mesura de forces fiables. En aquest capítol mostrem que és possible mesurar forces de motors moleculars a l'interior cel·lular, i els resultats són comparables a altres estudis de forces de motors.

Amb aquest treball, es demostra que fer mesures a l'interior cel·lular és possible, i que els mètodes utilitzats, basats en principis teòrics totalment diferents, són consistents entre ells.

Abstract

Optical Tweezers (OT) are a light-based non-invasive tool that has played an important role during the last decades in the field of biophotonics. Optical trapping and micromanipulation of microscopic objects is nowadays a possibility, with the capability of measuring forces acting on the trapped particle (in the piconewton range), in combination with advanced optical microscopy techniques. OT have found numerous applications in the field of biophysics, and more specifically in molecular motor studies. One of the open challenges in the field is measuring molecular motor forces in their natural in vivo environment: the interior of living cells. Due to the complex mechanical properties of the cell cytoplasm standard trap force calibration methods do not apply in this environment.

In this thesis we investigate two recent optical force calibration methods: active-passive calibration in viscoelastic media, and direct force measurements via light momentum changes. The two methods are tested and cross-validated inside living cells, an application involving intracellular molecular motor stall force measurements is demonstrated. The obtained results prove the possibility of measuring forces inside the cell cytoplasm with holographic tweezers, even with an object-independent trap force calibration when the conditions for the momentum-based technique are fulfilled.

We also present an algorithm for manipulating groups of optical traps with minimal computational cost, using random mask multiplexing combined with iterative computer-generated holograms for dynamic holographic optical tweezers.

Contents

1	Introduction	8
1.1	Forces in Optical Tweezers	10
1.1.1	Rayleigh regime	10
1.1.2	Ray optics regime	11
1.2	The optical trap as a force sensor	14
1.2.1	The harmonic optical trap	14
1.2.2	Standard trap stiffness calibration methods	14
1.3	The challenge of force sensing inside biological cells	15
1.3.1	<i>In situ</i> intracellular calibrations: active-passive calibration in viscoelastic media	16
1.3.2	Momentum-based force detection: towards a sample-independent calibration	16
1.4	Scope of the thesis	17
2	Holographic micromanipulation	18
2.1	Micromanipulation with multiple traps	18
2.1.1	Holographic optical tweezers	19
2.1.2	Experimental setup	21
2.2	Standard algorithms for hologram computation	22
2.2.1	Iterative approach	22
2.2.2	Prisms-and-lenses	23
2.2.3	Random mask multiplexing	24
2.2.4	Theoretical efficiency of the random mask algorithm	24
2.3	New hybrid algorithm combining Random Mask encoding with iterative methods	26
2.3.1	Principle of operation	26
2.3.2	User interface	27
2.3.3	Translation and rotation of groups of trapped microbeads	28
2.3.4	Quantifying hologram efficiency and trap stiffness	28
2.4	Conclusions	31
3	Active-passive calibration in yeast	32
3.1	Theory of active-passive calibration in viscoelastic media	33

3.1.1	Description of an optically trapped particle in a viscoelastic media	33
3.1.2	Central assumption, and requirements for trap calibration	35
3.1.3	Trap calibration	35
3.1.4	Viscoelastic parameters	37
3.2	Experimental methods	38
3.2.1	Optical trapping setup	38
3.2.2	<i>S. Pombe</i> samples	39
3.2.3	Preliminary equipment characterization	40
3.2.4	Protocol for active-passive calibration experiments	40
3.2.5	Comments on amplitude choice for β calibration	43
3.3	Data analysis	43
3.3.1	Data loading and preliminary checks	44
3.3.2	Beta calibration	45
3.3.3	Passive measurements	47
3.3.4	Active measurements: checking and fitting	49
3.3.5	Trap calibration and viscoelastic parameters	52
3.4	Results for different lipid granules	54
3.4.1	Calibrated trap parameters	54
3.4.2	Frequency dependence	57
3.4.3	Power dependence	58
3.4.4	G moduli	58
3.5	Conclusions	59
4	Momentum method validation in A549 cells	61
4.1	Introduction	61
4.2	Experimental system for momentum-based force measurements and active-passive calibration	62
4.2.1	System requirements for momentum-based force measurements	62
4.2.2	Experimental setup	64
4.2.3	Compatibility of imaging and force detection	67
4.2.4	Parameters of the momentum-based detection system	68
4.2.5	Notes on active driving in AP calibration	69
4.2.6	Data acquisition and analysis	70
4.2.7	Preliminary considerations for force measurements in heterogeneous media	71
4.3	Active-passive calibrations in A549 cells	73
4.3.1	Cell sample preparation	73
4.3.2	Intracellular trapping of Lipid Droplets	74
4.3.3	Active-passive calibration in trapped LDs	75
4.3.4	Measured trap parameters (α , β , κ)	76
4.3.5	Asymmetry in trap parameters	77
4.3.6	Dependence on particle size	78
4.3.7	Measured PSD signal offsets	79
4.4	Validation of DF method in A549 cells	80

4.4.1	Low frequency noise in A549 cells	81
4.4.2	AP calibrations at higher frequencies	82
4.4.3	Evidence of biological activity	83
4.5	Comments on two-method cross-validation in A549	86
5	Molecular motor force measurements	87
5.1	Molecular motors and intracellular transport	87
5.1.1	Motor studies on <i>in vitro</i> optical trapping assays	88
5.1.2	The complexity of motor activity <i>in vivo</i>	88
5.2	The stall force experiment	91
5.3	Stall force measurements in A549 cells	94
5.3.1	Intracellular traffic in A549 cells	94
5.3.2	Comments on trapping power	95
5.3.3	Nocodazole assay	96
5.3.4	Experiment protocol	97
5.4	Data analysis	98
5.4.1	Automatic stall event inspection	98
5.4.2	Identification of clear motor-stalling events	100
5.4.3	Identification of one-dimensional experiments	101
5.4.4	Baseline correction in stall force measurements	103
5.4.5	Comments on global baseline fluctuations	104
5.4.6	Evaluation of light losses	104
5.4.7	Estimation of error in stall force measurements	106
5.4.8	Determination of inward/outward directions of stall events	107
5.4.8.1	Cell polarity	108
5.4.8.2	Relative orientation of PSD and CCD axis	108
5.4.8.3	Classification of inward/outward events	110
5.5	Results	110
5.5.1	Stall force measurements	110
5.5.2	Inward/outward events	112
5.5.3	Evidences of multiple motors in force measurements	115
5.6	Further comments on intracellular force measurements	119
6	Final conclusions	120
	Bibliography	126

Chapter 1

Introduction

Nature has always been a source of inspiration and wondering for humans. It is through observation, experimentation and creative thinking that scientific knowledge about our universe builds up across the centuries in different scientific disciplines. With the advances in our understanding of the world, new tools arise, which in turn allow us to explore even further, pushing the limits of knowledge.

Optics has been an important part of this journey, with light being not only an interesting subject of study *per se*, but also an instrument to explore nature beyond what humans can physically sense. Since the 17th century telescopes allowed us to see further than ever, fundamentally changing our preconceived ideas about the universe, and microscopy allowed us to visualise structures smaller than what the human eye can resolve, from small organisms to unicellular bacteria, and subcellular structures.

Optical microscopy evolved in new forms of imaging seeking enhanced resolution and contrast, including fluorescence for targeted functional imaging, confocal arrangements for fine 3D sectioning, multiphoton excitation for increased contrast and penetration depth, PALM-STORM, STED, and structured illumination (SIM) for enhancing resolution beyond the original optical diffraction limit. Other techniques that can bring imaging capabilities to an even smaller scales are electron microscopy (TEM, SEM) and scanning probe techniques such as atomic force microscopy (AFM), scanning tunneling microscopy (STM) and near-field scanning optical microscopy (NSOM). It is nowadays possible to look not only at intracellular organelles and structures with very fine detail, but also down to single molecules and even individual atoms, expanding the window of what can be observed, studied, and eventually understood.

Besides, it is not only observation what brought science forward, but also the ability to touch and experiment with the physical world. Surprisingly we have been mainly spectators of the microscopic world for centuries, in a similar way as we observe the universe beyond our galaxy. It wasn't until 1970s that Arthur Ashkin discovered the possibility of gently pushing small material particles by means of radiation pressure [8], and later on demonstrated that it is possible to

stably trap dielectric particles with a single-beam geometry [9], using a tightly-focused laser beam. Optical Tweezers were born, and with them a new field full of possibilities with applications in several branches of science. Manipulation of microscopic objects is nowadays possible with this minimally invasive tool, which is entirely based on light.

Its applications span beyond optics, including physics of colloids and aerosols [10], atoms trapping [11], or life sciences. Biology found in optical tweezers a precision technique enabling a range of new experiments that were not possible beforehand [12, 13]. Contactless optical trapping and manipulation of biological samples can be achieved with minimal risk for the samples themselves, which can be kept in conditions of sterility while they are investigated with a gentle push of light.

Moreover, it is also possible to use optical tweezers as a force sensor with a typical range of forces within 0.1 to 100pN. This makes it ideal to quantify the forces involved in biophysical processes such as molecular motors dynamics [14, 15, 16, 17], protein conformational changes [18], or protein-protein binding interactions. Applications related to biomedical research are also on the rise, including assisted fecundation, immune cell studies [19], or investigation on intracellular traffic [2], which is linked to neurological problems such as Alzheimer's disease.

Apart from optical tweezers, other useful techniques for force sensing in the microscopic scale are Atomic Force Micorscopy (AFM) and Magnetic Tweezers [20]. These techniques complement optical tweezers, with specific advantages and drawbacks that make them suitable for different applications [21]. For intracellular experiments, both optical and magnetic tweezers are valid approaches, since they are contact-free techniques that may operate in the cell cytoplasm without disrupting the cellular membrane. Magnetic tweezers work over a broader force range (from 0.001 to 100pN), but rely on the internalization of paramagnetic beads to use as handles for force measurements [20]. On the other hand optical tweezers may directly use endogenous cellular organelles as handles for optical forces [22, 23, 24], but have limited forces. AFM can measure much higher forces than the rest (in the range of 10pN to 1nN), but its application is restricted to measurements in locations that are physically accessible, such as protein binding at the cellular membrane [25].

Different configurations exist for generating an optical trap. For example, two counter-propagating laser beams can be aligned to create a stable trap, where the pushing axial forces from each beam are compensated [8, 5]. On the other hand, a single-beam configuration is also valid for trapping, using a high numerical aperture beam [9]. This last approach is the most commonly used, since it can be easily adapted to work with advanced microscopy techniques, such as phase contrast or confocal microscopy. Optical tweezers can be hence be used for combined with high-quality imaging of the sample, which is specially useful for biological investigations.

1.1 Forces in Optical Tweezers

The principle behind optical trapping is the exchange of momentum between a light beam and a material object. Radiation pressure can accelerate small objects and, with the right geometry, constrain their movement within a confined region of the space (trap).

In order to understand the trapping behaviour observed in single-beam optical traps (or optical tweezers), there are analytical expressions for the trap force in two limit regimes: Rayleigh regime (for particles much smaller than the wavelength) and Ray optics regime (for particles much larger than the wavelength). In general, and specially for the intermediate size range (which is the most common case in practical applications) note that there is no simple analytical form to calculate the optical force. In these non-trivial cases, one could use Generalized Lorentz-Mie theory and its extensions[26] to numerically simulate light scattering on the trapped bead and calculate optical forces

1.1.1 Rayleigh regime

When the particle size is much smaller than the trapping wavelength, it can be modelled as dipole that scatters light from a beam with intensity profile $I(x, y, z)$. In that context, there is a gradient and a scattering force acting on the bead, which are respectively given by [27]:

$$\vec{F}_g = \vec{\nabla}[\vec{p} \cdot \vec{E}] = 2\pi \frac{n_1}{c} a^3 \frac{m^2 - 1}{m^2 + 2} \vec{\nabla} I(x, y, z) \quad (1.1)$$

$$\vec{F}_s = \frac{n_1}{c} \frac{8}{3} \pi k^4 a^6 \left[\frac{m^2 - 1}{m^2 + 2} \right]^2 I(x, y, z) \hat{z} \quad (1.2)$$

with n_1 the refractive index of the medium, $m = n_2/n_1$ the relative refractive index of the particle, a the radius of the particle, $k = 2\pi/\lambda$ (with λ being the laser wavelength), c the speed of light, and $I(x, y, z)$ the intensity profile of the beam. The combination of both force components creates a force field that may have a stable position close to the focus of the beam, as long as the gradient force is larger than the scattering force in the axial direction. For a Gaussian beam with beam waist ω_0 , this condition is only fulfilled when:

$$\frac{3\sqrt{3}}{128\pi^5} \left[\frac{m^2 - 1}{m^2 + 2} \right] \frac{\lambda^5}{a^3 \omega_0} \geq 1 \quad (1.3)$$

Hence, in order to achieve a stable trapping, the relative refractive index needs to be $m > 1$, and the beam waist small enough (i.e. high NA required). An example of a simulation,¹ in the Rayleigh regime, showing the bidimensional force field and the force profiles in the axial and transverse directions, is

¹Force field simulations were carried out with a custom-made applet for optical trap simulation, described in [28]

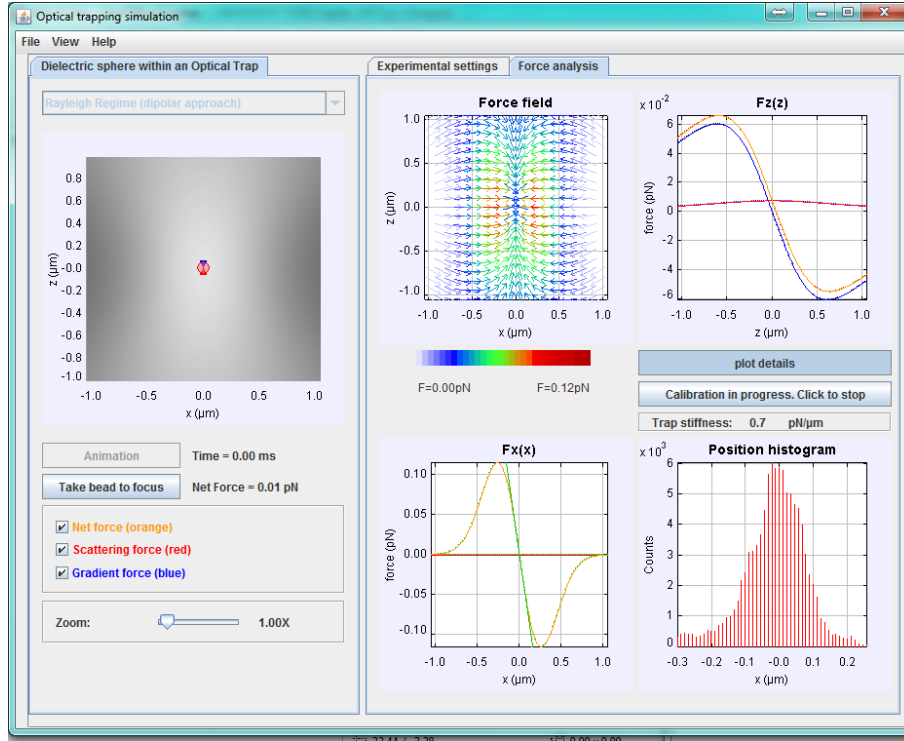


Figure 1.1: Force field in Rayleigh regime. The simulation parameters are $P = 100\text{mW}$, $a = 50\text{nm}$, $NA = 0.65$, $\lambda = 1064\text{nm}$, $n_1 = 1.33$, $n_2 = 1.58$. In the force curves, the different force components are shown, including gradient (blue), scattering (red) and total (orange) forces.

presented in Figure 1.1. A stable position close to the focus of the beam is observed in the force field. The restoring force behaviour is clear in the transverse and axial force curves, where the optical force force grows as the object position separates from the trap centre.

1.1.2 Ray optics regime

The ray optics regime (or Mie regime) applies when the particle is much larger than the wavelength of the trapping beam. In that case, the interaction can be described in terms of refraction and reflection of rays through the trapped object.

As seen in Figure 1.2, a single ray (propagating from lower to higher z coordinates) undergoes a change of direction due to refraction through a dielectric sphere. Because of the momentum conservation law, the observed change in the light momentum creates a reaction force on the particle of opposite sign. For comparison with the Rayleigh case, the resulting force can be decomposed

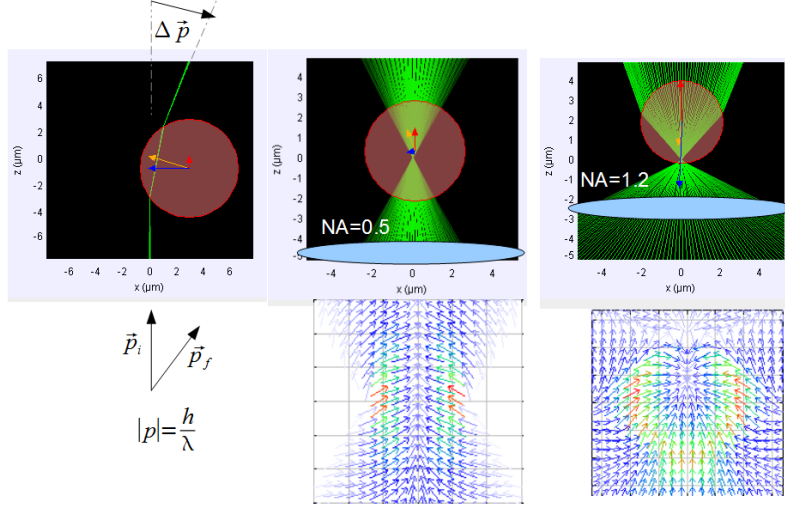


Figure 1.2: Ray tracing for a single ray, with the associated change of momentum, and force fields for low NA and high NA beams. The arrows in the ray diagram correspond to the gradient force (blue), scattering force (red) and total force (orange).

in a scattering component (parallel to the incident ray direction) and a gradient component (perpendicular to the incident ray direction). Then, for the full beam, the total force acting on the trapped sphere can be calculated by adding the force contributions from each ray.

Again, a trap is formed only when the gradient force is able to overcome the scattering force in the axial direction. Since the beams contributing most to the gradient force are the ones at high incidence angle, it is understandable that using a high NA favours the creation of a stable optical trap, whereas a low NA beam tend to push the particle away in the axial direction. This is illustrated in Figure 1.2 , showing examples of the force field generated by a low-NA beam (non-trapping) and a high-NA beam beam (trapping).

The force for each single ray on a spherical dielectric particle can be analytically described by [29]:

$$F_g = \frac{n_1 P}{c} \left[R \sin(2\theta_i) - T^2 \frac{\sin(2\theta_i - 2\theta_r) + R \sin(2\theta_i)}{1 + R^2 + 2R \cos(2\theta_r)} \right] \quad (1.4)$$

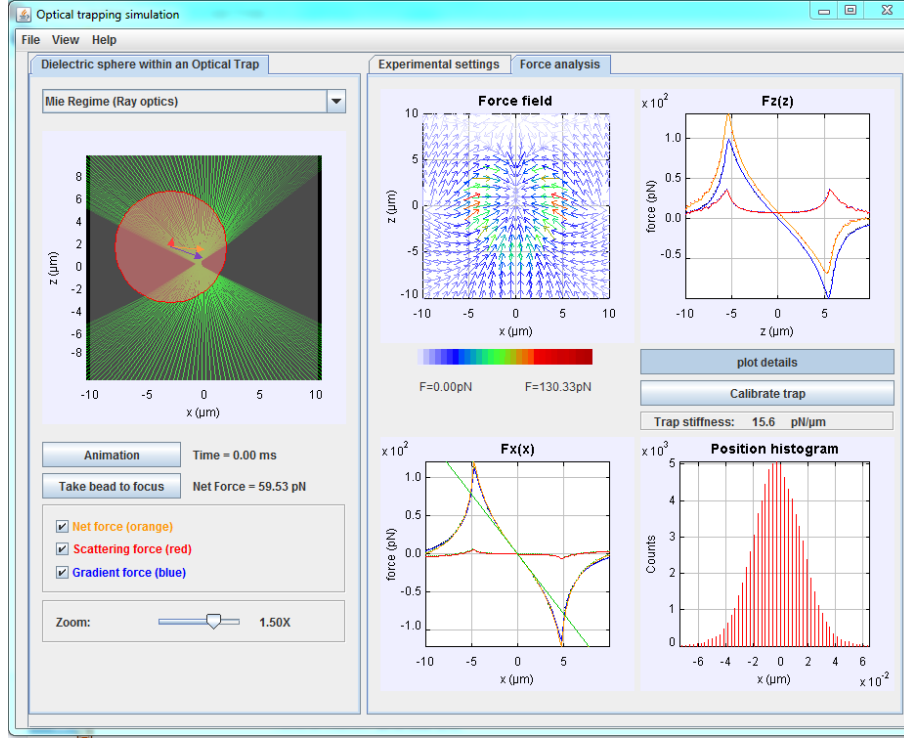


Figure 1.3: Simulation of optical forces in the ray optics regime. The parameters of the simulation are $P = 100mW$, $a = 5\mu m$, $NA = 1.2$, $\lambda = 1064nm$, $n_1 = 1.33$, $n_2 = 1.58$, and lens overfilling factor $\gamma = 1$ [28].

$$F_s = \frac{n_1 P}{c} \left[1 + R \cos(2\theta_i) - T^2 \frac{\cos(2\theta_i - 2\theta_r) + R \cos(2\theta_i)}{1 + R^2 + 2R \cos(2\theta_r)} \right] \quad (1.5)$$

where θ_i is the ray incidence angle at the surface of the sphere, θ_r the first refraction angle, R and T the Fresnel reflection and transmission coefficients, n_1 the refractive index of the media, P the power, and c the speed of light. The scattering component (F_s) points in the direction of the incident beam, while the gradient component (F_g) is perpendicular to it. Note that the analytical model includes the multiple reflections and refractions inside the sphere.

The total force on the microsphere can be calculated by adding the force contributions from all the rays forming the beam. A simulated example of the force field in the ray optics regime is shown in in Figure 1.3. Again, a stable position (trap centre) is observed and the force curves show a region with a restoring force, that would keep the particle trapped at an equilibrium position near the focus of the the beam.

1.2 The optical trap as a force sensor

1.2.1 The harmonic optical trap

Looking at the transverse force profiles $F_x(x)$ in Figures 1.1 and 1.3, for an optically-trapped microsphere in a Gaussian beam, one can see a linear region around the centre of the optical trap. In this range, the trap force can be fairly approximated by Hooke's law, with the restoring force growing linearly as the particle moves further from the equilibrium position.

$$F_x(x) = -\kappa_x(x - x_0) \quad (1.6)$$

Hence one can potentially use the trapped particle as a probe for measuring external forces acting on it. For this purpose, if the trap stiffness (κ_x) is known, any small particle position shifts with respect to the trap equilibrium position (x_0) can be directly converted into force units

The trap stiffness is, in general, strongly dependent on experimental parameters including laser power, wavelength, particle and medium refractive index, particle size, numerical aperture and aberrations of the beam. Due to some of the particle parameters not being accurately known in most applications, the trap stiffness needs to be explicitly calibrated for each trapped object.

In order to use the trap as a force sensor, once the trap stiffness is known, forces in the linear range can be quantified by measuring the relative position of the trapped bead with respect to the trap equilibrium position. Accurate particle positions are typically obtained with back-focal-plane interferometry [30, 31], using a fast detector such as a Quadrant Photodiode (typically working at 10kHz or more). The voltage to position conversion factor can be calibrated (e.g. scanning a stuck bead), and with that the signal from the sensor can be converted to positions and finally, to force.

Alternatively video acquisition may be used for parallel measurements with multiple traps, using particle tracking to measure changes in the trapped position. Video measurements are typically more demanding in terms of equipment, and the sampling frequency is typically at least an order of magnitude lower than with QPD or PSD devices. Also, camera recordings at high speed generate a huge amount of data, that may be unnecessary if one is just interested on the particle trajectory.

1.2.2 Standard trap stiffness calibration methods

Several methods exist for calibrating the trap stiffness for optically trapped particles in a purely viscous medium [30, 1, 32].

A simple approach is to apply controlled (viscous drag) forces on the trapped object, by making the medium flow at controlled speeds around the trap. In this way, the position of the bead can be recorded as a function of the known applied viscous forces, and with that the trap stiffness can be determined [33]. Note that this requires knowledge on the viscous properties of the medium and the particle size, so that the Stokes force ($F = 6\pi r\eta v$) is known.

Another possibility is the time-of-flight method [30], that looks at the trajectory of a particle falling into the trap, and uses it to reconstruct the trap potential. Again, for using this method the viscous properties of the medium and the particle size need to be known in advance.

A very simple approach is the analysis of the Brownian trajectories of the trapped particle, whose extent (σ_x) is directly related to the force of the trap, following the equipartition theorem:

$$\frac{1}{2}k_B T = \frac{1}{2}\kappa\sigma_x^2 \quad (1.7)$$

This method is straightforward to implement (only requires to measure the variance in the particle trajectory), and interestingly no knowledge about the viscosity of the medium or particle size is required. However, any system drifts or external noise adds up to the position variance, making the equipartition theorem more prone to underestimate the actual trap stiffness in the presence of noise.

A more refined method, also based on the Brownian motion of the trapped particle, is power spectrum analysis [34, 35]. The Fourier decomposition of the particle's thermal agitation typically results in a Lorentzian shape as a function of the frequency

$$S(f) = \frac{k_B T}{\gamma\pi^2(f_c^2 + f^2)} \quad (1.8)$$

The corner frequency relates to the trap stiffness $f_c = \kappa/2\pi\gamma$, where γ is the Stokes coefficient. The method is very accurate and robust against noise at specific frequencies (that can be excluded from the Lorentzian fit). However, it still relies on knowledge of the viscosity of the medium and particle size, which are necessary to retrieve the trap stiffness.

Finally, a modification of the power spectrum method with addition of stage driving is shown in [31]. In this case the trap stiffness is determined without need of previous knowledge on the medium viscosity, which is obtained as a side result of the calibration process.

1.3 The challenge of force sensing inside biological cells

The standard methods work well in purely viscous environments, but in some occasions one would be interested in measuring forces in complex environments. An example for this situation are optical trapping experiments inside biological cells. The cytoplasm of a living cell is a dense mixture of a viscous cytosol and more rigid/elastic structures (cytoskeleton, organelles, membranes...) giving the cell its mechanical consistency. In that context, the calibration methods described before do not hold, and other approaches are needed to be able to face the challenge of intracellular force measurements with the optical traps [14, 2].

One possible way to tackle this problem is performing trap force calibrations with purified organelles in a viscous buffer (where standard methods apply). If the refractive index of the buffer is properly tuned to mimic the cell cytoplasm one can in principle extrapolate the calibrated stiffness into the cell, taking into account phenomenological correlations. For example trap stiffness can be related to microscopy image contrast [36] or particle size [22, 37]. Synthetic microspheres of controlled refractive indexes and sizes (matching with lipid droplets parameters) can also be useful for external calibrations [38]. External particles may even be internalised by certain cell types (via phagocytosis) and used as intracellular handles for force measurements [39]. This sophisticated ways of quantifying the trap spring constant circumvent the lack of a proper method for calibrating the trap force in living cells, although an *in situ* calibration would be preferred for simplicity and for taking into account all the local conditions of the experiment *in vivo*.

For example, *ex situ* calibrations do not consider elements in the cell, like membranous structures in the path of the laser, that might introduce local optical aberrations affecting the actual trap stiffness. Also local variations in the cell refractive index around the trap due to the presence of cellular structures could introduce changes in the trapping strength that are not taken into account in measurements on a viscous buffer.

1.3.1 *In situ* intracellular calibrations: active-passive calibration in viscoelastic media

A method for calibrating optical traps in viscoelastic media was first theoretically developed [3] and later on experimentally demonstrated in an actin gel [4]. It consists of combining passive recordings of the Brownian motion of the trapped particle, and active measurements in which a controlled perturbation is applied to the system while the response on the trapped bead is monitored. Based on the Fluctuation Dissipation Theorem, the method is able to retrieve the trap stiffness, and characterise the viscoelastic parameters of the medium at the same time.

The active-passive method has been proposed as a possible way calibrating optical traps in the cellular cytoplasm. This idea is explored in chapter 3 of this thesis, where we apply it for the first time in a living system (*S. Pombe*). The possibility of calibrating the trap strength on optically trapped organelles in the intracellular environment paves the way for addressing future biophysical challenges directly in the cell, rather than synthetic *in vitro* experiments.

1.3.2 Momentum-based force detection: towards a sample-independent calibration

An alternative method that has the potential to be applied in complex media is the measurement of light-momentum changes [Smith2003], which requires the ability to detect momenta of the major part of the photons interacting with the sample to infer the net force exerted by the laser beam. Although this

is technically challenging, it has recently been compatibilized with single-beam optical traps by our group [Farré2010, Farré2012]. This method has been shown to be sample independent (with beads of different sizes and refractive index) and directly supplies the net optical force acting on any trapped object.

Considering that, one could potentially trap endogenous cellular organelles in the cytoplasm to measure forces acting upon them. However, the method may be sensitive to light losses and scattering at other structures in the path of the beam. Hence, a first step is to validate that the system calibration constant still holds inside a living cell. This is investigated in chapter 4.

1.4 Scope of the thesis

This thesis aims at paving the way for future intracellular force measurements, by demonstrating the possibility of using active-passive calibration or momentum-based force detection for performing quantitative force measurements inside living cells.

In chapter 2 we start by describing the holographic optical trapping system, and present a particular algorithm for the dynamic manipulation of groups of multiple traps with a minimum computational cost.

In chapter 3 we present the application of active-passive calibration method inside living *S. Pombe* cells, and describe the peculiarities found in living systems (as opposed to synthetic media) that need to be taken into account during the analysis process. Trap calibration results on a plurality of optically trapped lipid granules, are presented, together with the measured viscoelastic properties of the cellular cytoplasm.

In chapter 4 we use active-passive calibration to benchmark the momentum-based force measurements. The two independent methods, implemented here on the same experimental setup, are cross-validated for the first time inside living cells.

Finally, in chapter 5 we present an application of the momentum method for measuring molecular motor stall forces inside living cells. The experimental protocols, data analysis process and stall force results are presented and compared with the literature.

Chapter 2

Holographic manipulation of groups of optical traps

During the last decade holographic optical tweezers (HOT) have become a powerful tool for the dynamic manipulation of microscopic samples in three dimensions [40]. Computer generated holograms (CGH) are displayed on a spatial light modulator (SLM) in order to modify the complex amplitude of the trapping beam. Thus, the beam can be split, tilted or reshaped, and arbitrary three-dimensional patterns of light can be created. The modulated beam is usually focused into highly concentrated light spots by a high numerical aperture optical system. Each light spot can be used as an independent optical trap that exerts controlled forces on the sample.

In this chapter we describe first the interest of using multiple traps in optical tweezers, the standard algorithms for generating arbitrary trap patterns, and we finally propose a method [41] to manipulate rigid groups of optical traps in real time with a minimum computational effort.

2.1 Micromanipulation with multiple traps

The use of a plurality of optical traps instead of a single light spot allows one to trap more than one object at a time, similarly to a microscopic analogue to our hands and fingers. There is a growing need and interest in the use of more than one trap for micromanipulation, for example, in single-molecule biophysics [42]. Dumbbell assays requiring two independent traps are increasingly used for characterizing motor proteins [43], and a more sophisticated example is found in [44], where the preparation of a specific experiment requires that four traps are used to hold two DNA strands and wound one of them around the other.

There are different methods to generate multiple optical traps, either by combining independent laser sources into the objective lens, splitting a single laser beam into two orthogonally-polarized beams or creating interferometric

patterns of light spots from a single beam. Unfortunately, these solutions are either expensive, restricted to two traps or to fixed trap patterns, respectively.

By contrast, the most useful approaches for generic micromanipulation experiments are those offering a dynamic and versatile control over an arbitrary number of independent traps. For that purpose, one can use a time-sharing technique, which consists of a fast switching of the laser beam between different positions in the sample (as many as the number of desired optical traps). If the switching is performed quickly enough (faster than the diffusion time-scale of the particles, so that they are not affected by the flickering), the trapped objects will behave in practice as in a constant laser spot [1, 32]. Time-sharing can be implemented with different devices, such as acousto-optic deflectors [33], scanning galvanometer mirrors or electro-optic deflectors [45]. Their performance in terms of speed, position repeatability, range of deflection angles, beam pointing stability or optical efficiency is uneven, each of them being strong in certain aspects and weak in others [32]. High-speed beam deflection for time-shared optical traps is usually computer-controlled, and the intensity and 2D-position of each optical trap can be tuned independently. However, the number of traps cannot be increased indefinitely, since the visitation frequency for each trap should be high enough to prevent particles from escaping. Although 1000 visitations per second per trap are adequate in most cases, in [46] they show that a visitation rate of 10 kHz per trap would be necessary for bringing the diffusion distance between laser visitations down to 1 nm, thus limiting the number of traps to only six in that case. Such accuracy is convenient in precise experiments like molecular motor studies.

2.1.1 Holographic optical tweezers

A recent, innovative approach to generate multiple traps is the use of digital holography for spatially modulating the laser beam, adding in-depth control of the multiple traps in contrast to the 2D positioning performed by deflecting-only devices. Holography was first introduced in the field of optical micromanipulation in 1999 [47], by adding a liquid crystal spatial light modulator (SLM) in the optical path of the trapping laser. The SLM is a reconfigurable device allowing the modulation of the phase and/or amplitude of an incident light wavefront at each pixel of the display. In this way, one can control, for example, the tilt and convergence of the output wave, or split the beam into many beams at different angles. An illustrative example is shown in Figure 2.1, where two different phase masks produce an effect similar to a prism or a lens, making the beam focus shift laterally or axially.

Consequently, custom positioning of an arbitrary number of light spots in the sample plane (after the focusing, objective lens) is achieved, and thus microparticles can be trapped and manipulated in 3D, with no need for mechanical movements in the optical elements of the setup. So far, holographic optical tweezers have found abundant applications in microfluidics, biophysics, colloidal studies, and 3D micromanipulation experiments in general [48]. There are even recent perspectives on using an automated holographic optical tweezers mod-

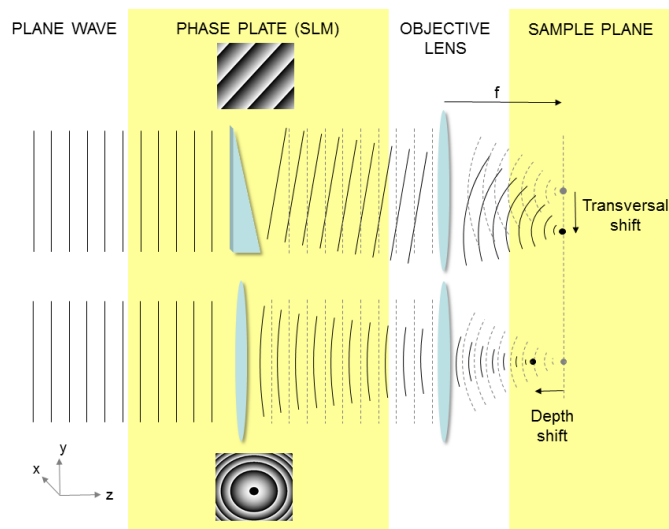


Figure 2.1: Illustration of two phase masks: a linear phase and a parabolic phase, which produce an effect equivalent to a prism and a lens respectively. Following the properties of the optical Fourier transform carried out by the objective lens, these phase masks produce a spatial shift in the focal spot, either laterally (for the linear grating) or axially (for the spherical phase mask).

ule for colloidal studies in the International Space Station, a high-vibration, microgravity environment. [49].

Another advantage brought by holography is the possibility to correct for optical aberrations to improve trapping performance [50]. Furthermore, twin traps with different focusing depths can be generated [51] allowing single beam optical tweezers to trap even at low numerical apertures. Another interesting application is the creation of optical traps with exotic shapes and properties, like Laguerre-Gaussian beams, which carry light orbital angular momentum that makes the trapped particles rotate within a light vortex [48]. Advances of the technique in the last decade have led to the implementation of devices with convenient interfaces, which make micromanipulation as simple as sliding the operator's hands over a multitouch screen [52], allowing us to reach and operate in the microscopic world as easily as in the macroscopic world.

In general, holographic optical tweezers can be used as a tool to assemble small objects such as microbeads, rods, cells, nano objects and indeed combinations of them [53, 54]. Several micromanipulation experiments involve grabbing, moving and rotating relatively large objects, which must be held from different points to achieve stable trapping with a controlled orientation. For example, in [55] a cell is suspended with several optical traps for immobilizing and performing controlled positional changes during *in vivo* imaging with Raman spectroscopy. In some cases more than one single object must be controlled independently e.g. in [56] where non-trivial structures are built from several semiconductor nanowires by holding, cutting, translating, rotating and fusing them with holographic optical tweezers. This requires a dynamic control over the position and orientation of each part. In fact, the grouping of holographic optical traps into rigid assemblages that are then operated as a single object is a basic functionality included in many advanced interfaces, such as those in [57, 52]. However, these group operations are not optimized at the algorithm level and always involve the re-computation of the whole hologram. The hybrid method we present below is a step forward on that direction.

2.1.2 Experimental setup

The holographic tweezers setup we used for the experiments presented in this chapter was built around a commercial inverted microscope (Nikon Eclipse TE-2000E). The beam of an Ytterbium fiber laser (IPG YLM-5-1064-LP) is expanded by a telescope to overfill a reflective phase-only SLM (Hamamatsu X10468-03) and it is then directed into the microscope through an epi-fluorescence port, where a dichroic mirror sends the beam towards the sample through an oil-immersion objective (Nikon Plan Fluor 100X, 1.30 NA).

A telescope in a 4-f configuration conjugates the SLM plane (12x16mm liquid-crystal screen) with the back aperture of the microscope objective. The telescope is designed so that the beam slightly overfills the entrance pupil of the objective to ensure that the high-NA part of the beam has sufficient power for a more stable trapping in the axial direction. Further details can be found in [58]. A sketch of the setup is shown in Figure 2.2.

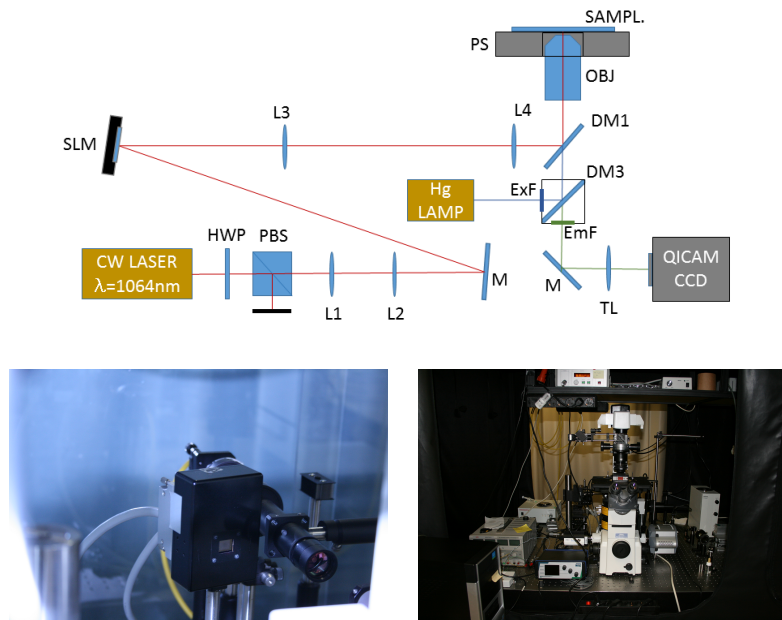


Figure 2.2: Holographic optical tweezers setup, and a photograph of a Spatial Light modulator

2.2 Standard algorithms for hologram computation

Several computational algorithms are available for calculating Computer Generated Holograms (CGH) for optical trapping. The efficiency, uniformity and speed requirements [59] of each experiment may determine the choice of one particular algorithm or another.

2.2.1 Iterative approach

Some of the most widely used methods for computing phase holograms do not come as a closed-form solution but are iterative, e.g. the Gerchberg-Saxton (GS) algorithm [60] or the Direct-Search algorithm [61].

In particular, the Gerchberg-Saxton algorithm produces a hologram by sequentially propagating the field from the sample plane to the Fourier plane and vice-versa, using digital Fourier transforms. The start field at the sample plane is typically a mask with random phases and an amplitude profile corresponding to the desired trap pattern. The principle of the method consists of imposing the target amplitude profile at the sample plane, and forcing a phase-only mask in Fourier space (resetting amplitude constant) after each iteration. The phase profile of the electric field at the SLM plane evolves through the iterations, even-

tually converging to a specific phase mask that would produce the desired trap pattern at the sample plane, once it is displayed on an SLM.

The holograms resulting from this type of iterative method are very efficient (with theoretical efficiency close to 100%). However, it takes several iterations for the algorithm to converge on a valid phase mask. This makes the process very slow and prevents holograms from being computed in real time at a video frame rate, loosing the interactivity with the user.

The main drawback of iterative algorithms is hence the long computational time needed, even with modern CPUs, which are currently too slow for three-dimensional real-time applications [62]. A good way to overcome this limitation is the use of a graphics processing unit (GPU) on recent graphics cards [63], which are optimized for use with pixel matrices. This approach enables real-time computation of iterative CGHs. However, even though some programming environments exist for specific graphic card manufacturers (e.g. CUDA language for NVIDIA cards [64]), programming for GPU may still be a difficult task for non-experts.

2.2.2 Prisms-and-lenses

A simple, fast and direct approach for creating multiple traps is the prisms-and-lenses algorithm [65]. This method simply consists of generating a blazed phase grating for shifting a light spot laterally, and a quadratic phase term for changing the focusing plane, as illustrated in Figure 2.1. A lateral shift in two dimensions can be produced by encoding the following phase map in the SLM:

$$\phi(x, y) = 2\pi \left(\frac{x}{L_x} + \frac{y}{L_y} \right) \text{ mod } 2\pi \quad (2.1)$$

The parameter of the grating (L_x, L_y) is directly related to the displacement of the focused spot at the sample plane (Fourier plane of the SLM): $(x_t, y_t) = \left(\frac{\lambda f}{L_x}, \frac{\lambda f}{L_y} \right)$, where λ is the laser wavelength and f the focal length of the system. Multiple 3D trap patterns can easily be created by adding the complex amplitudes of each individual trap and extracting the resulting phase:

$$\phi(x, y) = \arg \left(\sum_j e^{i\phi_j(x, y)} \right) \quad (2.2)$$

which encodes a plurality of optical traps on a single hologram. Note that this algorithm is equivalent to the first iteration of the GS method. The prisms-and-lenses algorithm is much faster than iterative algorithms, and it can be carried out at video rates. As the amplitude modulation term is discarded, intensity fluctuations may occur within the trap pattern. With some corrections [66] one can also get CGHs with good performance for a small number of traps. However, spurious light spots might appear due to the spatial harmonics in the phase-only hologram. The presence of ghost traps in unwanted locations might result in practical problems when they interfere with particles that are meant

to be trapped at designated places, and may reduce the uniformity in periodic trap patterns, such as optical trap arrays.

2.2.3 Random mask multiplexing

Along the same line, in [67] our group presented a simple technique for producing holographic optical traps, based on the random mask (RM) encoding method. It provides a non-iterative and thus very fast algorithm for calculating phase holograms which can be used for optical trapping and micromanipulation at video rates.

The RM encoding method consists of splitting up the whole number of pixels of a SLM into N disjoint sets (masks) of randomly chosen pixels, $M_l (l = 1..N)$, with N being the number of holograms to be simultaneously encoded. An example of the hologram multiplexing process with $N=2$ is illustrated in Figure 2.3. The assignment of pixels to masks is performed randomly to avoid distorting the trap shapes [68]. Each mask displays a phase function $H_l(u, v)$ that can generate a single trap (as in the original method) or an arbitrary light distribution (as we will discuss below). Thus, the hologram $H(u, v)$ encoding all the holograms can be written as:

$$H(u, v) = \sum_{l=1}^N m_l(u, v) H_l(u, v) \quad (2.3)$$

with

$$m_l(u, v) = \begin{cases} 1 & (u, v) \in M_l \\ 0 & (u, v) \notin M_l \end{cases} \quad (2.4)$$

A common problem with many CGHs is that phase-only holograms (e.g. in prisms-and-lenses algorithm) contain harmonics of the encoded information, resulting in the appearance of spurious traps. However, since the information of each hologram here is distributed in a random fashion, the light that is not going to the original traps is simply scattered over the sample, and not concentrated in unwanted locations. However, the method suffers from low efficiency in the holographic reconstruction depending on the number of multiplexed holograms.

2.2.4 Theoretical efficiency of the random mask algorithm

The efficiency of the random mask algorithm can be calculated as follows [41]. If we consider a pure phase hologram $H(j, k)$ of $P \times P$ pixels, encoding N component holograms, and assume with no loss of generality that this hologram is illuminated by a plane wave of unit amplitude, $A = e^{i\phi}$, then the energy at a plane immediately after the hologram is:

$$E_{tot} = \sum_{j=1}^P \sum_{k=1}^P (H(j, k)A)^* H(j, k)A = \sum_{j=1}^P \sum_{k=1}^P |H(j, k)|^2 = P^2 \quad (2.5)$$

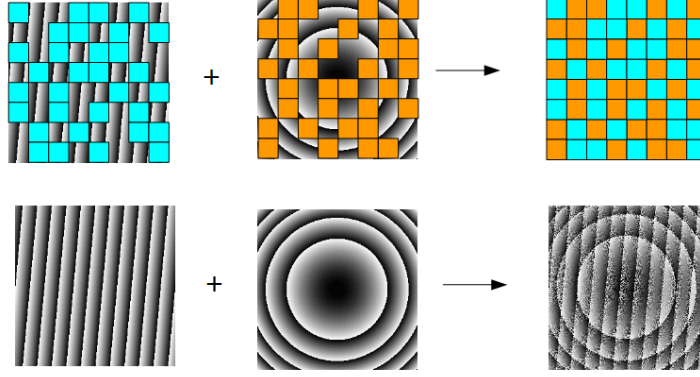


Figure 2.3: Illustrative example of the random mask process: two independent holograms (a linear phase and a spherical phase) are assigned to two randomized groups of pixels that are complementary to each other. When both random masks are overlapped, they form a mosaic with components from each of the original holograms randomly distributed. The combined hologram will simultaneously encode both original traps (in that case, a laterally-shifted trap and an axially shifted trap).

By virtue of Parseval's theorem, this is also the total energy at the sample plane (at the Fourier plane of the SLM). Obviously, the amount of light devoted to each pixel mask will be proportional to the number of pixels in the mask. The field amplitude at a certain position (x, y) in the sample plane (after the optical Fourier transform) can be written, in discrete notation, as:

$$C(x, y) = \frac{1}{P} \sum_{j=1}^P \sum_{k=1}^P H(j, k) e^{-i \frac{2\pi}{P} (xj + yk)} \quad (2.6)$$

For simplicity we now consider the particular case of N multiplexed holograms in which each RM encodes a constituent hologram $H_l(j, k)$ generating one single shifted trap (blazed phase grating). Thus, in a certain trap t located at (x_t, y_t) , with the hologram encoded in mask m_t with n_t pixels, the field amplitude will be:

$$C(x_t, y_t) = \frac{1}{P} \sum_{j=1}^P \sum_{k=1}^P \sum_{l=1}^P m_l(j, k) e^{-i \frac{2\pi}{P} ((x-x_t)j + (y-y_t)k)} \quad (2.7)$$

considering that the light coming from mask m_t will only contribute significantly to the spot at position (x_t, y_t) in the sample plane. Thus, the total energy focused in the traps will be:

$$E_{traps} = \sum_{t=1}^N \left(\frac{n_t}{P}\right)^2 \quad (2.8)$$

The efficiency η , i.e. the relationship between the energy in the traps and the total energy, can be easily calculated in the case of N equally-weighted traps ($n_t = P^2/N$ for each mask):

$$\eta = \frac{E_{traps}}{E_{total}} = \frac{\frac{1}{P^2} \sum_{t=1}^N n_t^2}{P^2} = \sum_{t=1}^N \frac{1}{N^2} = \frac{1}{N} \quad (2.9)$$

This means that with an increasing number of constituent holograms the overall efficiency decreases as the inverse of the number of components, which is the main limitation of this technique. Thus, as a stand-alone procedure the RM algorithm is suitable only for generating a small number of traps, however, as we will show, it lends itself to be applied in combination with other, more efficient algorithms while keeping its advantages.

2.3 New hybrid algorithm combining Random Mask encoding with iterative methods

Here we introduce an alternative use of the RM-multiplexing method as a tool to combine not only individual traps, but pre-computed holograms corresponding to arbitrary trap distributions. It can thus be seen as a meta-algorithm which adds functionalities to holographic traps that have been previously created by another algorithm. The resulting hybrid method shares the advantages of both constituents: the efficiency of iterative methods in generating holograms (here used as building blocks, that are computed off-line), and the speed of RM multiplexing for putting different pieces together and moving each of them independently in real time.

2.3.1 Principle of operation

At first, a set of holograms is pre-calculated (off-line) with a high-efficiency method, obtaining one phase mask corresponding to different blocks or sub-groups of traps. This different pieces may correspond e.g. to the shape of a particular objects of known shape that will be trapped. We use Gercherg-Saxton [60] for that purpose, an iterative method with very high holographic reconstruction efficiency. Each individual hologram (building block) may encode a single trap, a group of traps or an arbitrarily complex light distribution. The individual holograms are computed with a high-efficient iterative algorithm before the experiments, when time is not a constraint. It is important to note that these blocks will behave as rigid pieces (the shape of the trap distribution will be maintained for the whole experiment).

Then the random mask technique is used to put together the different building blocks in a single phase mask, distributing the components into disjoint pixel masks (spacial multiplexing). The resulting phase hologram will contain the information of all different blocks, and will reconstruct all of them simultaneously. Unlike other methods, in RM the information of each building block is localised in a specific separate group of pixels (masks). Thus they can be manipulated independently at a very low computational cost, leaving the rest unchanged. For example, a linear phase, a spherical phase, or an in-plane rotation can be applied to any mask in real time, resulting in independent movements of a single block of traps, with no need to re-compute the whole hologram. The manipulation of a single block does not affect the other holograms.

For example, for translating a group of traps encoded in a individual complex hologram $H_i(x, y)$, the original hologram needs to be multiplied by a linear phase:

$$H'_i(x, y) = H_i(x, y)e^{i2\pi\left(\frac{x}{L_x} + \frac{y}{L_y}\right)} \quad (2.10)$$

Note that this operation is direct and fast, with no need for computationally-demanding iterations to recalculate the hologram for the whole scenario. The resulting phase hologram can then be updated on its correspondent pixel mask. The final hologram will produce a similar pattern as before, but with one subgroup of traps (the one associated to the modified pixel mask) being laterally shifted from its original position.

Additionally, in-plane rotation of one particular building block, can be carried out by rotating the corresponding hologram image within its pixel mask. The rotation may be combined with an additional linear phase shift to tune the centre of rotation.

2.3.2 User interface

A custom LabVIEW interface was built to implement the hybrid method for real time manipulation of rigid groups of traps. The interface can load a collection of pre-computed Gerchberg-Saxton holograms and multiplex them together using random pixel masks. The user can then select the mask corresponding to a specific group of traps, and use the sliders in the interface to produce lateral shifts in x and y direction, or rotate the hologram to make the piece rotate in turn.

Since individual holograms are located in independent pixel-masks, movements in one piece can be performed independently of the rest of the components, whose pixel masks remain unchanged. In the example shown in Figure 2.4 there are two independent groups of 4 traps, and one of them (the square shape) is shifted upwards using a slider in the interface in real time, while keeping the other piece still.

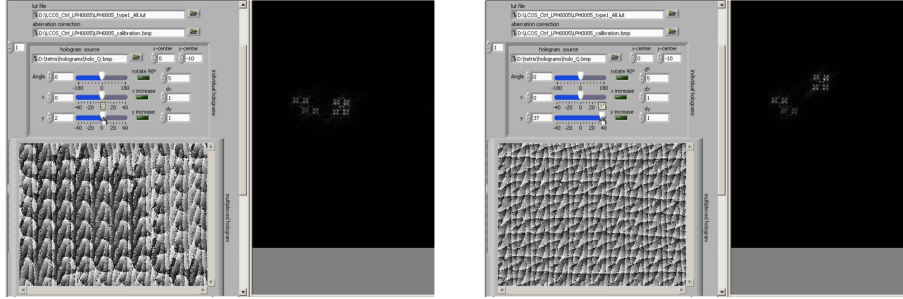


Figure 2.4: LabVIEW interface for multiplexing pre-computed holograms, with controls for shifting and rotating any of the individual pieces. In this case two holograms were multiplexed corresponding to two groups of 4 traps. In the right frame, the square group of traps has been shifted upwards while the other group remains at the same position.

2.3.3 Translation and rotation of groups of trapped microbeads

The manipulation of assembled groups of optically-trapped beads is shown in Figure 2.5, in which three independent blocks of four polystyrene spheres (1 μm in diameter) are moved along complex trajectories by means of three multiplexed GS holograms. As the efficiency of the RM encoding method decreases with the number of masks, the performance of the final hologram is improved by using these groups of several traps as building blocks, as opposed to multiplexing 12 single-trap holograms. Meanwhile the practical advantages of the RM encoding method (speed, localized information, and lack of spurious light concentrations) are maintained. The downside is that the shape of each independent group of traps (each one associated to one pre-computed hologram) must remain constant during the experiment, but as we described before there are plenty of applications that can benefit from dynamic manipulation of rigid shapes or groups of traps.

2.3.4 Quantifying hologram efficiency and trap stiffness

In order to evaluate the performance of the hybrid method in practice, we measured the stiffness of several holographically-generated optical traps as a function of the number of multiplexed holograms. For this experiment, we used an array of 4 x 3 optical traps, with approximately 4 μm separation between traps and we trapped twelve polystyrene beads (Fluka 72938, $1.16 \pm 0.04 \mu\text{m}$ in diameter) suspended in water. The array was first created using a single GS hologram. Then, four hybrid configurations generating the same trap pattern were constructed using a different number of multiplexed holograms (N) in every case. For each hybrid hologram, an elementary GS hologram representing a small group of $12/N$ traps was cloned N times using the RM encoding method.

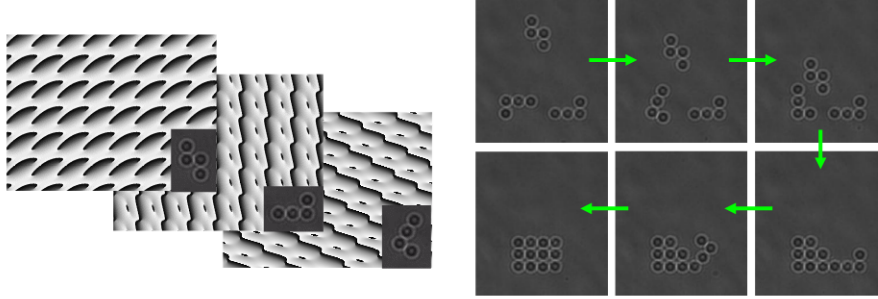


Figure 2.5: GS holograms corresponding to different Tetris pieces. The image sequence shows optically-trapped microbeads forming three independent blocks of 4 traps. The pieces are independently translated and rotated using the hybrid method.

N	Elemental piece (GS Hologram)	Multiplexing process
1	4x3 (full array)	No multiplexing (single GS hologram)
2	2x3 (half array)	Added horizontal shift
3	4x1 (row)	Added vertical shifts (3 rows)
4	1x3 (column)	Added horizontal shifts (4 columns)
12	single traps	Each piece is a linear phase grating

Table 2.1: Different configurations for building a 4x3 array of optical traps using the hybrid method. In each case, N clones of an elementary piece were multiplexed using N equally-weighted random masks. Linear phases were added, as described in “Multiplexing process” column, in order to place the traps in the same locations as those in the original 4x3 array.

Table 2.1 summarizes the construction process.

The theoretical efficiencies of the holograms were evaluated by Fourier-transforming each phase hologram to obtain the energy distribution at the sample plane. Efficiency was calculated as the ratio between the amount of energy at the trap positions and the total energy of the image. The efficiency as a function of the number of holograms is shown in Figure 2.6a, showing an exponential decay with power -1.01 ± 0.04 . The efficiency being the inverse of the number of multiplexed masks still holds even if we do not use pure linear-gratings as building blocks, but complex GS encoding a plurality of traps. This exponent matches with the expected behaviour according to Equation 2.9 (efficiency proportional to the inverse of N), which we get even when the individual holograms were not just linear phases but more complex GS holograms. Efficiency of individual holograms varies between 0.79 and 0.95.

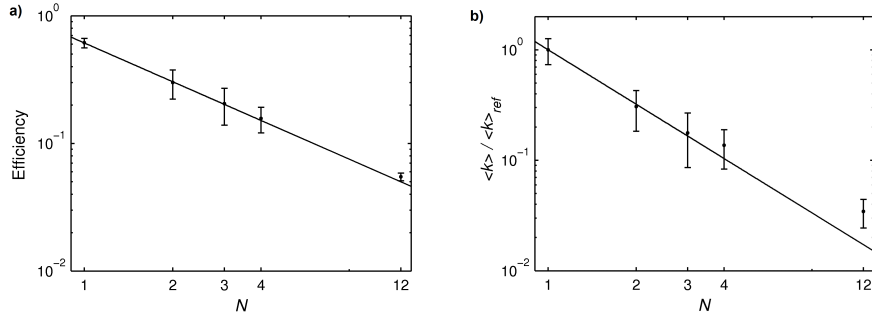


Figure 2.6: Simulated efficiency (a) and experimental trap stiffness (b) averaged over the entire array

The transverse stiffness κ_x and κ_y of the traps in the array were measured for each hybrid hologram as well as for the original GS hologram for comparison. Since there were several optical traps, the stiffness calibration was performed by video analysis. The Brownian motion of the trapped beads was registered with a CCD camera (QICAM 12-bit-mono Fast) for 105 frames. Particle trajectories were obtained with nanometer resolution using the Video Spot Tracker software from CISMM.¹

Since the temporal resolution of the camera was not high enough to allow us to calibrate the trap via a spectral analysis, trap stiffness was estimated using the equipartition theorem:

$$\kappa_x = \frac{k_B T}{\sigma_x^2} \quad \kappa_y = \frac{k_B T}{\sigma_y^2} \quad (2.11)$$

where σ_x and σ_y are the standard deviations of the measured particle trajectories, T is the absolute temperature of the sample and k_B is the Boltzmann constant. Interestingly, Figure 2.6b shows that the transverse stiffness of the optical traps, averaged over the entire array, decreases also as a power law of the number of multiplexed holograms in a similar way to efficiency, but with a faster decay (exponent -1.6 ± 0.2).

Thus, when using the proposed hybrid method, it is important to carefully consider the balance between the number of independent parts and the strength of the optical traps. Splitting a trap pattern into separate pieces gives flexibility, allowing the easy manipulation of different objects, but at the expense of weaker optical forces. Since the amount of laser power in practice is limited, it is important to keep the efficiency of the holograms high enough for trapping. Thus, we recommend the use of the hybrid method with a reasonably low number of independent blocks.

¹Video Spot Tracker is a particle tracking software developed by CISMM at UNC-CH, supported by the NIH NIBIB (NIH 2-P41-EB002025) and it is available for free at: <http://cismm.web.unc.edu/software/> (last checked 17/08/2016).

2.4 Conclusions

We have presented a hybrid method combining an iterative algorithm with the RM encoding method for manipulating groups of holographic optical traps in real time. The individual hologram for each block was previously computed using the highly-efficient iterative algorithm and the RM encoding method was used to quickly and accurately join the holograms. We have shown that with the proposed method, different rigid parts (i.e. groups of traps with a fixed spatial distribution according to the specific object shape and dimensions) can be independently manipulated without time-consuming computations.

The main advantages of this method compared to others are its simplicity, its speed, and the lack of spurious light spots. The main drawback of the method is an inherent efficiency reduction, which we found out to decrease with the number of multiplexed holograms, as noticed in trap stiffness measurements. Thus, there is an important trade-off between the desired hologram efficiency (the lower the number of masks, the better) and its flexibility (number of independent pieces).

Chapter 3

Active-passive calibration of optical traps in fission yeast cells

Since the first demonstration of force measurements inside living cells by Ashkin et al [14], the quantification of intracellular biological forces has remained a challenge due to the difficulties of calibrating the trap strength in a complex media such as the cellular cytoplasm [69, 21]. Traditional trap calibration methods are only applicable in purely viscous media, but the cellular cytoplasm, packed with organelles and cellular components, is better described as a gel, with viscoelastic properties.

The cytoplasm of biological cells can be fairly modelled as a viscoelastic material, containing a fluid body (cytosol) as well as rigid/elastic structures that give mechanical consistency to the cell (actin and intermediate filaments, and microtubules). Viscoelastic materials present properties of both fluid and elastic substances. As a consequence, a microscopic particle within a viscoelastic medium experiences a force that would be partly hydrodynamic (proportional to their relative velocity) and partly elastic (proportional to the position within the medium).

Active-passive calibration of optical traps in viscoelastic media, based on the Fluctuation Dissipation Theorem (FDT), has been proposed as one possible method for measuring optical forces inside living cells. The method was first developed theoretically by M. Fischer and K. Berg-Sørensen [3] and later experimentally tested in an F-actin gel by Fischer et al. [4]. It is applicable to a trapped particle in a locally homogeneous viscoelastic media, without any explicit assumptions on the medium's viscoelasticity (as opposed to [70]). The method involves a set of measurements of the undriven system (i.e. with the trapped particle undergoing natural thermal agitation) and the driven system (i.e. with small external perturbations applied to the system), which can be combined to determine the trap stiffness and the friction retardation spectrum

of the system. External perturbations can be applied either by oscillating the sample stage (while keeping the laser still) or by oscillating the laser position (while keeping the sample still).

Here we use the stage-oscillation approach, similarly to [4], which can be easily integrated on an existing optical trapping setup by using a piezoelectric stage as a sample holder. We apply active-passive calibration method for the first time inside a living biological environment, and we show the possibility of determining trap stiffness on optically-trapped intracellular organelles, and the viscoelastic properties of the cell cytoplasm [71].¹

This chapter contains first a summary on the theory behind the method, followed by the experimental protocols, a detailed description of the data analysis, and the results obtained in living fission yeast cells.

3.1 Theory of active-passive calibration in viscoelastic media

3.1.1 Description of an optically trapped particle in a viscoelastic media

The theoretical development [3] starts from a generalized Langevin equation for the position of the particle, including particle inertia, a random thermal agitation force, a harmonic force term (optical trap), the speed and acceleration memory terms (to account for the interaction of the particle with the viscoelastic medium over time), and external forces (for active perturbations). Here we describe the equations corresponding to the undriven (“U” sub-index) and a stage-driven (“D” sub-index) scenarios:

$$m\ddot{x}_U(t) = - \int_0^\infty \gamma_{1,U}(\tau)\dot{x}_U(t-\tau)d\tau - \int_0^\infty \gamma_{2,U}(\tau)\ddot{x}_U(t-\tau)d\tau - \kappa x_U(t) + F_{random}(t) \quad (3.1)$$

$$\begin{aligned} m\ddot{x}_D(t) = & - \int_0^\infty \gamma_{1,D}(\tau)(\dot{x}_D(t-\tau) - \dot{x}_s(t-\tau))d\tau + \dots \\ \dots - \int_0^\infty & \gamma_{2,D}(\tau)(\ddot{x}_D(t-\tau) - \ddot{x}_s(t-\tau))d\tau - \kappa x_D(t) + F_{random}(t) \end{aligned} \quad (3.2)$$

where $x_{U/D}(t)$ are the trapped particle’s position (with $\dot{x}_{U/D}(t-\tau)$ and $\ddot{x}_{U/D}(t-\tau)$ being its pasts velocity and acceleration), $\gamma_{1,U/D}(\tau)$ and $\gamma_{2,U/D}(\tau)$ are the time-dependent viscous and elastic memory effects respectively, κ the trap stiffness, $F_{random}(t)$ is the thermal agitation force (with average zero, and standard deviation $\sqrt{2k_B T \gamma_{1,U/D}(t)}$, where k_B is the Boltzmann’s constant and T the temperature), m is the mass of the particle, and $x_s(t)$ is the stage position in stage-driving situation (with $\dot{x}_s(t-\tau)$ and $\ddot{x}_s(t-\tau)$ being its pasts

¹The research presented in this chapter was carried out during an internship at the Niels Bohr Institute (Copenhagen) and the Technical University of Denmark (DTU Physik, Kgs. Lyngby), as part of the FPU program from the Spanish Ministry of Education.

velocity and acceleration). The previous equations can also be expressed as a Fourier decomposition [3] such that:

$$-\omega^2 m \tilde{x}_U(\omega) = -i\omega \tilde{\gamma}_U(\omega) \tilde{x}_U(\omega) - \kappa \tilde{x}_U(\omega) + \tilde{F}_{random}(\omega) \quad (3.3)$$

$$-\omega^2 m \tilde{x}_D(\omega) = -i\omega \tilde{\gamma}_D(\omega) \tilde{x}_D(\omega) - \kappa \tilde{x}_D(\omega) + \tilde{F}_{random}(\omega) + \tilde{F}_{ext}(\omega) \quad (3.4)$$

where $\tilde{\gamma}(\omega) \equiv \tilde{\gamma}_{1,U}(\omega) + i\omega \tilde{\gamma}_{2,U}(\omega)$ is known as the friction retardation spectrum, with its real part accounting for dissipative processes and its imaginary part accounting for elastic processes in the interaction between the bead and the medium [4]. The term $\tilde{F}_{ext}(\omega) = i\omega \tilde{\gamma}(\omega) \tilde{x}_s(\omega)$ is the external perturbation to the trapped bead caused by stage driving, through the surrounding media.

The thermal fluctuations average out over time, making the random terms vanish for a sufficient long measurement. The thermal average of the particle positions for the undriven and driven scenarios is then:

$$\langle \tilde{x}_U(\omega) \rangle = 0 \quad (3.5)$$

$$\langle \tilde{x}_D(\omega) \rangle = \chi(\omega) \tilde{F}_{ext}(\omega), \quad \chi(\omega) = \frac{1}{\kappa + i\omega \tilde{\gamma}_D(\omega) - \omega^2 m} \quad (3.6)$$

where $\chi(\omega)$ is the system's response function relating an external force perturbation to the position fluctuations on the trapped bead. Note that $\chi(\omega)$ is as a matter of fact an inverse effective spring constant, taking into account both the medium viscoelasticity and the actual trap stiffness.

For convenience one can define the following quantities, corresponding to passive $P_U(\omega)$ and active $\tilde{R}_S(\omega)$ measurements.

$$P_U(\omega) \equiv \langle |\tilde{x}_U(\omega)|^2 \rangle = \frac{2k_B T \text{Re}\{\tilde{\gamma}_U(\omega)\}}{|\kappa + i\omega \tilde{\gamma}_U(\omega) - \omega^2 m|^2} \quad (3.7)$$

$$\tilde{R}_S(\omega) \equiv \tilde{\gamma}_D(\omega) \chi(\omega) = \frac{\tilde{x}_p(\omega)}{i\omega \tilde{x}_s(\omega)} \quad (3.8)$$

If the perturbations are sinusoidal stage oscillations with angular frequency $\omega = 2\pi f$, amplitude $A_S(\omega)$ and phase ϕ_S , to which the particle responds with a sinusoidal amplitude $A_p(\omega)$ and phase ϕ_p . In that case, the active spectra $\tilde{R}_S(\omega)$ can be conveniently expressed in terms of measurable parameters as:

$$\tilde{R}_S(\omega) = \frac{\tilde{x}_p(\omega)}{i\omega \tilde{x}_s(\omega)} = \frac{A_p e^{i(\omega t + \phi_p)}}{\omega A_s e^{i(\omega t + \phi_s + \pi/2)}} = \frac{A_p}{\omega A_s} (\sin \Delta\phi - i \cos \Delta\phi) \quad (3.9)$$

where

$$\Delta\phi = \phi_p - \phi_s \quad (3.10)$$

is the phase delay between the particle and the stage sinusoidal trajectories.

3.1.2 Central assumption, and requirements for trap calibration

In order to calibrate the trap constant, the key assumption of the method is that the friction retardation spectrum is the same for the driven and the non-driven scenarios, following Onsager's regression hypothesis [3], so that

$$\tilde{\gamma}_D(\omega) = \tilde{\gamma}_U(\omega) \equiv \tilde{\gamma}(\omega) \quad (3.11)$$

This is a consequence of the Fluctuation Dissipation Theorem (FDT) [4], which relates the imaginary part of the system response $\chi(\omega)$ with the two-sided power spectrum $P(\omega)$ of random particle oscillations:

$$\text{Im}\{\chi(\omega)\} = \frac{\omega}{2k_B T} P(\omega) \quad (3.12)$$

This condition holds for small disturbances of the system, so that it is reasonable to assume that the system responds linearly to the applied perturbation, and that its response function is not permanently modified because of the applied perturbation (stationary process). As an example, a stage driving amplitude of 100nm was successfully used previously for calibrations in actin gel, whereas larger driving amplitudes (500nm) were shown to have changed the viscoelastic properties of the medium [4], possibly because of actin network disruption.

Additionally, one should make sure that the particle stays within the harmonic region of the trap potential, so that the trap force is fairly modelled at all times as a spring with stiffness κ . For Rayleigh particles (much smaller than the wavelength) a reasonable linear scanning range can be around half of the beam waist radius [28], whereas for larger particles the linear region scales with the particle size. In any case, the trapping power should be enough to keep the objects tightly trapped, so that they stay within the harmonic part of the trap for the whole calibration process, despite thermal agitation and external perturbations.

Finally, the trapped particle should also stay within the linear range of the position detector. Typically a Quadrant Photodiode (QPD) is used in Back-focal-plane interferometry for detecting the trapped object's position, with high accuracy, at a fast sampling rate. However, the QPD signals are linear with the trapped object's position only within a certain range of positions near the trap centre. The extent of the linear range depends on the size of the spot on the detector, which may change depending on the trapped object. Hence, it is important to make sure that the trapped particle does not move out of this linear regime in all calibration experiments.

3.1.3 Trap calibration

Following the conditions described before, one can then combine active and passive spectra (Eqs. 3.7 and 3.8) to obtain an expression for the trap stiffness

[3, 4]:

$$(\kappa - \omega^2 m)_\omega = \frac{2k_B T}{P(\omega)} \text{Re}\{R_s(\omega)\} \quad (3.13)$$

The left hand side of the active-passive calibration equation can be fitted for using the frequency-dependent values for the right-hand side of the equation, to obtain the trap stiffness (κ) and the mass (m) of the trapped particle. In practice, considering the very small mass of the trapped particles, and the low driving frequencies for the stage-driving approach (typically below 100Hz), the inertial term $\omega^2 m$ can be completely neglected with respect to the trap stiffness and viscoelastic forces [4, 71]. Hence, for the case of stage driving (following Equation 3.9) one gets:

$$\kappa(\omega) \simeq \frac{2k_B T}{P(\omega)} \frac{A_p(\omega)}{\omega A_s(\omega)} \sin(\Delta\phi) \quad (3.14)$$

This allows one to calculate the trap stiffness from a list of measurable quantities such as the fitted parameters of the particle and stage sinusoidal trajectories, including their amplitudes (A_p and A_s), the phase delay between the particle and the stage ($\Delta\phi$), the perturbation driving frequency ($\omega = 2\pi f$), the temperature (T), and the passive power spectrum (for the undriven system) evaluated at frequency ω . The passive power spectrum can be calculated in practice from the Fourier transform of the undriven particle's trajectory over a finite time:

$$\langle P(\omega) \rangle = \lim_{T_{meas} \rightarrow \infty} \frac{\langle |\tilde{x}_p(\omega)|^2 \rangle}{T_{meas}} \quad (3.15)$$

with a measurement time T_{meas} typically in the order of a few seconds. In its discrete form, the Fourier transform of a finite signal $x(t)$ of length N , sampled at δt time intervals can be calculated like:

$$\tilde{x}(\omega_k) = \delta t \sum_j^N e^{-i2\pi j k/N} x(t_j) \quad (3.16)$$

The stage amplitude A_s is easily given in physical units, since the conversion factor between the piezo monitor channel and its physical position is a known property of the piezoelectric stage system. However, an additional step is needed to obtain A_p in physical units, since the voltage-to-position conversion factor of the QPD signals depends on each trapped object. This position calibration factor (β) can be measured in practice by comparing video and QPD signal amplitude as described later in this chapter. Then, one can convert voltage measurements A_p^V to physical units by using: $A_p = A_p^V \beta$, as well as the power spectrum: $P(\omega) = \beta^2 P^V(\omega)$.

One can first determine the force calibration constant directly in voltage units (κ^V in pN/V):

$$\kappa^V(\omega) = \frac{2k_B T}{P^V(\omega)} \frac{A_p^V(\omega)}{\omega A_s(\omega)} \sin(\Delta\phi) \quad (3.17)$$

Once this conversion factor is known, one could potentially use the trapped object as a handle to measure optical forces, similarly to a dynamometer from QPD voltage signals, as the particle moves away from the trap centre: $F = \kappa^V(x^V - x_0^V)$. However in many cases the trap stiffness needs to be known in physical units (e.g. $pN/\mu m$), for quantifying the strength of the optical trap and comparing with other optical trapping experiments. This can be easily obtained once β is known, with the trap stiffness (κ) in physical units being:

$$\kappa(\omega) = \frac{\kappa^V(\omega)}{\beta} \quad (3.18)$$

The uncertainty in individual trap stiffness measurements can be calculated by error propagation from all the measured parameters:

$$\frac{\Delta\kappa(\omega)}{\kappa(\omega)} = \left[\left(\frac{\Delta T}{T} \right)^2 + \left(\frac{\Delta P(\omega)}{P(\omega)} \right)^2 + \left(\frac{\Delta A_p(\omega)}{A_p(\omega)} \right)^2 + \dots \right. \\ \left. \left(\frac{\Delta A_s(\omega)}{A_s(\omega)} \right)^2 + \left(\frac{\Delta(\Delta\phi(\omega))}{\tan(\Delta\phi(\omega))} \right)^2 + \left(\frac{\Delta\beta}{\beta} \right)^2 \right]^{-1/2} \quad (3.19)$$

Typically the most important contributors to the error $\Delta\kappa$ are $\Delta\beta$ and $\Delta(\Delta\phi)$, as illustrated later in the experimental results. Active measurements are normally carried out through a set of n different frequencies, and then the average value $\kappa_{av} = \langle \kappa(\omega) \rangle$ is taken as the final trap stiffness result. The uncertainty $\Delta\kappa_{av}$ in the results presented later in this chapter combine the statistical error (SEM) and the average error from the individual $\kappa(\omega)$ measurements, taking into account that a certain error in global parameters such as β or t_{delay} cannot be reduced by averaging measurements over different frequencies:

$$\Delta\kappa_{av} = \sqrt{\left(\frac{\sigma_{\kappa(\omega)}^2}{n} \right) + \langle \Delta\kappa(\omega) \rangle^2} \quad (3.20)$$

3.1.4 Viscoelastic parameters

The viscoelastic properties of the cytoplasm can then be calculated from the previous measurable quantities. The system response function is:

$$\chi(\omega) = \frac{1 - i\omega\tilde{R}_s(\omega)}{\kappa - \omega^2 m} \simeq \frac{1 - i\omega\tilde{R}_s(\omega)}{\kappa(\omega)} \quad (3.21)$$

And considering it as an effective inverse spring constant (as suggested by Eq. 3.6), one can define:

$$\kappa_{eff}(\omega) = \frac{1}{|\chi(\omega)|} \quad (3.22)$$

Note that κ_{eff} includes contributions from both the trap and the medium, hence it will normally take a value that is higher than the actual trap stiffness κ .

The friction retardation spectrum and its errorbars for the real and imaginary parts are calculated as follows[71]²:

$$\tilde{\gamma}(\omega) = \frac{\tilde{R}_s(\omega)}{\chi(\omega)} \quad (3.23)$$

$$\frac{\Delta(\text{Re}\{\tilde{\gamma}(\omega)\})}{\text{Re}\{\tilde{\gamma}(\omega)\}} = \sqrt{\left(\frac{\Delta\kappa_{av}}{\kappa_{av}} + \frac{\Delta\beta}{\beta}\right)^2 + \left(\frac{\Delta(\Delta\phi)}{\tan(\Delta\phi)}\right)^2} \quad (3.24)$$

$$\frac{\Delta(\text{Im}\{\tilde{\gamma}(\omega)\})}{\text{Im}\{\tilde{\gamma}(\omega)\}} = \sqrt{\left(\frac{\Delta\kappa_{av}}{\kappa_{av}} + \frac{\Delta\beta}{\beta}\right)^2 + \left(2\frac{\Delta(\Delta\phi)}{\tan(\Delta\phi)}\right)^2} \quad (3.25)$$

Finally, the frequency-dependent G modulus can be calculated as:

$$G(\omega) = \frac{i\omega}{6\pi r} \tilde{\gamma}(\omega) \quad (3.26)$$

with its real part, known as the shear storage modulus, is a measure of the elastic energy stored in the system. Its imaginary part, known as the shear loss modulus, is related to the dynamic viscosity of the system. The error bars for the real and imaginary parts can be calculated as follows:

$$\frac{\Delta(\text{Re}\{G(\omega)\})}{\text{Re}\{G(\omega)\}} = \sqrt{\left(\frac{\Delta(\text{Im}\{\tilde{\gamma}(\omega)\})}{\text{Im}\{\tilde{\gamma}(\omega)\}}\right)^2 + \left(\frac{\Delta r}{r}\right)^2} \quad (3.27)$$

$$\frac{\Delta(\text{Im}\{G(\omega)\})}{\text{Im}\{G(\omega)\}} = \sqrt{\left(\frac{\Delta(\text{Re}\{\tilde{\gamma}(\omega)\})}{\text{Re}\{\tilde{\gamma}(\omega)\}}\right)^2 + \left(\frac{\Delta r}{r}\right)^2} \quad (3.28)$$

where r is the radius of trapped particle, which can be measured on the microscope images.

3.2 Experimental methods

3.2.1 Optical trapping setup

The optical trapping setup uses a $Nd : YVO_4$, laser (5W, SpectraPhysics BL-106C, 1064nm) coupled into an inverted microscope (Leica DMIRBE) and focused with an oil immersion objective (Leica HCX PL APO 100X, NA=1.4 OIL CS). A piezo-electric translation stage with capacitive feedback (PI P-517.3CL) is used to oscillate the sample. A QPD (S5981, Hammamatsu) was placed at a conjugate plane of the back-focal plane of a high NA condenser lens (1.4NA, OIL), for particle position sensing. A dichroic mirror allowed sample illumination with the microscope lamp, while deflecting the laser beam (coming from the sample) towards the lateral arm and the QPD detector.

²Part of the expressions for error propagation are based on unpublished notes from M. Fischer

A data acquisition card (NI PCI-6040E) was used to read the stage positions simultaneously with QPD signals. A CCD camera (All KODAK Pike, 60fps) was placed at the side port of the microscope to image the sample. An additional lens in front of the CCD provided some additional magnification, resulting in a pixel resolution of $(5.56 \pm 0.02)nm/pixel$. Even though granule images are still conditioned by the objective diffraction limit, having this extra magnification allowed us to better track the displacements of the trapped objects for β calibration.

3.2.2 *S. Pombe* samples

S. Pombe cells (SPK10 strain, wild type, h-)³ were cultured in agar dishes. After spreading cells in a new agar dish to form new colonies, the culture dish was kept 24h in the incubator at 30°C, and then stored in the fridge at 4°C. Before the experiments, a small amount of cells was transferred with a sterile tip from the agar plate to a flask with 12mL of yeast extract peptone dextrose medium (YPD), a common broth for yeast cells growth. The cells were then left to grow overnight on a shaking water bath.

For the experiments, cells were then transferred to an AA (amino acid) medium, and alternative cell growth media containing bacto yeast nitrogen base, ammonium sulfate, and an amino acid drop-out mix minus leucine. This AA media was used in substitution of YPD because it turned out that the latter interfered with the poly-L-lysine coatings used for cell adhesion on the glass (see description of microchamber below). For transferring to the new media, the YPD cell suspension was centrifuged for 5min at 5000rpm, the YPD medium extracted, and the cell pellet re-suspended on fresh AA medium.

Active-passive experiments require cells to move simultaneously with the stage, in order to transfer the desired perturbations to the cytoplasm and ultimately to the trapped organelle. Since *S. Pombe* cells would not naturally attach to the glass coverslips, we used a poly-L-lysine coating to glue the cells to the coverslip surface. For that purpose 10 μ L of a solution containing 10mg/mL of poly-L-lysine (Sigma) in a phosphate buffer (10mM K_3PO_4) was uniformly spread over a clean coverslip surface (previously washed with 70% ethanol) and let dry out forming a thin coating. Then a perfusion chamber was built using the coated coverslip below (with the poly-L-lysine layer facing inside), double sided scotch tape as spacer (leaving two apertures at the sides for flushing medium), and a thick glass slide on top. The cell suspension was introduced between the glass slides, with the aid of capillary forces, leaving no air bubbles, and the chamber was finally sealed using vacuum grease at the open sides, to prevent evaporation.

³*S. Pombe* cells for the experiments presented in this chapter were provided by Prof. Geneviève Thon (Dept. Genetics, Institute of Molecular Biology, University of Copenhagen)

3.2.3 Preliminary equipment characterization

A read-out delay was found between QPD and stage signal readings through the acquisition card. We quantified this delay with a stuck bead scanned across the laser spot (linear region) with sinusoidal stage driving at different frequencies (from 5Hz to 50Hz), obtaining $\phi_p - \phi_s = \omega t_{delay}$, with $t_{delay} = 467 \pm 65 \mu s$. This value was later used to correct the observed phase delay between the particle and stage in all active-passive calibrations, using the following expression and its associated uncertainty:

$$\Delta\phi_{corrected} = \Delta\phi_{fit} + \omega t_{delay} \quad (3.29)$$

$$\Delta(\Delta\phi) = \sqrt{(\Delta(\Delta\phi_{fit}))^2 + (\omega_s \Delta t_{delay})^2} \quad (3.30)$$

The most relevant term in practice for the phase uncertainty in our measurements is the part coming from Δt_{delay} , which becomes specially relevant at higher frequencies, as shown later in this chapter.

Regarding the piezo-electric stage, its actual sinusoidal displacement was found to decrease as the driving frequency increased, for a sinusoidal input voltage of a constant amplitude (sent from the NI-DAQ card). The response curve is shown in Figure 3.1. For the actual measurements, the input signal amplitude was corrected (dividing by the appropriate point in the stage response curve) in order to get the stage moving with the desired amplitude.

3.2.4 Protocol for active-passive calibration experiments

Samples were placed on the inverted microscope and the illumination column adjusted for Köhler illumination. Lipid granules inside different *S. Pombe* cells were trapped. For each of them, the following experimental protocol was followed:

1. A target lipid granule was trapped inside a yeast cell using a laser current of 8.2A (corresponding to 500mW laser output, or 116mW at the sample).
2. A photograph of the cell with the optically-trapped granule was taken at the start and at the end of the calibration process, to record the granule position within the cell environment, and make sure the conditions (size/focus) remain the same before/after the calibration process. An example of granule images is shown in Figure 3.2.
3. The calibration of the voltage-to-position conversion factor β for each trapped object requires measuring particle displacements both in physical units (with the CCD camera) and voltage units (with QPD). Due to the limited camera frame rate (60Hz) this measurement was performed at a low driving frequency (2Hz), so that sinusoidal trajectories could be reasonably sampled in time. The stage driving amplitude was set to 200nm, which produced particle displacements in the range of 5 to

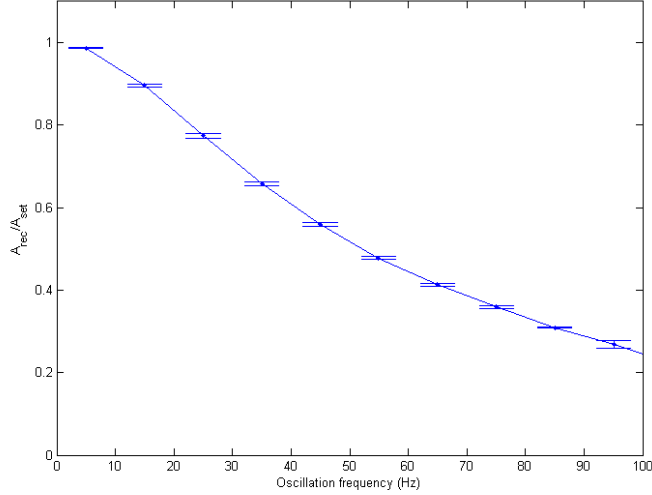


Figure 3.1: Stage response curve (recorded amplitude / set amplitude) to sinusoidal drivings as a function of the the driving frequency, averaged over three different driving amplitudes (200nm, 500nm and 1000nm).

14 pixels for different granules, that could be successfully tracked from the camera images. For video measurements the condenser aperture was closed to provide maximum image contrast for the trapped lipid granules. An identical experiment was performed immediately afterwards with the condenser aperture fully open (and the microscope lamp off), for reading the QPD signals corresponding to the same driving amplitude.

4. Passive measurements involve recording the Brownian motion of the trapped particle with no external perturbation (no stage movements). For that purpose, 3s time series at 22kHz were recorded 30 times, distributed before and after the active recordings.
5. Active measurements involve driving the stage at controlled amplitude and frequencies and simultaneously recording the stage and QPD signals, to evaluate the particle movements in response to the applied perturbations. The stage was driven in a sinusoidal fashion for 10s, and data was recorded at 10kHz. Stage amplitude was set to $A_s = 100nm$ (similarly to previous experiments in actin gel [4]), and frequency was scanned from 5Hz to 75Hz in 5Hz steps.

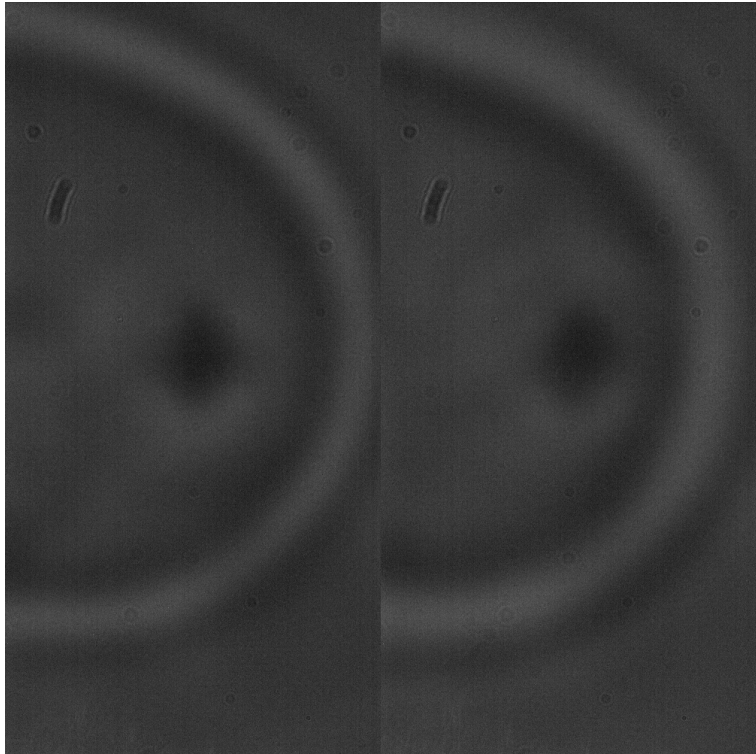


Figure 3.2: Images of a trapped granule before and after active passive calibration. No significant defocus or change of size was observed.

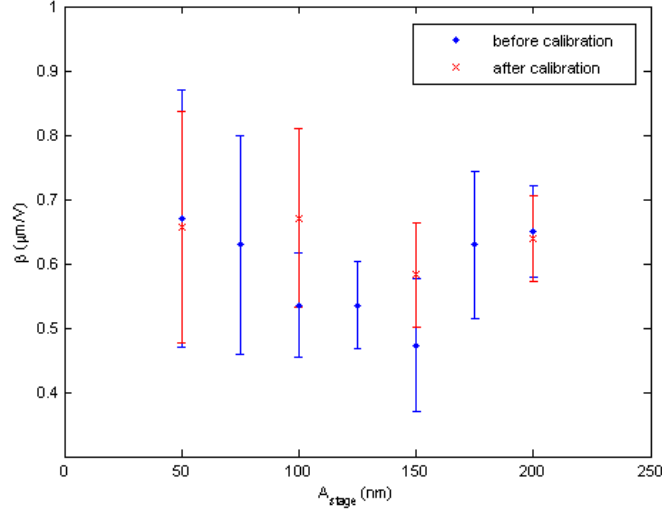


Figure 3.3: β calibration on a single lipid granule before/after active measurement, at different stage amplitudes (within linear region)

3.2.5 Comments on amplitude choice for β calibration

The driving amplitude for β calibration should be large enough to produce visible particle shifts (that can be detected in video images), but it is also important to make sure the particle stays within the linear region of the QPD. As long as this condition is fulfilled, measurements of beta are independent of the driving amplitude. Additionally, the β parameter measured for the same granule before and after the whole calibration process are compatible as long as there are no major changes in the trapping conditions (such as focus changes or new objects coming into the trap). Evidence of changes during the calibration process may also be observed on the active/passive signal checks described in the data analysis section.

3.3 Data analysis

Active-passive calibrations require more extended analysis process than other standard methods (e.g. equipartition theorem or drag forces). To automatize the analysis a custom MATLAB package was developed as part of this thesis, so that it can be used by non-experts of retrieving the trap parameters from active-passive recordings. A snapshot of the program interface is shown in Figure 3.4. The program guides the user through the different stages of data analysis, starting from data loading and pre-screening (upper-left), β calibration, passive spectra analysis, fitting of active time series, calculation of trap stiffness and

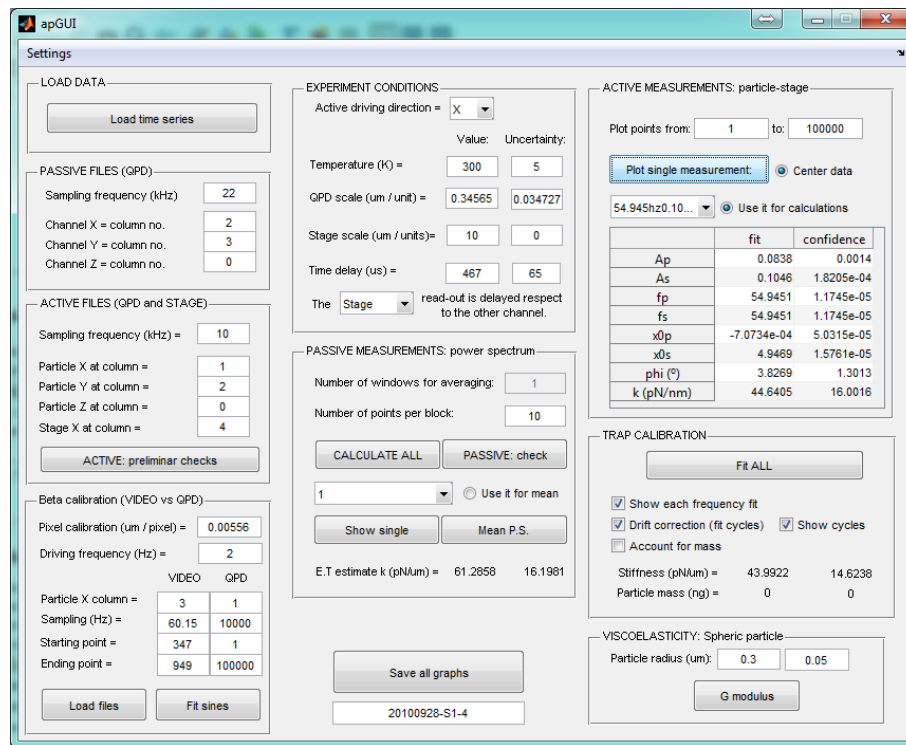


Figure 3.4: Custom MATLAB user interface for analysing active-passive calibration data

viscoelastic parameters. The general experiment parameters (including temperature, card time delay between channels, and stage position conversion factor) are manually introduced in the interface.

3.3.1 Data loading and preliminary checks

For start, clicking the “Load time series” button runs “load_data2.m” script, which lets the user import active measurements (identified with a specific character string in the filename containing the driving frequency for each file) and passive measurements (before and after active measurements). The sampling frequency and the column number for the different QPD channels and the stage is manually specified in the corresponding text boxes.

Clicking the “Active: preliminary checks” button runs a script to calculate and display an initial set of preliminary checks for the active measurements (“mean_evolution2.m”), as shown in Figure 3.5. This part of the analysis looks into the X and Y signals, to show any unexpected movements in the Y (non-driving) direction, and any signal jumps or drifts across the experiments that could indicate changes in the trapping conditions (or even a new object coming

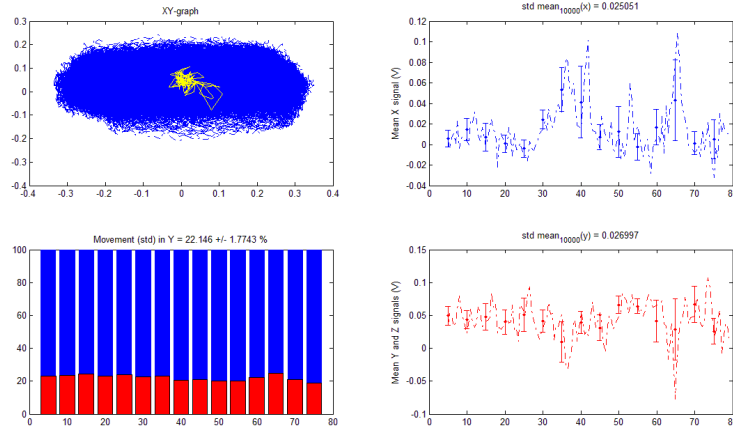


Figure 3.5: Active measurements preliminary checks

back into the trap).

Most of the particle movement is expected to take place along the driving direction (X). In the example shown in Figure 3.5 there is an average 22% movement in the Y channel (calculated as relative standard deviation $\sigma_Y/(\sigma_X + \sigma_Y)$), which is due to the natural Brownian motion in the Y direction.

3.3.2 Beta calibration

The “Beta calibration” panel is used for calculating the volts-to-position conversion factor for each trapped particle. The input parameters include the camera pixel calibration constant, the sinusoidal driving frequency (typically 2Hz) and the sampling rate for video and QPD signals.

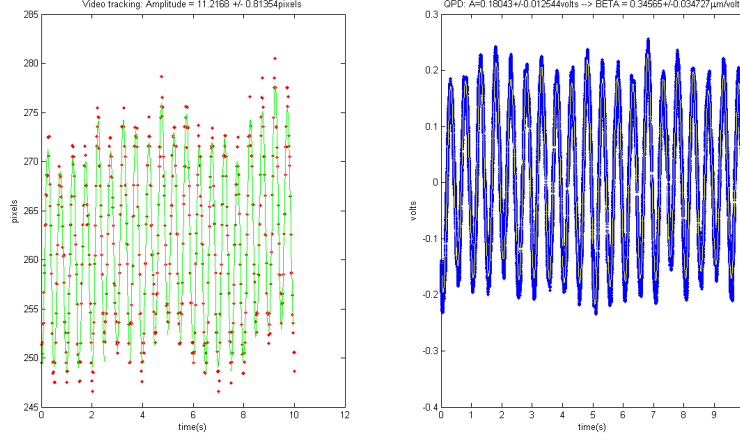
Particle tracking for beta calibration was carried out externally using Video Spot Tracker software ⁴, as well as a home-made particle tracking software ⁵, with good agreement between both methods.

“Load files” button runs the “beta_load.m” script, which prompts the user to choose a file with video tracking results (a column with particle trajectory, in pixel units) and another file with corresponding QPD signal (measured on the same particle, with the same driving frequency and amplitude). The column number with the relevant data for each file is manually specified in the interface text boxes.

After a preliminary display of the loaded position time series (where a sinusoidal oscillation should be clearly identifiable both in video and QPD signals),

⁴Video Spot Tracker software is developed by CISMM, Computer Science group, University of North Carolina, and is freely available at: <http://cismm.web.unc.edu/software/>

⁵Credit: Nader Reihani

Figure 3.6: Sinusoidal fits for β calibration

the start and end points for the sinusoidal fit are manually specified in the corresponding text boxes. A click on the “Fit sines” button runs the “beta_fit.m” script, which calculates first an initial estimate of the sinusoidal parameters, and then fits data to a sinusoidal model $x = x_0 + A \sin(\omega t + \phi)$ using “nlinfit.m” (from MATLAB Statistical Toolbox) for least squares nonlinear regression. The three parameters to adjust are offset (x_0), amplitude (A) and phase (ϕ), whereas the frequency ($\omega = 2\pi f$) is imposed according to the stage driving frequency (f). For optically trapped organelles in a living cell, natural cell activity was observed to create slow drifts, with eventual uncontrolled particle movements superposed to the actual sinusoidal motion in response to stage driving. In order for the model to fit to the actual particle trajectories, the time series was split in different blocks (corresponding to one single driving cycle each), so that the offset parameter could re-adjust following the center of the oscillations at all times, as illustrated in Figure 3.6.

Finally the average amplitude in physical units (A_{vid}) and Volt units (A_{QPD}) are determined from the fit results, which leads to the result of β , with its associated error.

$$\beta = \frac{\langle A_{vid} \rangle}{\langle A_{QPD} \rangle} \quad (3.31)$$

$$\Delta\beta = \beta \sqrt{\left(\frac{\sigma_{A_{vid}}}{\langle A_{vid} \rangle}\right)^2 + \left(\frac{\sigma_{A_{QPD}}}{\langle A_{QPD} \rangle}\right)^2} \quad (3.32)$$

3.3.3 Passive measurements

The software analysis software uses MATLAB’s Fast Fourier Transform (FFT) in the calculation of the power spectral density for the passive time series. Power spectra are smoothed by averaging over blocks of neighbouring frequencies (n_b points), and then averaged for all time windows (N_w passive recordings repeated on the same particle). The number of points for blocking in the frequency axis is manually introduced in the passive panel GUI. We used $n_b = 10$ for our analysis.

The “Passive check” button displays an overview of the passive recordings as seen in Figure 3.7. In the event of any temporary events, long term drifts or new particles coming into the trap (that would invalidate the initial calibration), the change in conditions may show up as jumps on any of these evaluated indicators. The “Show single” button lets the user check individual measurements, in case some of them have signs of problems. For example, passive measurement #9 in the data shown in Figure 3.7 has a similar average voltage than the rest (as seen in the lower left plot), but the peak in the mean squared difference (comparing spectra shapes) flags a difference from the general trend. When looking at the individual spectra shown in Figure 3.8 one can observe a two broad protrusions in experiment #9 (within 50-400Hz) that are not on the reference one. Since it is clearly something particular from this measurement only (possibly due to biological activity, or a temporary mechanical disturbance on the system during this 3s measurement), it could be safely excluded from the final average by using the corresponding check-button in the program interface.

One of the side results directly from passive recordings is a first (rough) estimation of an effective trap stiffness can be calculated from passive measurements using the equipartition theorem:

$$\kappa_{ET} = \frac{k_B T}{\sigma^2} \quad (3.33)$$

where σ^2 is the variance in the trapped particle’s position (due to Brownian motion). Calculated for each passive measurement, it also serves as a way to detect changes in the trapping conditions. Note that κ_{ET} contains the effect of elastic components of the medium and the actual trap stiffness, both imposing constraints on the natural particle thermal agitation. For that reason, the trap stiffness values obtained with the equipartition theorem would hardly ever match with the actual trap stiffness in this context, even though that would work fine in a noise-free purely-viscous environment). Hence the need for the active-passive calibration process to isolate the actual trap stiffness from the rest of the contributions.

A final average passive power spectrum is calculated using all passive recording (except the ones that were manually excluded), and the values of the power spectral density were evaluated at the specific frequencies of interest corresponding to the active driving frequencies. An illustrative example for an averaged spectra in optically trapped lipid granules inside *S. Pombe* is shown in Figure 3.9. The peaks within the 80-300Hz may be due to mechanical resonances in

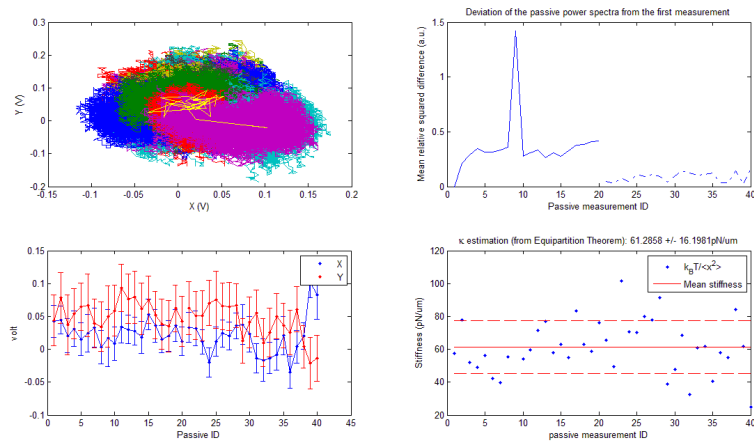


Figure 3.7: Passive data overview to detect possible problems: particle trajectories (upper left); a normalized difference indicator of each spectra from the initial one (upper right), the evolution of the average value along different passive recordings (lower left), and a rough estimation of trap stiffness based on the equipartition theorem.

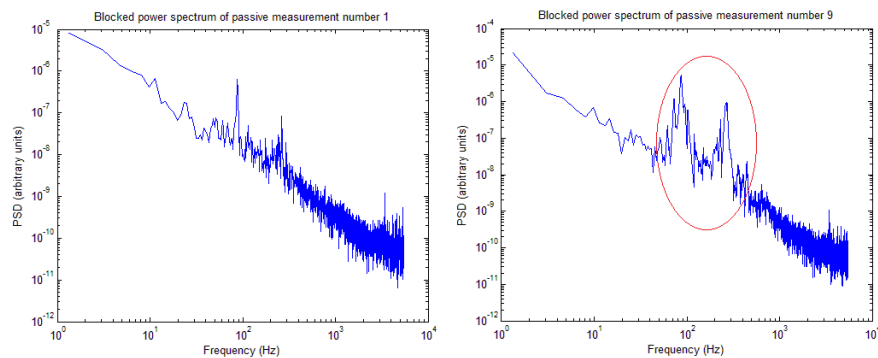


Figure 3.8: Blocked passive spectra of recordings #1 (left) and #9 (right). A large unexpected protrusion in the spectrum of measurement #9 is observed in the range of 50-100Hz, whereas in the spectrum of measurement #1 there is only a smaller noise peak localized at 80Hz (out of the calibration frequency range).

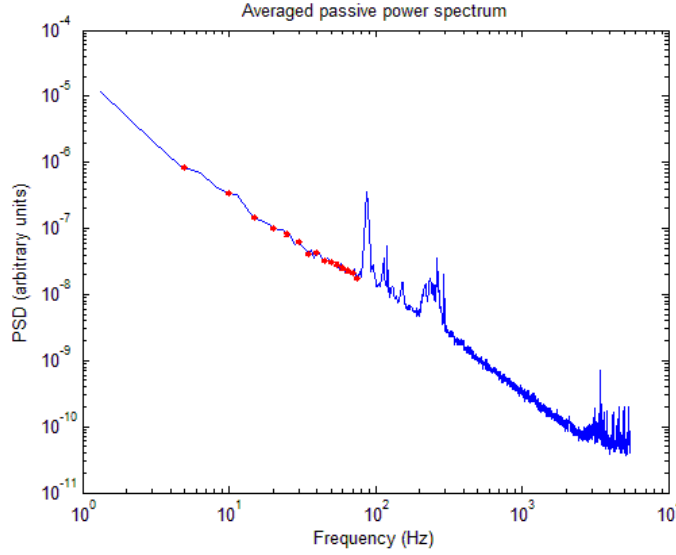


Figure 3.9: Average passive power spectrum of an optically trapped lipid granule in a *S. Pombe* cell, with marks at the specific frequencies to be used for trap calibration (those paired with active measurements).

the system. The errorbars at any frequency of interest are given by:

$$\Delta P(\omega)/P(\omega) = 1/\sqrt{n_b N_w} \quad (3.34)$$

3.3.4 Active measurements: checking and fitting

This is the core of the data analysis, and most time-consuming part, in which the sinusoidal active time series are analysed to quantify the stage and particle moving amplitudes, and the phase delay between them. The active data analysis is activated with the “Fit all” button, which runs the script “fitting_phase.m”. Optional checkboxes in the interface allow to specify fitting conditions and generate additional plots.

- “drift correction”, when enabled, allows for a moving offset parameter in the fitting routine, which adapts to the centre of the sinusoidal oscillations along the time series in small blocks of 2 cycles. This is useful to compensate for uncontrolled long-term drifts along the time series (which is quite significant in the intracellular environment), in order to provide a more accurate estimation of particle oscillation amplitudes.
- “account for mass” option enables a parabolic fit in the κ vs frequency results (rather than calculating an average κ across the different frequencies) to account for the inertial term $-\omega^2 m$. This option was not used

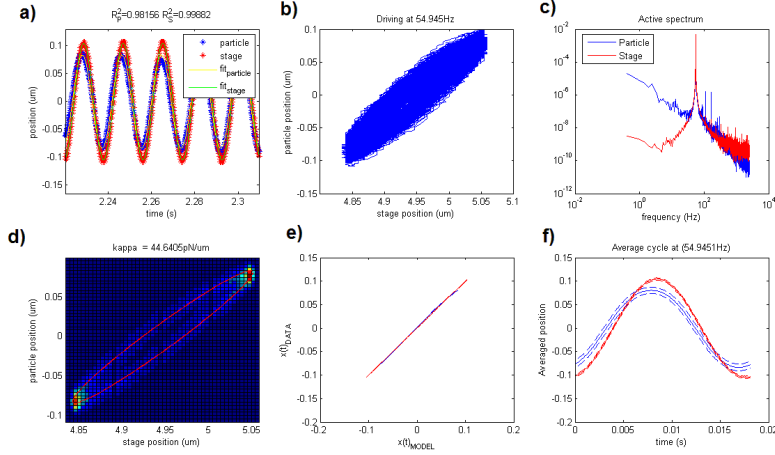


Figure 3.10: Example of active data analysis for an optically-trapped lipid granule with a 55Hz sinusoidal stage oscillation. a) particle and stage trajectories (zoomed in, with sinusoidal fit and R^2 coefficients for each indicating goodness of fit). b) particle vs stage position (elliptical shape). c) power spectra of stage and particle trajectories, with a spike at the driving frequency. d) 2D histogram of particle-vs-stage driving plot (showing an ellipse shadow), with overlapped fitted model (red line), e) particle (blue) and stage (red) average trajectories against the sinusoidal model. f) Average particle and stage cycle at this driving frequency, mean (continuous) and standard deviation (dashed lines).

in the results presented in this chapter because the inertial term is not important at low frequencies (as confirmed by the measured trap stiffness not changing significantly over the explored frequency range).

- “show each frequency fit”, when enabled, would display intermediate results for each sinusoidal fit, allowing the user to have an overview of each active measurement, and check that the particle is responding as expected to the stage sinusoidal perturbations.

For each active measurement, the program automatically fits the parameters of the stage and particle trajectories and displays the results, as seen in Figure 3.10. One can use this plots on active measurements to visually check that the particle moves as expected in response to the sinusoidal stage perturbation. Both trajectories have a clear sinusoidal shape (the particle one is typically noisier due to thermal fluctuations), with a certain phase delay between them that is related to the viscoelastic properties of the medium.

Regarding phase, the particle is always observed to have its maximum elongation slightly before the stage peaks (i.e. the delay $\Delta\phi = \phi_S - \phi_p$ is positive). Note that even though the particle moving before the stage may seem counter-intuitive, this is the expected behaviour when the inertial term is negligible

compared to the competing external forces (trap and viscoelastic drag).⁶In the general case, for an arbitrary viscoelastic medium, the phase delay takes a value between $0 < \Delta\phi < \pi/2$, with the particle maximum elongation peak taking place before the stage maximum elongation. Higher phase delays indicate the medium being more viscous-like, while smaller phase delays indicate the medium being more elastic.

Regarding the shape of the trajectory, the particle responds in a sinusoidal fashion to the applied stage perturbation. In occasions there may be deviations from this expected motion which needs to be looked in detail. One way of detecting that is by looking at the goodness of the sinusoidal fit. R^2 values below 0.9 were taken as a clear sign that the particle trajectory had some kind of deformation. Another visual way to detect this kind of problems is looking at the particle-vs-stage position response graphs in Figure 3.10 (upper middle trajectory and lower left elliptical fit). When two de-phased sinusoidal signals are plotted against each other one should typically observe an elliptical shape, with an eccentricity depending on the delay between the two signals, as seen in the example. However, if the particle motion is not sinusoidal, the ellipses would look distorted too. One can also look at the average trajectories plotted against the sinusoidal model, which should look like a straight line provided that there are no major deformations in the measured trajectories.

Checking the shape of the trajectory is a good way to find out whether the particle stayed within the linear region of the QPD detector or not. The trajectory may diverge from the sinusoidal model in the region of maximum elongation (reporting lower elongation than what is expected for a sine) if the particle is being dragged out of the QPD linear range, indicating that a smaller driving amplitude would be preferred.

Other sources of disturbances from the expected elliptical driving behaviour could be a e.g. physical obstacle blocking part of the particle's movement in one specific direction (e.g. other objects, a dense regions of the cytoskeleton, cellular membranes...). Cropped sinusoidal trajectories may lead to an underestimation of the particle amplitude response corresponding to a certain stage perturbation, which would in turn produce a result which is lower than the actual trap stiffness, hence, this measurements should be discarded (or repeated with a smaller driving amplitude).⁷

⁶This counter-intuitive behaviour can be understood e.g. thinking of the simple model of a particle with negligible inertia trapped in a purely viscous medium in motion. The particle would react to the instantaneous viscous drag force by sitting at a position that is proportional to the medium velocity ($k_{trap}x_p(t) = \gamma v_s(t)$), so that external forces are equilibrated. In that case, for a sinusoidal stage perturbation $x_s(t) = A_s \sin(\omega t)$ the medium would flow at a speed $v_s(t) = \omega A_s \sin(\omega t + \pi/2)$, so the particle position $x_p(t) = \gamma \kappa_{trap}^{-1} v_s(t)$ would be "advanced" $\pi/2$ respect to the stage position. On the other hand, if the medium was purely elastic, the force experienced by the particle would be proportional to the medium displacement ($\kappa_{trap}x_p(t) = \kappa_{medium}x_s(t)$), so there would be no phase delay between the stage and particle trajectories. Viscoelastic media lay in between these two extreme cases, with phase delays within $0 < \Delta\phi < \pi/2$.

⁷A further implementation of the active-passive calibration method described in next chapter included real-time QPD vs stage signal monitoring in a LabVIEW interface, to detect this kind of issues *in situ*, so that driving parameters could be re-adjusted, if needed, during

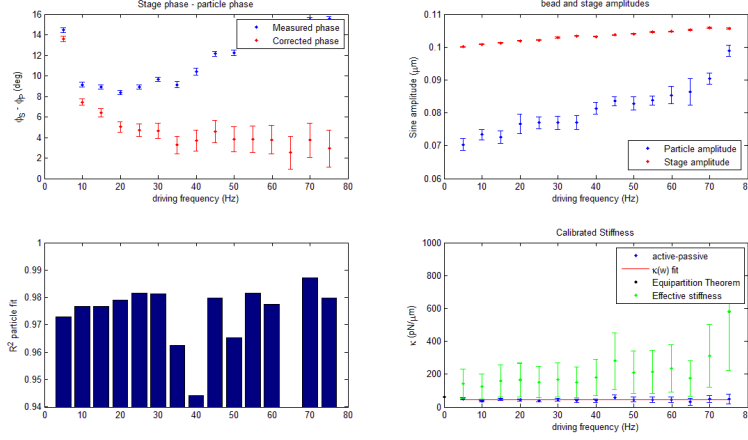


Figure 3.11: Results summary of active analysis on particle (blue) and stage (red) trajectories for each driving frequency, including phase delay (corrected for card t_{delay}), sinusoidal amplitudes, goodness of fit (R^2) for the particle trajectory, and stiffness results including active-passive trap calibration (blue), average value (red), the estimation from equipartition theorem (black), and the effective stiffness (green) including both the trap and the medium elasticity.

Finally, the amplitude of the particle displacements was checked to be lower than the stage amplitude. Some measurements showed particle amplitudes higher than the stage amplitude, and were discarded due to its objectionable physical meaning. We attribute these cases possibly to an overestimation of the β position conversion factor.

3.3.5 Trap calibration and viscoelastic parameters

At the end of the automatic active-data analysis the calibration results are presented as a function of the driving frequency, as shown in Figure 3.11. The results include the phase delay $\Delta\phi$ for the fit results (blue) and its corrected value (red) using Equation 3.29, the particle and stage amplitudes, and the goodness of the sinusoidal fit in the particle trajectory (to detect deviations from the expected sinusoidal trajectory). The results for the trap stiffness may be compared with the initial estimation coming from the equipartition theorem (black) and the effective spring constant at different frequencies (green), containing the elastic forces of both the trap and the surrounding medium. For that reason the effective spring constant is normally higher than the actual trap stiffness (blue dots).

Another graph to observe the trap stiffness results only is shown in Figure 3.12. At this range of frequencies the inertial $\omega^2 m$ vanishes, and the trap stiffness is the same for all the experiments.

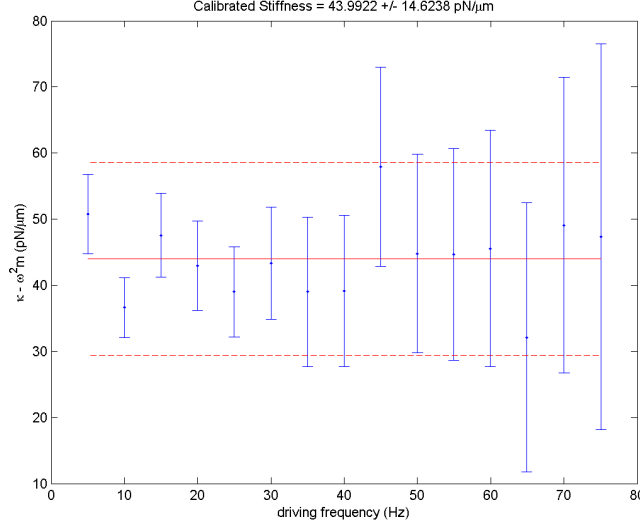


Figure 3.12: Calibrated trap stiffness at different driving frequencies (blue) and average value (red) with error bars, following the procedure described in subsection 3.1.3

ness is independent of the frequency (apart from a certain statistical variation around the average value). In the event of significant trends or jumps in the $\kappa(\omega)$ graph, that may indicate uncontrolled drifts or changes in the trapping conditions, which can be confirmed by looking at the preliminary checks that have been previously described. Any measurement at a specific frequency (or a certain frequency range) may be excluded from the final κ_{av} calculation, if there is a reason for that, by disabling the corresponding button in the “active measurements” panel.

The errorbars in κ can be split in the different contributions from each parameter involved in the trap stiffness calculation. An example of error contributions as a function of driving frequency is shown in Figure 3.13, where we observe that the uncertainty in β and $\Delta\phi$ are the dominant terms contributing to the uncertainty in κ .

The friction retardation spectrum $\tilde{\gamma}(\omega)$ is calculated as a side result of the active-passive measurements (following Equation 3.23), with its real part corresponding to the viscous drag component, and the imaginary part corresponding to the elastic component (which is significant in viscoelastic media, but zero in purely viscous media). The fact that the imaginary part of $\tilde{\gamma}(\omega)$ does not vanish towards lower frequencies indicates that there is some static elasticity in the medium. This prevents us from using an explicit formula specified in [4] to find out β directly from active-passive recordings: $\beta = 2k_B T \cot(\Delta\phi) / (\omega P^V \kappa^V)$, which is only valid for media with vanishing static

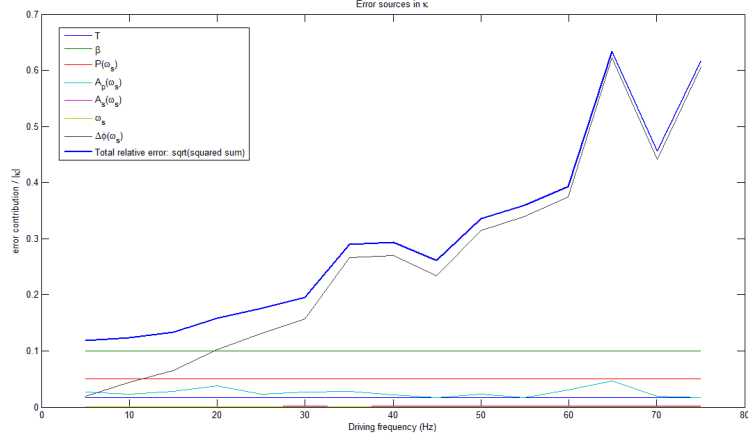


Figure 3.13: Relative error contributions to trap stiffness from the different measured parameters

elasticity, with $\lim_{\omega \rightarrow \infty} \text{Im}\{\tilde{\gamma}(\omega)\} = 0$. Hence the need for a dedicated experiment to determine the voltage-to-position conversion factor, as we did in this chapter.

Finally, the “G modulus” button in the user interface runs the “Gmodulus.m” script. This calculates and displays the G modulus at different frequencies, using Equation 3.26, the particle radius (specified in the interface), and its associated error bars. An example is shown in Figure 3.15. Note that due to the small size of lipid granules (close to the diffraction limit), there is a considerable uncertainty on the measured particles from video images, which is taken into account in the error bars. Lipid granule diameters were estimated to be in the range of $(0.6 \pm 0.1)\mu\text{m}$.

3.4 Results for different lipid granules

3.4.1 Calibrated trap parameters

Active-passive calibrations were carried out in 29 different lipid granules in cells from 6 different *S. Pombe* sample preparations. Those measurements that had clear evidence of changes in the trapping conditions (during the $\sim 3\text{min}$ calibration process), following the checks previously described, were considered invalid. The results for the 22 successful trap stiffness calibrations are displayed in Figure 3.16. The obtained trap stiffness (κ) varies from $4\text{pN}/\mu\text{m}$ to $84\text{pN}/\mu\text{m}$ depending on the trapped object, while the position calibration factor (β) varies from $0.15\mu\text{m}/V$ to $0.89\mu\text{m}/V$. The statistics on the measured parameters are summarized in Table 3.1.

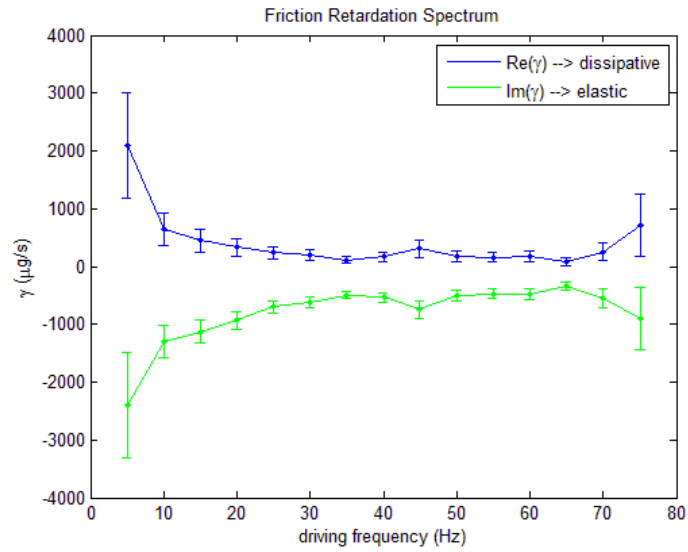


Figure 3.14: Friction retardation spectrum (real and imaginary components)

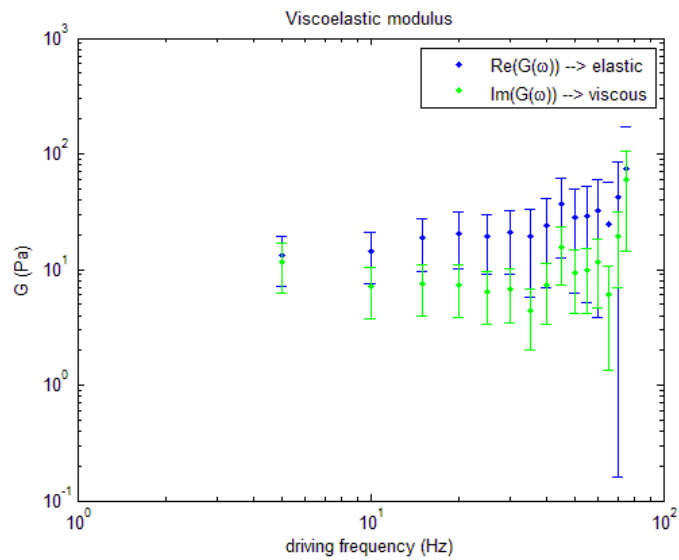


Figure 3.15: G modulus for a lipid granule trapped in water

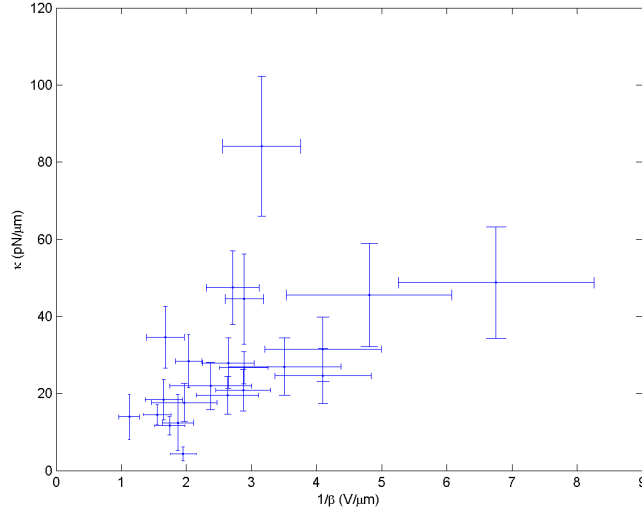


Figure 3.16: Trap stiffness calibration results (κ and $1/\beta$) for different lipid granules

	κ^V (pN/V)	β ($\mu\text{m}/V$)	κ (pN/ μm)
μ	10.6	0.427	28.4
σ	5.5	0.173	17.5
σ/μ	51%	40%	61%
$\overline{\varepsilon_{rel}}$	20%	17%	28%

Table 3.1: Statistics of calibrated trap parameters for different lipid granules (with constant laser power): mean (μ), standard deviation (σ), coefficient of variation (σ/μ), and average measurement uncertainty ($\overline{\varepsilon_{rel}}$).

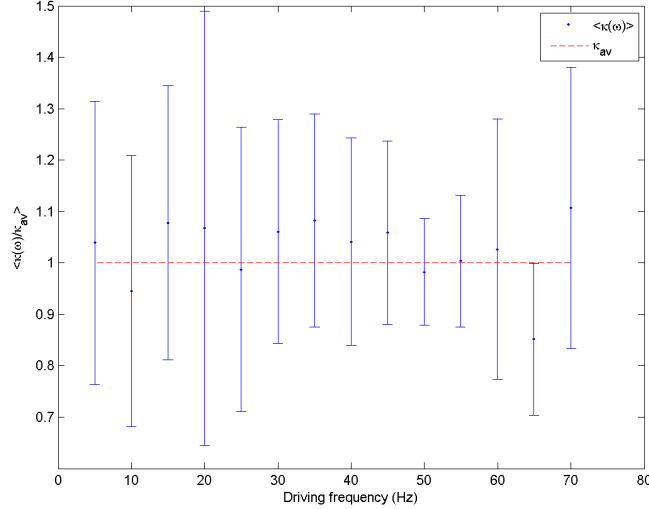


Figure 3.17: Normalized trap stiffness as a function of the driving frequency, averaged over different lipid granules. Error bars show the standard deviation for each driving frequency.

The broad distribution on trap stiffness across different lipid granules (with a coefficient of variation of 61%) can probably be attributed to a combination of factors such as different granule sizes, shapes, and refractive index (related to granule composition). The spread in trap stiffness values supports the need for an *in situ* calibration method to assess the strength of the trap specifically for each individual object.

3.4.2 Frequency dependence

The measured trap stiffness is expected to be independent of the frequency as long as the inertial term can be neglected. In order to look at the global dependence of the trap stiffness on the driving frequency, one can first normalize the datasets of each object by their mean stiffness ($\kappa(\omega)/\kappa_{av}$), and then calculate the average for each frequency across all different granules, as shown in Figure 3.17. There is no major dependence of the measured trap stiffness on the driving frequency, which allows us to confirm that the calibration method works as expected in the explored frequency range. As a positive note, biological activity in living *S. Pombe* does not seem to be seriously interfering with the active-passive calibration in the frequency window from 5Hz to 75Hz.

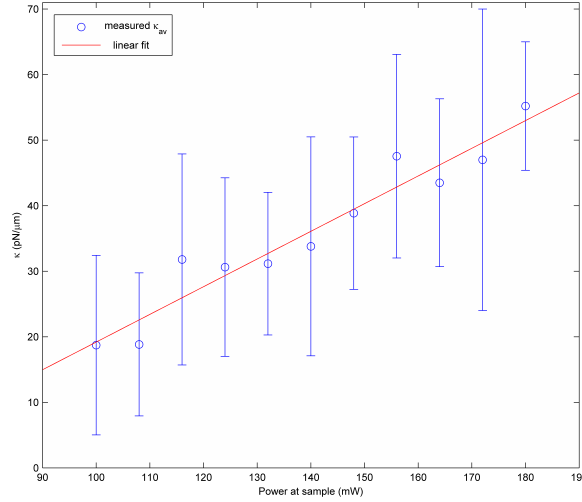


Figure 3.18: Trap stiffness measurements on a lipid granule at different laser powers

3.4.3 Power dependence

The strength of an optical trap is proportional to the laser power. We tested that with a series of active-passive calibrations on a single lipid granule at varying laser powers. As shown in Figure 3.18 the trap stiffness increases with the power at the sample, which can be well described by a linear trend.

3.4.4 G moduli

The average of the obtained G moduli for all different lipid granules was calculated to observe the global frequency-dependent viscoelastic behaviour in *S. Pombe* cells. The results presented in Figure 3.19 show that the real and imaginary parts of the G modulus have similar magnitudes, which vary from 4Pa to 30Pa within the explored frequency range. There is a clear growing trend in the real and imaginary parts of the average G modulus, which can be well described by a model of the form $G \sim \omega^\alpha$, with an exponent around 0.75 [71].

The measured values are in the range of other microrheology studies in actin network [72, 73], comparable to the measurements in the cytoplasm of different cell types such as *Dictyoselium* [74], slightly larger than measurements in HeLa, HepG2 and THLE cells [75], and slightly lower than in PC3 human prostatic adenocarcinoma cells [76]. Finally, the results are comparable to results from previous studies in *S. Pombe* cells shown in [71] based on re-processed data from [77].

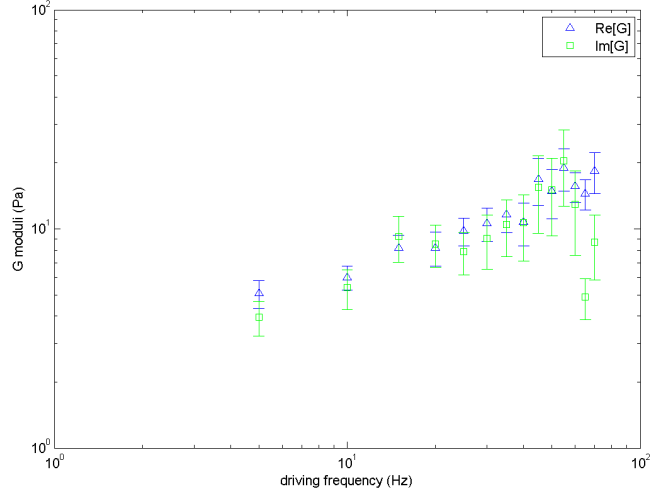


Figure 3.19: G moduli averaged over different lipid granules. Errorbars correspond to the standard error of the mean (SEM).

3.5 Conclusions

We applied the active-passive calibration method for viscoelastic media, based on the Fluctuation Dissipation Theorem (FDT) to optically-trapped endogenous lipid granules in living *S. Pombe* cells. This is a first proof of principle for the FDT method in a living environment using the stage-driving approach [71]. Compared to previous measurements in actin-gel, we observed a need to introduce several checks in the data analysis process to monitor possible changes in the trapping conditions and uncontrolled perturbations due to cell activity. We developed a MATLAB package for visualising active-passive measurements, fitting sinusoidal trajectories, and calculating the trap stiffness and the local viscoelastic parameters.

The measured trap stiffness (κ) is essentially constant over the explored frequency range (5Hz to 75Hz), which confirms that biological activity in the living *S. Pombe* cells does not invalidate active-passive calibration at these frequencies. As expected from any optical trap, the trap strength increases with laser power.

Trap stiffness results are highly dependent on the trapped object, which reflects the diversity in the optical characteristics of naturally-occurring intracellular organelles and their local environment, and justifies the need for object-specific optical trap calibrations. The ability to perform local calibrations *in situ* is of great advantage compared to other approaches relying on *ex situ* calibrations [36]. External calibrations can hardly take into account all the specific

conditions that may contribute to the trapping efficiency inside the cell, such as local aberrations of the beam, heterogeneities in the refractive index of the cytoplasm, and the specific shape and structure of the trapped organelle.

Further implementations of this method have been reported recently using the laser-driving approach (which is able to explore high frequencies, and perform faster calibrations). For example, Blehm et al. [78] measure molecular motor stall forces in A549 cells with an optical trap that is calibrated on-the-fly with the laser-driving approach.

In conclusion, the active-passive calibration method for viscoelastic media based on the FDT has proved to be a valid approach for calibrating optical traps *in situ* within the cytoplasm of living cells.

Chapter 4

Momentum-based optical force measurements: validation inside A549 cells

4.1 Introduction

Optical force is the result of a change on the momentum of light. Hence, one can directly quantify a force exerted onto a sample with a light beam by directly measuring the global change in the beam's momentum [5, 6, 7], as introduced in Chapter 1. Even though this direct force (DF) method is still not the most common approach in the optical trapping community (where traditionally a trap-stiffness calibration is most widely used), DF measurements have a clear potential advantage when it comes to mechanically complex environments. The reason is that the calibration of the beam's momentum does not rely on any assumption on mechanical sample properties for force calibration, just on the ability to capture all the scattered light to quantify the momentum lost by the beam (and hence transferred to the sample as an optical force).

The cell cytoplasm is an interesting example where its mechanical complexity prevents standard methods from being used for optical trap calibration. In the previous chapter we presented the Active-Passive Calibration (AP) as a valid possibility for quantifying optical forces in optically trapped organelles inside the cell, with the assumption of the cytoplasm behaving as a viscoelastic material. Even though the DF method can naturally provide force measurements without any assumption on the mechanics of the medium, it is to be seen how the force measurements may be affected by other cellular structures in the path of the beam, like organelles or the cellular membrane.

The global beam momentum change arises from the added contribution of all optical momentum transfers on the whole path of the laser beam, whenever there are changes in refractive index. This evidently includes the momentum

transferred to the trapped object, which produces the optical trapping force, but also any momentum exchanged at further layers in the sample, on other refractive/scattering structures. Even though most of the relevant momentum exchange is expected to concentrate in the trap region (where the beam is focused), it is interesting to evaluate how additional elements within the crowded cellular environment would affect force measurements, and whether the DF system calibration holds in this context.

For that purpose, in this chapter we present a series of calibrations with an experimental system integrating both DF and AP force detection methods. The calibrated piconewton-to-volt parameter (α) is compared to the nominal system calibration based on momentum analysis, in order to validate optical force measurements in the cytoplasm of living cells.

4.2 Experimental system for momentum-based force measurements and active-passive calibration

4.2.1 System requirements for momentum-based force measurements

Both the active-passive calibration method and the direct force method based on momentum transfer use a Back-focal-plane-interferometry configuration. Hence, the two methods can be easily integrated provided that the (more restrictive) conditions for the momentum-based method are fulfilled [5, 6, 7]:

- Use a Position Sensing Detector (PSD) rather than a Quadrant Photo Diode (QPD). Both types of detectors can provide a signal that is proportional to the trapped object's position for a certain range, as required for trap stiffness calibrations. But crucially only the PSD detector retrieves a signal that is proportional to the centre of mass of the light distribution $I(x,y)$ over the whole detector (with efficiency Ψ and half-size R_D). This is key for providing an accurate measurement of transverse momentum of the beam[5, 6].

$$\begin{aligned} S_X &= \Psi \int \int \frac{x}{R_D} I(x,y) dx dy \\ S_Y &= \Psi \int \int \frac{y}{R_D} I(x,y) dx dy \end{aligned} \quad (4.1)$$

- Use a high-NA condenser lens to capture all the forward-scattered light. The maximum NA used in detection is limited in practice by the refractive index of the trapping medium, so in experiments in water ($n_{water}(1064nm) = 1.32$) we expect a cone of forward-scattered light corresponding to 1.32 NA (with the marginal rays being the ones scattered at 90° at the sample from the optical axis).
- The condenser lens should fulfill the Abbe sine condition [5, 6], so that any location at a lateral distance (r) from the optical axis at the back focal plane (BFP) of the condenser corresponds to one specific direction

at the sample plane, following $r = f'n \sin \theta$ (where f' is the focal length, n the refractive index of the medium, and θ the direction of propagation with respect to the optical axis). This is automatically fulfilled by using an aplanatic condenser lens, corrected for spherical and coma aberrations. Crucially, the distance r from the optical axis at the back aperture is then proportional to the transverse momentum component of photons scattered at direction θ : $p_r = p_0 n \sin \theta$ ¹, with $p_0 = E_0/c$ being the momentum of a photon in vacuum (with energy $E_0 = h\nu$), and c the speed of light. At the BFP the intensity distribution $I(x, y)$, or energy per unit time and surface, corresponds in fact to the momentum decomposition of the laser beam, following the relation:

$$p_x = \frac{p_0}{f'} x, \quad p_y = \frac{p_0}{f'} y, \quad (4.2)$$

- Minimize light losses in the upper water-glass interface. Due to the limited size of the condenser lens, there will be geometrical light losses if one performs the experiments too far from the upper surface of the sample. In that situation, light scattered at higher angles would be lost because of the condenser lens acting as a diaphragm, and aplanaticity may be compromised because of spherical aberrations. This can be avoided by working near the top surface of the sample, close to the condenser lens. Note that this may not be possible (e.g. on a typical $100\mu m$ thick sample) with a high NA oil-immersion objective (like the one used in the previous chapter) due to its very limited working distance and spherical aberrations as one focuses deeper into an aqueous sample. A water immersion objective (with longer working-distance) can easily overcome this problem and stably trap at the top of the sample chamber, as illustrated in Figure 4.5.

Under that conditions, the PSD signals described in Equation 4.1 can then be directly related to the optical force components (F_X, F_Y), or the change rate in the total beam momentum (P_X, P_Y). If we consider single photons with initial momentum (p_x^{ini}, p_y^{ini}), before interacting with the sample, and final momentum (p_x, p_y), after crossing the sample, the total change rate in the beam momentum can be expressed as the addition of individual momentum changes experienced by all photons ($p_x - p_x^{ini}, p_y - p_y^{ini}$), which can be calculated by weighting every momentum component by the number of measured photons on that direction per time unit $I(x, y)/E_0$.

$$\begin{aligned} F_X &= \frac{dP_X}{dt} = \int \int (p_x(x) \frac{I(x,y)}{E_0} - p_x^{ini}(x) \frac{I^{ini}(x,y)}{E_0}) dx dy \\ F_Y &= \frac{dP_Y}{dt} = \int \int (p_y(y) \frac{I(x,y)}{E_0} - p_y^{ini}(y) \frac{I^{ini}(x,y)}{E_0}) dx dy \end{aligned} \quad (4.3)$$

¹That expression follows from the Minkowski definition for the momentum of a photon in a medium: $\vec{p} = \vec{p}_0 n$, where n is the refractive index of the medium and \vec{p}_0 is the momentum of the photon in vacuum [79]. This is the canonical momentum, used for describing displacements of a body in a host medium, as well as in diffraction theories.

This is actually equivalent to calculating a centre of mass of the momentum distributions, so following the relation between of the BFP positions and momentum components (Eq. 4.2), the optical force can be expressed as:

$$\begin{aligned} F_X &= \iint \frac{p_0}{f'E_0} (xI(x,y) - x^{ini}I^{ini}(x,y)) dx dy \\ F_Y &= \iint \frac{p_0}{f'E_0} (yI(x,y) - y^{ini}I^{ini}(x,y)) dx dy \end{aligned} \quad (4.4)$$

which can finally be related to the PSD signals from Eq. 4.1 resulting in a simple proportionality relationship between PSD signal and force:

$$\begin{aligned} F_X &= \alpha(S_X - S_X^{ini}) \\ F_Y &= \alpha(S_Y - S_Y^{ini}) \\ \alpha &\equiv \frac{R_D}{\Psi f' c} \end{aligned} \quad (4.5)$$

Note that the calibration factor α relating voltage to force is independent of the sample, and it only depends on parameters of the force detection arm such as the detector efficiency (Ψ) and half-size (R_D), the system focal length (f') and the speed of light c . Later in this chapter we quantify the system for our particular system.

4.2.2 Experimental setup

The set-up used in this chapter consists of holographic optical tweezers built on an inverted Nikon Eclipse TE-2000E microscope, as described in Chapter 2, with the addition of the direct force detection arm described in [7] collecting the forward scattered light from the sample to analyse the changes in the beam momentum. A general overview of the setup is shown in Figure 4.1.

The light sources are an ytterbium fiber laser for optical trapping (IPG YLM-5-1064-LP, 5W@1064nm), a mercury (Hg) lamp for fluorescence excitation (Nikon Intensilight C-HGFI), and the microscope halogen lamp for bright field illumination. Lenses L1 ($f'=30\text{mm}$) and L2 ($f'=100\text{mm}$) form an inverted telescope that expands the initial 5mm laser beam to overfill the 12x16mm surface of the Spatial Light Modulator (SLM, Hammamatsu X10468-03). The SLM is conjugated with the back-aperture of the microscope objective (OBJ, Nikon Plan Apo 60X, 1.2NA, 0.27WD, WI) using a de-magnifying telescope with lenses L3 ($f=150\text{mm}$) and L4 ($f=100\text{mm}$), sending the laser beam to one of the epi-fluorescence ports of the microscope. A dichroic mirror (DM1) reflects the incoming laser beam (at $\lambda = 1064\text{nm}$) towards the objective and sample, while letting visible light pass through for bright field and fluorescence imaging.

A condenser lens (COND, Nikon T-CHA, 1.4NA, Aplanat) collects the forward-scattered laser light after the sample, while delivering illumination from the microscope's halogen lamp to the sample for bright-field imaging. A second dichroic mirror (DM2) reflects the collected laser light to the PSD while letting the microscope illumination light (visible) pass through in the opposite direction. The light intensity distribution at the back aperture of the condenser is projected by a relay lens (L5, $f=40\text{mm}$) onto the PSD (Thorlabs PDP90A), with

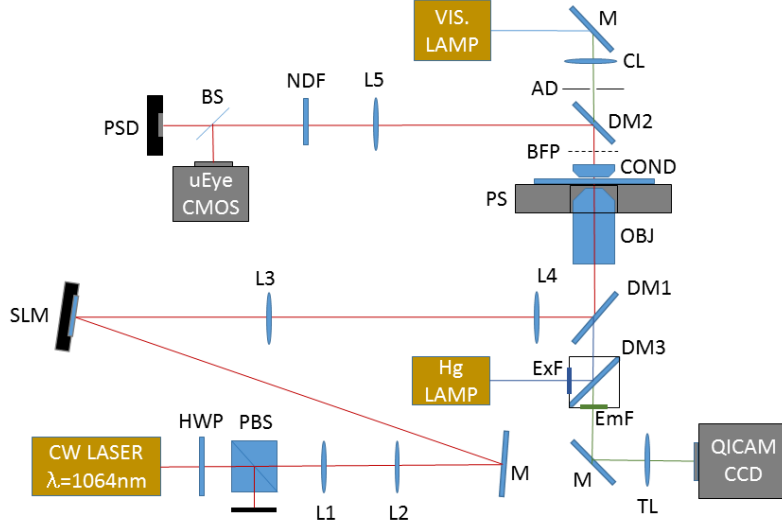


Figure 4.1: Setup for optical trapping, direct force detection, and active passive calibration.

a $\sim \times \frac{1}{4}$ magnification factor. The whole length of the detection arm, from the condenser to the PSD, measures 307mm.

The conjugation between the PSD plane and the BFP of the the condenser can be precisely adjusted with an axial-shifting cage-system mount for the relay lens. When the PSD is at the exact conjugate plane of the BFP, its signal should exclusively account for the transverse momentum of the beam (angular distribution), and be independent on the trap position within the field of view of the condenser lens. We adjusted the PSD axial position by translating the trap using a motorized micrometer on the last telescope (L4) on the trapping system, or using a cyclic sequence of linear-phase holograms on the SLM to displace the trap. Then one can continuously adjust the axial position of the detector or the relay lens until the oscillations on the PSD signals are minimized.

We use a 1.4NA condenser lens (oil immersion) to make sure that even the light scattered at very large angles ($\sim 90^\circ$) will be collected. Due to the high-NA condenser being oil immersion, the detection arm often needs to be moved vertically to allow some space for placing and removing samples on the microscope. Hence, the vertical position of the condenser (with the whole force detection arm) needs to be manually adjusted every time a new sample is placed onto the microscope. For that purpose, an object of interest at the target within the sample is trapped, and the optimal condenser position can be found

	PSD X	PSD Y	CCD X	CCD Y
Piezo MOD1 +	+	no change	-	+
Piezo MOD2 +	no change	-	+	+

Table 4.1: Sign factor for the PSD and CCD signals in their axis when movements are induced in the positive MOD1 and MOD2 channels of the piezoelectric stage. A more detailed angle analysis is performed in the next chapter.

looking at the BFP maximum light capture e.g. by monitoring the PSD SUM channel (proportional to the collected light power) and adjusting the height of the condenser lens until that signal is maximized.

Samples are placed on a piezoelectric stage (PS, Piezosystem Jena, Tritor 102 SG, with driver NV40/3CLE) for active driving measurements. The stage is positioned on the microscope stage with its lateral driving axes aligning with the PSD axes. Due to the considerable thickness of the piezoelectric stage, a custom objective mount extender (from the microscope objective revolver) is used to let the microscope objective reach the samples through the central aperture in the piezoelectric stage.

Bright field images are obtained using a CCD at the camera port of the microscope: QImaging QICAM IEEE 1394 FireWire (12-bit Monochrome, 1382x1040 pixels, 4.65 μ m pixel size, 10fps full-frame rate). The camera was attached to the optical table, rather than the microscope body itself, to prevent mechanical noise from the camera cooling fan affecting our measurements (undesired vibrations at certain frequencies were observed when the camera was turned on when in contact with the microscope). With the 60X objective and a 1.5X additional magnification (using the optional microscope tube lens) the pixel calibration relating sample dimensions to CCD pixels is measured to be $53.32 \pm 0.17 \text{ nm/pixel}$, using a calibration grid. There is only a 3% difference with respect to the expected pixel size using the nominal magnification.

The relation between the positive direction in the piezoelectric stage axis (MOD1 and MOD2), the PSD axis (X,Y), and the microscope CCD axis are summarized in Table 4.1. Note that even though the positive MOD1 (piezo) and PSD X directions match, there is a sign difference between the piezo MOD2 and PSD Y signals, which needs to be corrected for active-passive calibrations in the MOD2 direction. Also one should take into account that the CCD axis are tilted with respect to the driving axis, with the positive MOD1 and MOD2 driving directions corresponding to movements towards the 4th and 1st quadrants respectively. For the calibration of the position-conversion factor β (defined in Chapter 3) a rotation of axes is applied to the video-tracked trajectories in order to measure the full amplitude of the sinusoidal particle fluctuations, rather than its partial projections in the original CCD axes.

4.2.3 Compatibility of imaging and force detection

Monitoring the trap region during the experiments is specially relevant for live cells, where the cell activity may be producing changes in the trap environment. Hence, it is convenient to make force detection compatible with simultaneous microscope imaging, in order to be able to monitor the trap region during the experiments. Wavelength differences allow to easily decouple visible illumination from infrared laser collection using a dichroic beam splitter within the illumination train of the microscope, between the lamp collection lens and the condenser lens. In this way, the forward-scattered laser light (infrared) is redirected to the relay lens and the PSD, while keeping the illumination column free of obstacles for sample illumination.

However, there is the difficulty of adjusting the microscope illumination for high contrast microscopy while keeping the force detection path obstacle-free. In order to find a balance between image contrast and brightness in Köhler illumination one would normally use the aperture diaphragm at the focal plane of the condenser. Closing the aperture diaphragm greatly increases the image contrast, effectively revealing structures with tiny refractive index changes that would not be visible otherwise (like organelles within the cell cytoplasm). The side effects of using a reduced aperture are:

- Brightness reduction: this may be compensated by increasing the voltage applied to the microscope halogen lamp, and increasing the exposure time of the camera.
- Decreased resolution when the aperture is smaller than the actual NA of the objective. Even though the resolution power of the microscope is then under-used, it is more important for us to prioritize image contrast so that we can actually see the cellular organelles we are interested in.
- Increased depth of focus: structures that are further away from the actual focal plane become visible on the microscope image. This is not convenient for optical sectioning, but it is actually beneficial for monitoring purposes in our case, since it is then possible to detect spurious organelles that may be affecting the momentum of the beam at other planes further from the actual trapping plane.
- Blockage on the force-detection path: closing the iris at the back aperture of the objective impedes the information on the angular composition of the scattered beam reaching the detector.

We need to reduce the illumination aperture in order to get enough contrast. However, on a force-detection experiment the condenser aperture should be kept free of obstacles. Hence an alternative method for reducing the aperture of the illumination beam is required in order to provide enough contrast to image the structures in the cell cytoplasm. We decided to use an external iris at an alternate plane within the illumination train, out of the force-detection path,

that would still allow us to reduce the aperture of the beam. The only conjugate plane of the condenser aperture within the illumination train was on an inaccessible space between the microscope lamp and its collection lens. Placing an iris at intermediate planes other than the actual aperture diaphragm has the effect of not only limiting the aperture but also partially cropping the field of view (whereas in Köhler illumination aperture and field diaphragms are completely decoupled). In spite of that, a good trade off was found when the iris was located just below the lamp collection lens, where we could effectively reduce the aperture of the illumination beam enough to make the structures in the cell cytoplasm visible, while keeping the relevant field of view mostly uniformly illuminated. That allowed us to get high contrast images to monitor the cell cytoplasm during force detection experiments, while keeping the forward-scattering collection path free of obstacles for force measurements.

4.2.4 Parameters of the momentum-based detection system

The parameter that converts voltage signal into force units can be calculated from measurable system parameters [7], following the relation:

$$\begin{aligned} F_x &= \frac{R_D}{\Psi f' c} (S_x - S_x^{ini}) \\ F_y &= \frac{R_D}{\Psi f' c} (S_y - S_y^{ini}) \end{aligned} \quad (4.6)$$

The power efficiency Ψ relates detector voltage reading (SUM) to the laser power at the sample (across all optical elements of the collection system), and it was measured to be $58 \pm 3 \text{V/W}$ in our system [7]. The sensor half-size is $R_D = 4.5 \text{mm}$ according to the manufacturer specifications. The effective focal length f' of the detection optics is such that $x' = f'n \sin\theta$, so that every position x' at the detector plane corresponds to an angle θ (measured from the optical axis) at the sample. In our case, this was measured to be $f' = 2.62 \pm 0.08 \text{mm}$ [7]. A detailed protocol for characterising the system parameters can be found in [80]. The last parameter needed is the speed of light c . Hence, the nominal voltage to force conversion factor in our system is:

$$\alpha \equiv \frac{R_D}{\Psi f' c} = 99 \pm 6 \text{pN/V} \quad (4.7)$$

Note that, for a given system configuration, the conversion factor α is independent of laser power and sample properties as demonstrated in [6, 7]. Additionally, there are offset values (S_{xo}, S_{yo}) corresponding to the signals when there is no force applied to the trapped object. This offsets may depend on the laser power, beam shape, trapped object, and even position within the sample, and they can be directly measured for every object (e.g. see baseline determination in molecular motor force measurements in next chapter). Note that when differential force measurements are made (e.g. for two different positions of a trapped object) the force increment/decrease can be measured as the subtraction of forces.

Filter ID	T (1064nm)	P_{sat} (mW)	α_{system} (pN/V)
No filter	1	70	99 ± 6
F1 (Thorlabs NE02B)	0.418	165	237 ± 14
F2 (Thorlabs NE04B)	0.485	140	204 ± 12
F1 + F2	0.203	340	488 ± 30

Table 4.2: Transmittance (T) for different ND filters, with powers at the sample corresponding to PSD saturation (Pmax), and resulting voltage-to-force conversion parameter α .

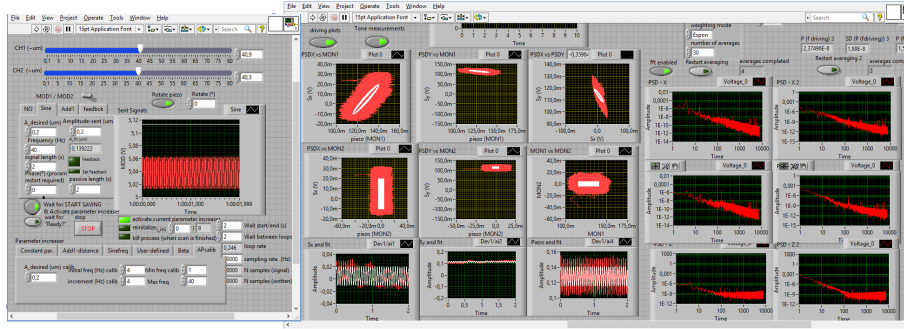


Figure 4.2: LabVIEW control interface for stage driving and PSD-piezo signal monitoring

Depending on the power at the sample, additional filters may be placed in front of the detector to keep the detector exposure to laser light below the saturation level of 4V in the SUM channel. Without any additional filter, the saturation level corresponds to a maximum power of $\sim 70\text{mW}$ at the sample. A set of neutral density filters were used to work at higher powers when needed. A good practice is to keep the SUM voltage within the upper central part of the voltage dynamic range, to have reasonable signal quality while preventing detector saturation during experiments. The transmittance (T) at 1064nm wavelength for the different filters we used are summarized in Table 4.2, together with the corresponding voltage-to-force conversion factors (α), and the maximum power at the sample P_{sat} that would saturate the detector. For the A549 experiments, the combination of filters F1+F2 was chosen, allowing us to use higher trapping powers without saturating.

4.2.5 Notes on active driving in AP calibration

The piezoelectric stage was placed on the microscope and manually rotated to get its driving axis aligned with the X and Y axis of the PSD. For each vesicle, the active-passive calibrations were carried out in this two orthogonal directions, corresponding to the PSD X and Y axes.

Regarding driving amplitude, again it is crucial to keep objects within the

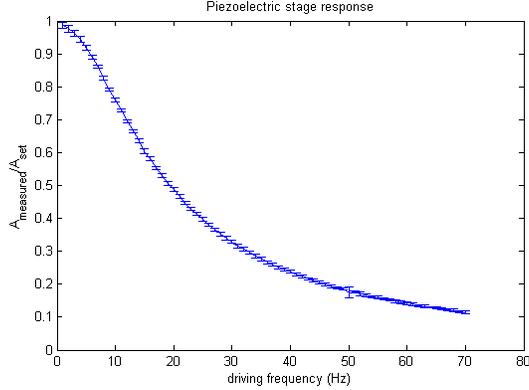


Figure 4.3: Response curve of the piezoelectric stage at different frequencies. The errorbars show the standard deviation for measurements for different driving amplitudes (at $0.1\mu\text{m}$, $0.2\mu\text{m}$, $0.5\mu\text{m}$ and $1\mu\text{m}$) and for two perpendicular driving directions (MOD1 and MOD2).

linear region of the trap. The amplitude response of the trapped object will vary from experiment to experiment, depending on particle size, the trap stiffness, and the mechanical properties of the medium. Live display of the PSD signals vs piezo driving on the custom LabVIEW software during active-passive (AP) calibration experiments enabled checking the calibration performance at a glance (Figure 4.2), also providing a first guess *in situ* for alpha calibration, and detecting movements in the perpendicular direction. Similarly to the previous chapter, the amplitude response of the piezoelectric stage decreases at higher frequencies. The ratio between the measured stage displacement (monitor channels) and the set driving amplitude (modulation channels) is shown in Figure 4.3.

4.2.6 Data acquisition and analysis

A custom LabVIEW package was developed for simultaneous live cell imaging, dynamic trap positioning², piezo-stage driving and monitoring, PSD signal recording, and active-passive calibration with a real-time first estimate of the measured parameters. Communication with the PSD (S_x , S_y , and SUM signal recording) and piezoelectric stage (modulation and monitoring) was carried out through a data acquisition card (NI-DAQ USB-6211), recording data at 15kHz sampling rate. After selecting and trapping the target object with the mouse interface, the active-passive protocol was activated. The active-passive calibration was carried out by alternating active and passive recordings in blocks

²The part of the LabVIEW software interface dedicated to holographic trap positioning was based on a customized version of “Blue Tweezers”, a package for holographic tweezers created at the University of Glasgow, which we modified for our purposes.

of 1s, typically from 4Hz to 70Hz. Having the passive measurements distributed along the whole calibration process allowed us to monitor drifts during the experiment.

At the start of each experiment the camera settings were automatically adjusted so that video of a small area around the trap could be recorded at a higher frame rate. This video was used both for the PSD signal-position calibration (β) and for visually monitoring the trap region during the calibration process. We used a region of interest (ROI) of 200x200 pixels (corresponding to 10.6 μ m square area around the trap location), which allowed us to go from the standard 10fps (full field of view) to 33fps (with ROI), which is convenient for the PSD signal-position calibration using video tracking. Additionally, the live video monitoring allowed us to detect and take note of potential accidents, like a new object jumping into the trap, that would invalidate the calibration.

Particle tracking of lipid droplets for β analysis was carried out with Video Spot Tracker ³, which is shown in Figure 4.4. The options we used for the tracking program were “optimize on” (to follow the organelle), “interpolate on” (slower tracking, but better accuracy), “symmetric” (as a first approximation for the diffraction spot generated by trapped objects in bright-field images), and size parameter R around a value between 5 and 15. R was readjusted for each particle to get the maximum contrast in the radial profile observed in the “debug-Landscape” window. In those cases in which the tracker lost the particle because of a fast change of position, the analysis was repeated with the “follow jumps” option activated (slower, but more robust against jumps). If the tracking was lost because of other objects coming into the trap during the calibration, that measurement was discarded.

4.2.7 Preliminary considerations for force measurements in heterogeneous media

If there are scattering elements in the path of the beam, either inside the sample (e.g. cell structures) or in other parts of the beam path (e.g. air bubbles within the condenser immersion oil) they are going to affect the beam.

The area of influence on the beam path follows a light cone of the 1.2NA beam focused in water, with an opening angle of 65.5 $^\circ$ from the optical axis. The implications for a beam focused after a 100 μ m-thick microchamber is that objects within a circular area of up to 418 μ m diameter at the base of the cone may have an effect on the beam. For experiments through a 10 μ m-thick cell, those structures within an area of 42 μ m diameter could interfere with the beam. The presence of scattering structures within this region other than the trapped object could potentially have an effect on the momentum-based measurements, and this motivates us to specifically study the system calibration in such-environment using an alternative method.

³The particle tracking software was developed by CISMM at UNC-CH, supported by the NIH NIBIB (NIH 2-P41-EB002025) and it is available at: <http://cismm.web.unc.edu/software/> (last checked 17/08/2016).

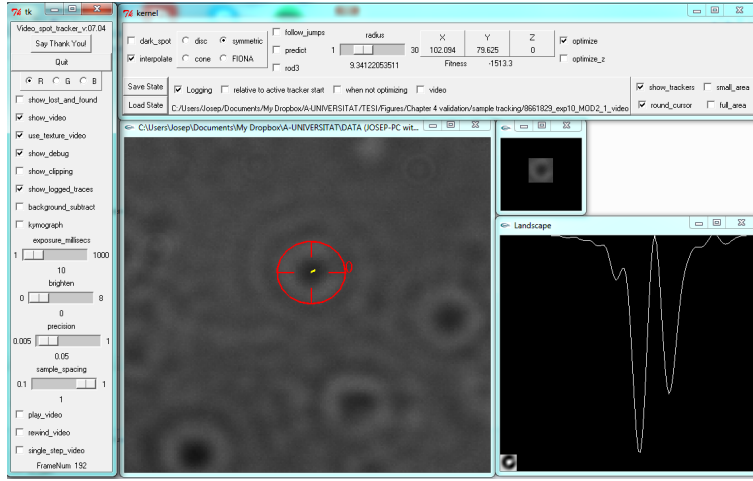


Figure 4.4: Snapshot of typical video tracking of a LD trapped inside an A549 cell during active-driving

There is a practical difference depending on whether obstacles are present before or after the trap. If there is a structure before the trap, it may have an effect on the way the beam is focused, which would change the trap geometry (including its stiffness) and the initial beam momentum (PSD signal offsets). No effect is expected though for the calibration constant of the momentum method, as long as all scattered light is collected. The situation is different when there are structures after the trapped object: which may or may not significantly affect the force measurement with the momentum method, and the voltage-to-position conversion factor (β) for the active-passive method. This is the most disadvantageous situation, since there might be a loss of information from the actual trapping plane (real forces in the sample, that we want to measure) and the detected signals based on the scattered light (measured forces). Upper structures are less of an issue for the active-passive calibration. Even if β may be affected by such structures, the measurements are still valid as long as the output signals are linear with the position of the trapped object within the driving range. The effective β can be locally calibrated for each vesicle, and the linearity of the position signal is something we routinely check during active data analysis, as described in the previous chapter, when we look at deviations on the particle trajectories from an ideal sinusoidal model.

Hence, the main point for us to prove in this chapter is whether the voltage-to-force conversion factor is valid for vesicles trapped inside a living cell, despite the intracellular environment. Since the actual particle position (in physical units) is not relevant for this purpose, one can potentially simplify the active-passive calibration process omitting the β -calibration part (which is one of the main contributors to the calibration errorbars in this method, as shown in Chapter 3). We did a first set of full measurements to understand the effect

of different parameters on the system calibration, and a second longer set of experiments focused only on the comparison of α in the two methods.

The hypothesis for the cross-validation of the two methods will consist on comparing the AP trap calibration (κ_{AP}^V , in pN/volts, defined in Equation 3.17) with the system calibration (α_{system} , defined in Equation 4.7), resulting in:

$$\kappa_{AP}^V = \alpha_{system} \frac{2k_B T}{\omega_S P(\omega_S)} \frac{A_P^V}{A_S} \sin(\Delta\phi) = \frac{R_D}{\Psi f' c} \quad (4.8)$$

4.3 Active-passive calibrations in A549 cells

4.3.1 Cell sample preparation

The A549 cell type (ATCC CCL-185) is a human lung carcinoma cell line initiated in 1972 by D.J. Giard using explanted lung tumour tissue from a 58 year-old white Caucasian male. The cells are adherent and look considerably flat when they are on normal growing conditions. Typical cell sizes are in the order of a few tenths of microns.. The choice of this cell type for the two-method cross-validation in living cells is in preparation for the intracellular force measurements we present in next chapter.

A549 cells were cultured following the standard protocol⁴. For the final sample preparation, a small amount of cells (typically ~ 1500 cells) were taken out during culture passage, placed on a sterile (autoclaved) glass coverslip and gently covered with growth medium filling the whole surface of the glass. The coverslip was stored inside a Petri dish, and after letting the cells settle on the glass surface for a few hours in the incubator (37°C, 5% CO₂), further growth media (3mL) was added to sustain cell growth. Trapping experiments were carried out 1 to 3 days after passage. As opposed to the yeast cells in the previous chapter, the A549 cells adhered firmly to the glass surface with no need of using poly-L-lisine. Just before the experiments, a micro-chamber was built by joining a clean glass coverslip, a silicone gasket ($\sim 100\mu m$ thick), and the cell-coated coverslip with the cells facing inside. The chamber was filled with an excess of growth medium, to avoid the formation of bubbles when closing the chamber with the upper coverslip. The sealing provided by the silicone gasket was enough to keep the liquid in the microchamber for the whole length of the experiments (typically lasting 1-2 hours).

Samples were placed on the microscope with the cells at the top side (i.e. cells hanging upside down from the upper coverslip). The adhesion force between the cell and the glass was enough to keep the cells attached during the course of the experiments with no apparent effect from the small gravitational pull. The reason for positioning the cells in the upper part of the chamber, as opposed to having them at the bottom (closer to the objective) is to maximize the amount of light collected by the condenser lens for force measurements. The long WD

⁴A549 cell line information: <https://www.lgcstandards-atcc.org/Products/All/CCL-185.aspx>

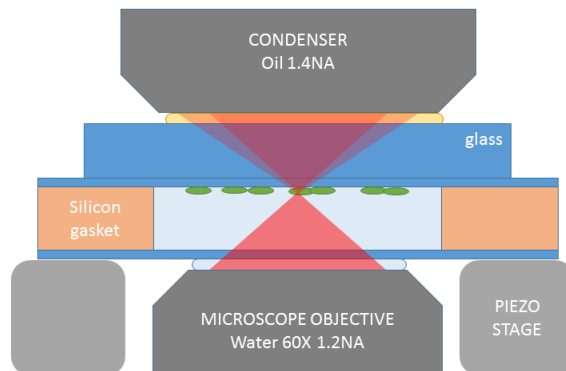


Figure 4.5: Illustration of sample design for force measurements, with trapping experiments at the top side of a liquid-filled micro-chamber.

of the water immersion objective allowed us to focus deep in the sample (near the top coverslip) to perform intracellular trapping experiments.

4.3.2 Intracellular trapping of Lipid Droplets

Trapping of cellular organelles inside the cells was achieved similarly to previous studies with other cell types in the group (e.g. NG108, *Nicotiana Benthamiana*, and *Allium cepa*) [23, 24, 81], where it was possible to optically trap organelles inside the cytoplasm (through the cellular membrane), with no significant damage to the cells [82]. A549 cells contain a variety of membranous structures within the cell cytoplasm that were visible under low NA bright-field illumination. Lipid Droplets (LD) have been used on previous studies as intracellular handles for micromanipulation experiments in *Drosophila* embryos [22, 83] and in A549 cells [36, 78]. Highly refractive spherical organelles in the cell cytoplasm, that were clearly contrasted in the microscope images, were identified as LDs for similarity with previous optical trapping studies in the same cell line. LDs are small organelles, with sizes ranging from 300nm to 1 μ m [36], typically with an average diameter of 700nm with 150nm standard deviation [83]. They have a high refractive index with typical values in the range of 1.48-1.53, while the cytoplasm refractive index is usually in the range of 1.37-1.40 [22]. Despite their small size, the high relative refractive index makes LDs suitable for intracellular optical trapping experiments with a range of forces that is relevant e.g. for molecular motor studies [83], as we will show in next chapter.

Any LDs within the microscope field of view could be targeted with the holographic trap. In order to check whether one particular object was trapped, a possible method is dragging the optical trap around the original position (with the holographic control interface) and observing whether the LD of interest follows the cursor trajectory across the cell or remains in its original position. Another less invasive method to ensure an object is actually trapped without

taking it far from its original location is by placing the trap in the close vicinity of the target object, and wait for it to freely “jump” into the trap as pulled by the optical force. Moreover, the system was aligned such that LDs on the trapping plane looked like dark spots, whereas they could look as white spots at other planes slightly off-focus.

For a given optical force (related to the trapping power, the organelle size and refractive index), the ability to optically trap and move an object within the cell cytoplasm strongly depends on its local environment. Some of the LDs were apparently strongly confined in stiff regions of the cytoplasm (e.g. densely packed with cytoskeletal filaments, or tightly bound to larger cellular structures) giving no chance for the available optical force to affect the object’s position. On the other hand, some LDs were located in more fluid regions of the cytoplasm, with no strong anchor points, and eventually diffusing in a Brownian fashion. In this context a targeted LD was more likely to follow the laser spot trajectory once trapped.

For the purpose of active-passive calibrations, the trapped object needs to be free to move to some extent in order to be able to evaluate position fluctuations in response to active driving. Hence, we restricted our LD measurements to those cases in which the balance between optical force and medium stiffness was favourable enough so that the LD could be successfully trapped and dragged by small sinusoidal perturbations. Live signal inspection during active-passive calibrations allowed us to check whether the object was totally stuck in the substrate or actively influenced by the trap force. When the medium rigidity is completely overcoming the optical force, the LD would move synchronized with the stage like a solid block, with no delay between the piezo and PSD signals. However, if the LD is optically trapped and free to move to some extent, the PSD sinusoidal signals will be shifted in time with respect to the stage driving, with a phase delay that depends on trap characteristics and local viscoelasticity. Only in this second situation will the active-passive method calibration succeed in measuring the system parameters.

4.3.3 Active-passive calibration in trapped LDs

A first set of active-passive calibrations were carried out on 26 different optically trapped LDs distributed over 12 different A549 cells, exploring a range of driving frequencies from 4Hz to 70Hz in 6Hz steps, in two perpendicular calibration directions (following the PSD axis), with laser powers ranging from 120 to 300mW at the sample. An amplitude of 200nm provided reasonable driving on most of the trapped particles, with sinusoidal trajectories clearly visible above the noise level, while keeping the object within the linear region of the trap (non-deformed ellipses). In those experiments in which the amplitude was observed to be too high (deformed ellipses), the driving amplitude was reduced to 150nm or 100nm.

The AP calibration provides a value for the voltage-to-force conversion factor (α) in pN/V for each trapped object. Similarly to the previous chapter, the resulting calibration values are averaged over different frequencies, following

	$\alpha_{AP}(pN/V)$	$\beta_{AP}(\mu m/V)$	$\kappa_{AP}(pN/\mu m)$	$c \kappa_{AP}/P (\mu m^{-1})$
μ	416	5.22	150	0.212
σ	73.6	4.92	149	0.215
σ/μ	18%	94%	99%	101%
$\overline{\varepsilon_{rel}}$	40%	13%	43%	43%

Table 4.3: Statistics of α (voltage-to-force), β (voltage-to-position), κ (trap stiffness), and $c\kappa_{AP}/P$ (normalized trap stiffness) measured for different LDs and powers: mean (μ), standard deviation (σ), coefficient of variation (σ/μ), and average relative confidence bounds ($\overline{\varepsilon_{rel}}$).

visual checks on the data. The PSD position calibration (β) was measured in every case as described in Chapter 3, and the trap stiffness calculated as the quotient of these two quantities: $\kappa = \alpha/\beta$. Those measurements that were clearly different from the general trend were excluded from the calculation of the average trap parameters. Measurements at 4Hz and/or 10Hz were most of the times far below the measurements at other frequencies, possibly due to cellular activity and noise at lower frequencies [71]. Some specific measurements at other frequencies were invalidated if strong drifts or jumps in the signal were observed, with help of video analysis to detect e.g. spurious objects coming into the trap (approaching the trapped object as seen in video images, and eventually falling into the trap). Another cause of drifts (invisible to video bright-field imaging) could be conformation changes in the cell cytoskeleton.

4.3.4 Measured trap parameters (α , β , κ)

The summarized statistics for this subset of calibrations are shown in Table 4.3.

The coefficient of variation for the voltage-to-force conversion factor (α) across different LDs is 18%. This margin of variations is below the average experimental error bars of the measurements (typically around 40% relative uncertainty in α on this measurements, mostly due to strong variations across different driving frequencies). Nevertheless, variations in α are small compared to β and κ values, which span over several orders of magnitude (with coefficients of variation of 94% and 99% respectively), as seen in Figure 4.7. Note that the spread in trap stiffness is still remarkable even when we normalize the trap strength by the laser power for each experiment ($\kappa c/P$, where c is the speed of light and P is the power at the sample), illustrating how strongly dependent is the trap stiffness on each trapped object. Having a spread on the voltage-to-force conversion factor of 18% across different trapped objects and powers is still a reasonable uncertainty for optical trap force measurements, considering that this avoids re-calibrating for each trapped object.

Even though κ and β are known to be strongly dependent on the trapped object and its environment, we expect their product ($\alpha = \kappa\beta$) to be a constant for the DF system, as α is not dependent on the physical characteristics of the sample. A scatter plot of κ vs β^{-1} for different LDs is presented in Figure

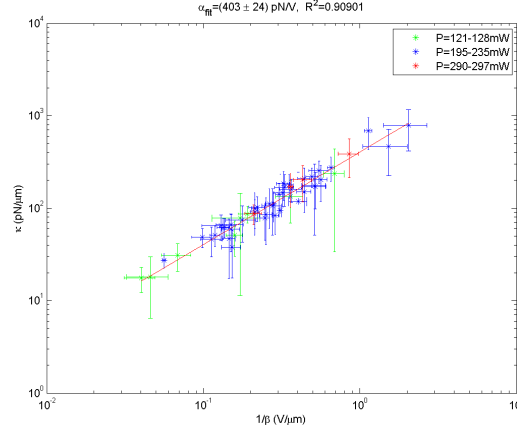


Figure 4.6: Trap stiffness (κ) vs position calibration coefficient ($1/\beta$) for different LDs and trapping powers, with a linear fit following the model $\kappa = \alpha/\beta$.

4.6, where we observe a reasonably linear trend between these two parameters. Interestingly, the graph also shows that inter-particle differences produce strong variations in κ and β , comparable even to the effect of changing the trap power up to a factor of $\times 2.5$. Using a $\kappa = \alpha(1/\beta)$ linear model, the obtained slope is $\alpha_{fit} = (403 \pm 24)pN/V$. This is in accordance with the mean and standard deviation values of this data set ($\alpha_{AP} = (416 \pm 74)pN/V$), but shows a trend slightly below the expected nominal calibration of the system (see Table 4.2), which is $\alpha_{nominal} = (488 \pm 30)pN/V$. The observed $\sim 15\%$ difference may be due to the presence of low frequency noise in AP calibrations, and it will be further discussed later in this chapter.

4.3.5 Asymmetry in trap parameters

Trap parameters may be dependent on the direction, e.g. due to small optical aberrations, polarization effects, or the non-sphericity of the trapped objects. The scatter plots of α , β and κ in two perpendicular calibration directions are shown in Figure 4.7.

In order to quantify their asymmetry in two perpendicular calibration directions (X and Y axis of the PSD), we define:

$$\varepsilon_{\alpha} = \frac{\alpha_y - \alpha_x}{\alpha_y + \alpha_x}, \quad \varepsilon_{\beta} = \frac{\beta_y - \beta_x}{\beta_y + \beta_x}, \quad \varepsilon_{\kappa} = \frac{\kappa_y - \kappa_x}{\kappa_y + \kappa_x} \quad (4.9)$$

The measured asymmetries for each parameter (averaged over different LDs) and their standard deviation are shown in Table 4.4. If one looks at the absolute value of the asymmetries averaged over different LDs, the unsigned asymmetries ($\langle |\varepsilon| \rangle$) are quite important for β and κ (with average variations of of 27% and 30% respectively in the X and Y axis), while the average unsigned asymmetry

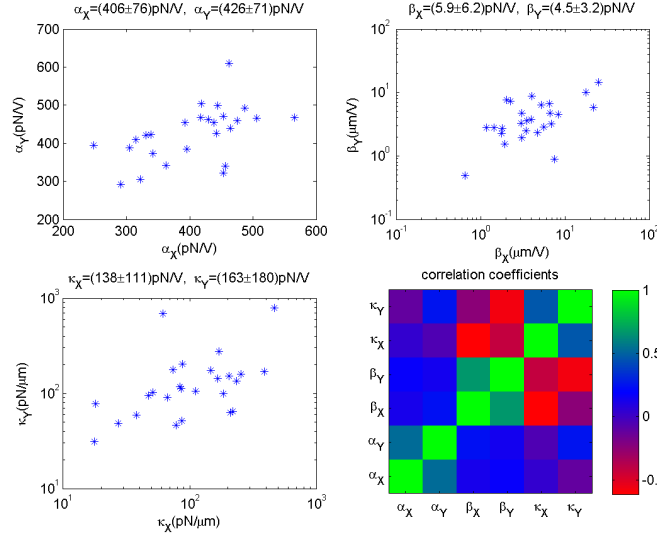


Figure 4.7: Scatter of trap parameter calibrations in two orthogonal directions (X and Y PSD axis).

	$\langle \varepsilon \rangle$	σ_ε	$\langle \varepsilon \rangle$	$\sigma_{ \varepsilon }$
α_{AP}	0.025	0.089	0.071	0.059
β_{AP}	-0.047	0.033	0.27	0.200
κ_{AP}	0.066	0.349	0.30	0.18

Table 4.4: Signed (ε) and absolute ($|\varepsilon|$) asymmetries of the calibrated trap parameters (α, β, κ), averaged over different LDs, and their standard deviations.

in α is much lower (7%). This is not surprising, since on an ideal force detection system we expect α to be a constant regardless of the direction across the BFP. Interestingly, if one looks at the signed asymmetries, their average values (grouping all LDs) are close to zero in all three cases. This indicates that the observed differences in the X and Y directions are mostly due to local sample anisotropies, rather than constant trap geometry or system aberrations, since the observed anisotropies seem to average out for all three parameters on a group of randomly-oriented objects. The cause of anisotropies could be either object shape and orientation, or beam aberrations induced by the cell membrane or other cellular structures in the surrounding area of the trap.

4.3.6 Dependence on particle size

A rough estimate of LD sizes can be obtained from the bright field images, although the measurement is not very accurate due to LDs sizes being close to the

microscope diffraction limit $d = \frac{1.22\lambda}{(NA_{objective} + NA_{condenser})}$ ⁵. Since we are totally under-filling the condenser lens (as mentioned before, to get enough image contrast for small objects in the cytoplasm) we rely only on the resolving power of the objective lens (1.2NA), providing a resolution for visible light around $\sim 0.55\mu\text{m}$. This is slightly below the typical LD size of 700nm, so measurements on the microscope images will provide us only with a rough estimation of trapped LDs size. We collected LDs sizes based on the radial distance between the particle centre and the first ring.

Another possibility used elsewhere for studying the dependency on object characteristics is looking at the normalised image contrast. This method was used in [36] as a way to extrapolate external trap stiffness calibrations into intracellular objects. If we define normalised image contrast as $q = (I_{max} - I_{min}) / \langle I \rangle$ on a $2.5\mu\text{m}$ square region around the trap position, we find a positive correlation (0.67) between the parameter q and the measured particle sizes (r).

If we look at a group of 40 calibrations at constant laser power, we observe that β increases with particle size, while κ decreases with particle size, as seen in the plots and the correlation values shown in Figure 4.8). However, α doesn't show a significant correlation with LD size, as we expected. Note that, for particles much smaller than the laser wavelength (Rayleigh regime) the trap stiffness would theoretically grow with the radius, while for particles much larger than the wavelength (Mie regime) the stiffness would decrease with particle size. In the intermediate range of sizes (comparable to wavelength, which is the case of LDs) there is no simple relationship to describe the dependence of trap stiffness with particle size. The slight positive correlation between LD size and PSD SUM channel may be due to the fact that smaller particles may have a more isotropic scattering profile (as opposed to larger particles, with a more forward-directed scattering), which may explain the changes in the amount of light collected in the forward direction as a function of particle size.

4.3.7 Measured PSD signal offsets

Another variable to take into account for force measurements, following Equation 4.6, is the PSD signal offsets (S_x^{ini}, S_y^{ini}). These signals account for the initial transverse momentum of the beam, when the trapped object is at the equilibrium position of the trap, with no net force acting on it.

As opposed to α , which stays mostly constant for the different trapped objects, the signal offsets do depend significantly on each trapped object, specially when dealing with heterogeneous samples. The signal offset may vary depending on variables such as laser power, the position of the trap within the microscope field of view, local beam aberrations (e.g. due to other sample structures).

Hence, it is necessary to determine this initial momentum in practice. Note that this is also a necessary step in all trap-stiffness approaches, where the trap centre has to be known (typically defined as the centre of passive fluctuations)

⁵<http://www.microscopyu.com/microscopy-basics/resolution>

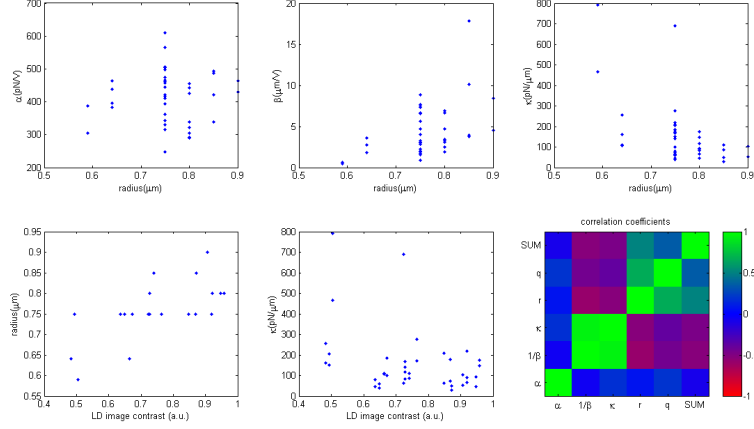


Figure 4.8: Dependence of measured trap parameters on LD size (r) and normalized image contrast (q) for a experiments at power $P_{sample} = 225mW$. Correlations between different parameters are displayed in lower right plot in a colour scale.

in order to be able to measure displacements and forces using Hooke's law. Similarly, we can measure the initial beam momentum by recording the PSD signals when the trapped object is at the equilibrium position of the trap, with no net force acting on it.

The distribution of PSD signal offsets for different calibration experiments in LDs, and different powers is shown in Figure 4.9. The standard deviation in the X and Y channels is 0.051V and 0.047V respectively, which corresponds to absolute force variations in the order of 25pN and 23pN. This is much higher than many of the biological forces that one could be interested in measuring (e.g. molecular motor force measurements within 1-15pN range), so the individual local offsets need to be subtracted in each measurement to convert signal to force, following Equation 4.6.

4.4 Validation of DF method in A549 cells

In order to explore further the frequency dependence of the active-passive calibrations, and cross-check the validity of both methods across different cell samples, we performed further calibration experiments ($n=150$) looking exclusively at the the force conversion factor α_{AP} on different LDs. The range of frequencies was kept from 4 to 70Hz.

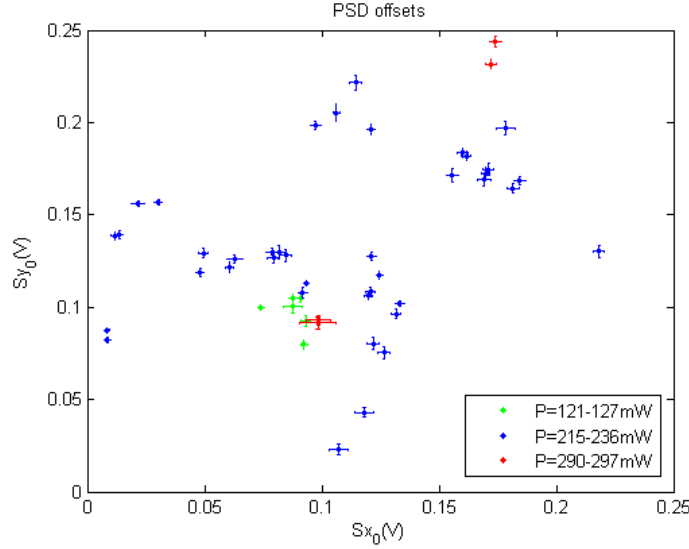


Figure 4.9: PSD signal offsets for different calibration experiments

4.4.1 Low frequency noise in A549 cells

Interestingly, what we initially thought as outliers (4Hz, or eventually 10Hz) in A549 cells active-passive calibrations seems to follow global trend over all studied samples. Since α is theoretically sample independent, we can average all the α_{AP} measurements for each active-driving frequency. The obtained values form a growing curve as a function of the frequency, $\alpha_{AP}(\omega)$, which tends towards a plateau at higher frequencies, as shown in Figure 4.10.

As we explained in the previous chapter, the calibrated stiffness should be independent of the driving frequency (specially for low driving frequencies, since the inertial term vanishes). However, it is known that biological activity in living cells may produce non-equilibrium fluctuations at lower frequencies, which may explain the observed pattern [84, 85]. In support of that, when observing the A549 cells on the microscope, there are LDs undergoing clear directional movements, i.e. performing runs of several microns in one specific direction for a few seconds. This is known to be caused by direct action of kinesin and dynein molecular motors, which transport LDs within A549 cells along microtubules, as we explore further in the next chapter.

For comparison, directed motion events were not visually observed in the *S. Pombe* cells studied in the previous chapter, where lipid granule trajectories were rather floating in a diffusive fashion, apparently confined around certain areas. Dedicated diffusion studies in fission yeast [77], using optical tweezers and multiple particle tracking, show that the motion of lipid granules in this type of cells is subdiffusive, presumably due the presence of dense polymer networks and cell membranous structures in the cytoplasm. Here they indicate that the

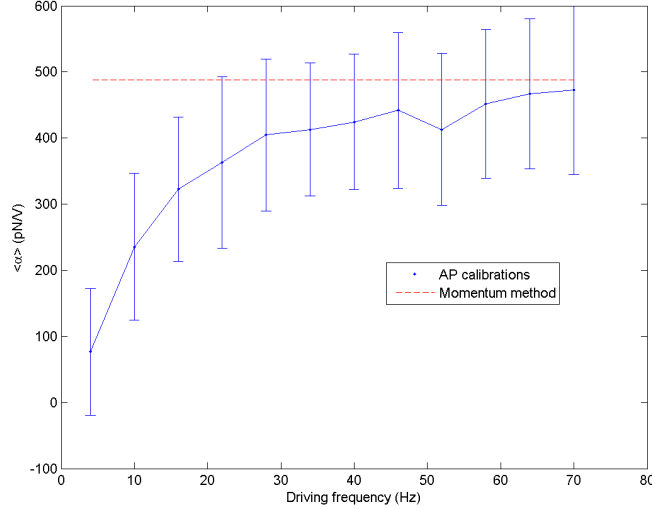


Figure 4.10: Frequency dependence of α_{AP} calibrations (averaged over 150 different calibrations), with errorbars corresponding to the standard deviation. The nominal system calibration α_{system} is shown as a reference.

viscoelastic landscape of the fission yeast cells may be more consistent with the physical properties of in vitro actin networks, and quite different from that of higher eukaryotic cells. That would explain the differences observed between the yeast and A549 experiments regarding the noise at lower frequencies.

In practice, biological activity in A549 cells increases the value of passive spectra at lower frequencies, compared to the spectra in equilibrium conditions. Following Equation 4.8, an overestimation of the equilibrium passive spectra $P(\omega_S)$ results in an underestimation of trap stiffness, which is consistent with our results. We could not explore the plateau at higher frequencies due to the limited bandwidth of the piezoelectric stage. However, within the explored frequency range the measured $\alpha_{AP}(\omega)$ tends towards a stable value at the highest frequency (70Hz), close to the nominal α_{system} .

4.4.2 AP calibrations at higher frequencies

We calculated the resulting α_{AP} for each of the 150 active-passive calibrations considering two cases: the usual approach, in which all frequencies are taken into account (except for 4Hz and 10Hz measurements, that are outliers in most of the measurements), and a second case in which only the highest frequencies (64-70Hz) are considered. The statistics for 150 active-passive calibrations, for the two mentioned frequency ranges, are summarized in Table 4.5.

For the first case we get an average α_{AP} and spread values very similar to

	$\alpha_{AP}(pN/V)$ (16-70Hz)	$\alpha_{AP}(pN/V)$ (64-70Hz)
μ	417	470
σ	76	113
σ/μ	18%	24%
$\overline{\varepsilon_{rel}}$	36%	33%
p (T-test)	6.8E-22	0.053
Compatibility with α_{system}	×	✓

Table 4.5: Statistical parameters (mean (μ), standard deviation (σ), coefficient of variation (σ/μ), and average relative confidence bounds ($\overline{\varepsilon_{rel}}$), corresponding to active passive calibration results considering either all frequencies from 16 to 70Hz (similarly to Table 4.3), or considering only higher frequencies (64-70Hz). We also show Student’s T-Test results to the hypothesis of the measured data having average α_{system} , with 5% significance level.

what we got on the initial measurements (from Table4.3), with a significant difference (14.5%) from the reference value $\alpha_{system} = 488pN/V$. If we use a Student’s T-Test to check the compatibility of both methods, it rejects null hypothesis of the all-frequency AP dataset having a mean equal to α_{system} with 5% significance. Hence, the two measure quantities and the reference value are significantly different.

However, if we consider only the two highest frequencies for each calibration (64-70Hz), which are less likely to be affected by molecular motor activity, the average value is much closer to α_{system} (only 3.6% difference), and the hypothesis of the population having a mean equal to α_{system} cannot be rejected with 5% significance. The resulting α_{AP} values at the high frequency range for all experiments are shown in Figure 4.11.

4.4.3 Evidence of biological activity

When passively trapping a LD with no active driving from the stage, sometimes force fluctuations are observed on the PSD signals. This illustrates the idea of the cell cytoplasm being a very dynamic environment, with many different organelles involved, including the trapped objects.

One of possible source of forces is the action of molecular motors in the cell, that bind to LDs and carry them along cytoskeletal filaments. When a motor starts pulling from an optically-trapped LD, typically a stall event is produced, in which the force signal grows up to a saturation level (motor stall) and then suddenly jumps down to the original value (when the motor stops pulling and dissociates from the cytoskeletal filament). This type of event is extensively explored later in next chapter, but some examples can be observed here e.g. in the initial part of the time series presented in Figure 4.12, around $t=20s$, and $t=30s$. These curves illustrate a form of biological forces that one could potentially study and quantify inside living cells using the momentum method, or using an AP-calibrated optical trap stiffness.

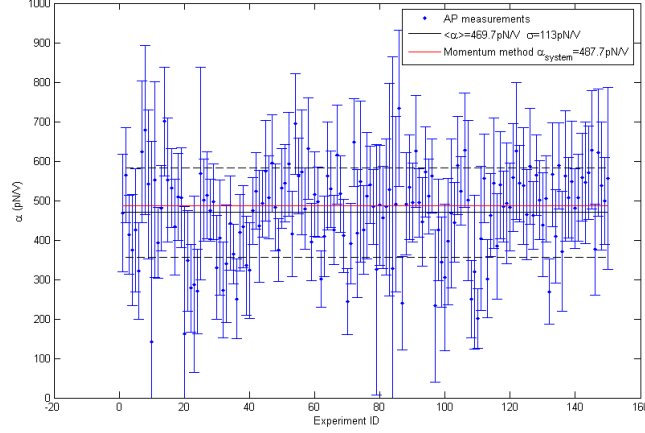


Figure 4.11: Calibration results in the 64-70Hz frequency range for 150 different active-passive calibration experiments, with mean and standard deviation limits, as well as α_{system} reference value (red line).

Another possible source of fluctuations on the PSD signals is the presence of other moving structures in the cell, that may be interfering with the beam and/or directly with the trapped LD if too close. This type of effect is observed towards the second half of the time series shown in 4.12. In the video frames the trapped LD (central black object) is labelled with a yellow arrow, and several other LDs are visible around it. Two of them (marked with red arrows) are at $t=25\text{s}$ at $\sim 2\mu\text{m}$ lateral distance away from the trap, at a slightly different focus (the white aspect typically corresponding to objects sitting above the trapped object). As time progresses the spurious objects get closer to the trapped object ($\sim 1\mu\text{m}$ from the trap centre at $t=40\text{s}$), and eventually fall into the trap area ($t=50\text{s}$ and $t=62\text{s}$). The corresponding PSD signals (specially the S_Y channel) show quite a stable baseline for the first part of the measurement, except for the temporary stall force events mentioned above. From $t=45\text{s}$ longer drift starts, corresponding to the fraction of time in which the spurious LD gets into the trap area.

Note that the magnitude of the drifts caused by other particles is comparable to the magnitude of force changes in some of the initial stall events. Hence, it is important to monitor the trap surroundings during any force measurements, to be aware of other potential objects falling into the trap area.

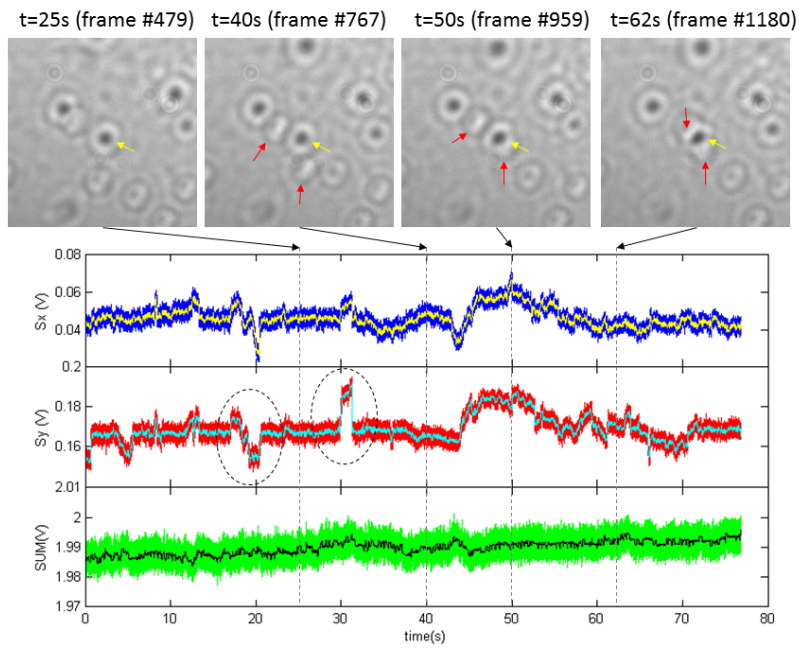


Figure 4.12: Sequence of a trapped LD (yellow arrow) with spurious LDs (red arrows) getting into the trap. The PSD signals of a 77s-long measurement are shown, with indications of 4 different positions as the spurious objects come closer to the trap. Circles show activity of molecular motors, which is further explored in next chapter.

4.5 Comments on two-method cross-validation in A549

Active-passive calibrations tending to a plateau around 70Hz indicates that the AP measurements may be getting closer to the actual trap parameters towards higher frequencies. We could not explore this plateau further at higher frequencies because of the limited bandwidth of the piezo-electric stage, and the presence of spurious peaks around 100Hz due to mechanical resonances of the system.

Looking at the available data, it is reasonable to assume that the measurements at the highest frequencies are the closest estimation we can get to the real calibration parameter with the current system. Further improvements, e.g. using an acousto-optic deflector (AOD) for active-passive calibration, would allow us to explore the two-method compatibility at higher frequency ranges, far away from the time-scales of cellular active processes. For example, an AOD at 4000Hz is used in [78] for active-passive calibration with laser-driving approach. Moreover, using laser-driving for AP calibrations (rather than stage-driving), the position parameter β could be quickly determined.

Active-passive calibration and momentum-based measurements are based on completely different assumptions: the former assumes the trap force being linear with the trapped object position, and the medium behaving as a viscoelastic material, while the latter assumes that there are no major biases due to optical momentum changes across different cellular structures (other than the trapped bead). The fact that the system calibration based on optical momentum matches the active-passive calibrations (at those frequencies with highest reliability) for different LDs, cells, and samples, leads us to conclude that structural light losses in A549 cells are not a major concern for doing optical force measurements in such environment. Still, care must be taken in locally determining the offset signals for each experiment, and keeping an eye on moving organelles in the vicinity of the optical trap to avoid them interfering with the force measurements.

If we compare the active-passive calibration results from this and the previous chapter, a clear reduction in the coefficient of variation (σ/μ) of the voltage-to-force conversion factors is observed: there is a spread of 51% variation in κ^V for *S. Pombe* measurements at constant laser power (with BFPI system using a QPD), while for the measurements in A549 cells (BFPI system with a PSD and optimized light collection) the spread reduces to 24% variation in α_{AP} (including measurements at different laser powers). Even though these two studies were performed in different types of cells, the results are an indication of the advantages that come from optimizing a BFPI system for momentum-based measurements.

Chapter 5

Molecular motor *in vivo* force measurements through light momentum changes

In this chapter a short introduction on the molecular motor role in intracellular transport is given, previous force studies (both *in vitro* and *in vivo*) are summarized, and finally new measurements of molecular motor stall forces in living cells via the light momentum method are presented and discussed.

5.1 Molecular motors and intracellular transport

Molecular motors are protein machines that have the ability to convert chemical energy from ATP hydrolysis into mechanical work (e.g. displacement or rotation against an opposing force or torque). Eukaryotic cells contain molecular motors that help transporting organelles to their correct cellular locations and modifying cellular morphology during cell locomotion and division [86]. Several diseases are known to be associated with abnormal motor operation [87]. Different families and subfamilies of motors exist on different living species [88]. The main agents for organelle intracellular transport are three motor groups: kinesin, dynein and myosin. These motors bind to the cell cytoskeletal filaments and typically advance in a 'hand-over-hand' manner in steps along the filaments. High directionality (ability to move unidirectionally along a cytoskeletal filament) and processivity (ability to bind to a filament and take successive steps before detaching) are characteristic features of cytoskeletal motors [89]. In particular, kinesin and dynein motors bind to cell microtubules and tend to progress towards the plus or minus ends respectively i.e. moving away-from (outwards) or towards (inwards) the Microtubule Organizing Centre (MTOC), which is located next to the cell nucleus. Microtubule motors play a role e.g. on bidirectional transport in neurons [22] and cell division [90]. On the other

hand, myosin motors are associated with actin filaments and they play a role e.g. on skeletal muscle contraction [91], or organelle transport in some cases [92, 93]. There are structural differences between each motor kind, and also differences on their performance in terms of duty ratio (fraction of time a motor head spends attached to the associated filament during a complete duty cycle), procession speed, step size, travel length and stall force. Moreover, different subgroups of motors within each family lead to selective organelle transport for each particular cell function [94].

5.1.1 Motor studies on *in vitro* optical trapping assays

Biophysical properties of molecular motors have been accurately characterized experimentally on *in vitro* optical trapping assays, starting from Ref. [15]. Kinesin is known to be a highly processive motor which is able to take hundreds of 8nm steps on a run (matching the actual distance between tubulin adjacent hetero-dimers [95]) with a load up to 6pN [96], typically stalling at 5pN [97]. On the other hand dynein-dynactin complex is also processive but with some peculiarities [98]. The stall force of dynein is a controversial topic. According to some sources it would normally make displacements of 32nm or 24nm steps under no load while the steps would reduce to 8nm under a maximum load force of 1.1pN [99]. Other studies report 7-8pN with 16nm steps (with occasional forward/backward 8nm steps) [100], and measurements on yeast cytoplasmic dynein show a stall force of 7pN [101]. A very recent *in vitro* study on mammalian dynein, including dynactin and Bicaudal-D2, reports a stall force of 4.3pN. It is important to note that dynein might behave differently for different organisms [102]. Besides, myosin motors are associated with actin-mediated transport, their step size is 35nm (following the half pitch of the actin filament helix) and they can hold an elemental force of 0.5pN per motor in higher plant cells (Myosin XI) [92]), or up to 5-6pN in myosin purified from rabbit muscle [103].

5.1.2 The complexity of motor activity *in vivo*

The actual performance of molecular motors on their natural environment, *in vivo*¹, is still a topic for ongoing research and it cannot be directly deduced from *in vitro* measurements [93]. Ultimately quantitative biophysical experiments need to be reproduced inside living cells to take into account all the environmental variables and ongoing processes involved in intracellular transport, like local stoichiometry, cytoplasm viscosity and molecular co-factors. One example is cytoplasmic dynein's performance which can be greatly affected by several regulatory factors [105] like dynactin and Lis1 [106, 107], apart from local ATP concentration and force load. That complexity could explain the controversial dynein stall-force measurements reported on different sources [108].

¹Note that in molecular motor literature the term *in vivo* is referring to the living cell itself, and not to a whole living organism as it is usually done in medical literature.

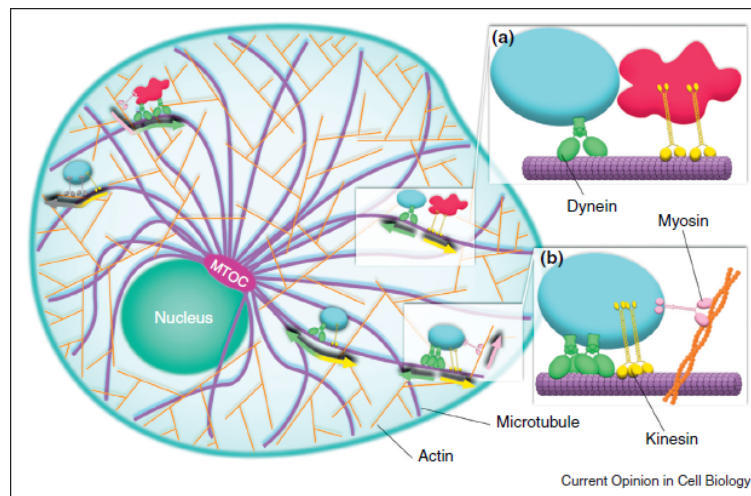


Figure 5.1: Image reproduced from Barlan *et al* [104] with permission from the publisher (Elsevier, license number 3958460529237). Different kinds of motors allow membrane organelles to be transported through the cytoplasm of eukaryotic cells. Kinesin (yellow) and dynein (green) are the main responsible for long distance transport along microtubules (purple) outwards or inwards respectively. Myosin motors (pink, gray) move along actin filaments (orange) and are usually responsible for short-range transport. Apart from being the substrate for molecular motors, cytoskeletal filaments also restrict vesicle motion along certain unidimensional spaces facilitating organelle interaction (inset a). Cargo transport is usually achieved by the combined action of a plurality of motors of equal or different types (inset b). The transport of each individual organelle is likely regulated by specific factors to allow rapid changes in distribution and motility [104].

Additionally to single-motor performance specifications, several motors can team-up *in vivo* to collaborate and regulate intracellular transport. For example kinesin velocity can increase with the number of motors pulling together against the cellular viscoelastic drag (which is about 1000 times higher than in a standard *in vitro* buffer) [109]. Also, some authors suggest that the stall force of kinesin-1 is additive [110, 38] and it can actually be used as a way to count the number of active molecular motors on a specific organelle. Interestingly other sources show that for a low number of kinesin-1 pulling together from the same organelle there is no much effect on the resulting force compared to the single kinesin case [111], presumably because the leading front motor (the one further along the track) would take over most of the effort required for particle displacement. The fact that kinesin stepping period cannot vary from 8nm, makes the lead motor unable to slow down and wait for the rear motors to catch up [104]. The number of active kinesin motors has been shown to be dependent on the local concentration of microtubule associated protein, tau [112]. Force sharing between multiple active kinesin motors does also have an effect on the final cargo travel length on long-distance transport [113], and low velocity conditions (by lower ATP) can benefit multiple kinesin collaboration [114].

On the other hand, the weaker cytoplasmic dynein seems much more prone to collaborate in order to generate larger forces, which is fundamental in cellular processes like long-range retrograde transport, cell migration, cytoskeletal reorganization, chromosome separation or nucleus migration [39]. Here dynein motors are shown to collaborate against an opposing force in a linear additive manner (twice the dynein number, twice the force). This is likely due to the fact that dynein can move in varying step sizes, which makes it easier for the motors in a group to wait or to catch up depending on what the rest of the team does, achieving an even distribution of the force load among the team.

There is also some controversy on the actual way kinesin and dynein coordinate their efforts in the cell cytoplasm, each of them pulling a priori towards opposite microtubule ends. Frequent direction changes are observed on cargo motion *in vivo* [115]. One hypothesis is that there is a switch that turns on and off each specific family of motors [116] making the cargo move coordinately towards either one end or the other. Another popular explanation is a tug-of-war model where opposing groups of motors are pulling from the cargo at the same time in a stable force balance, and the net cargo movement is regulated by small variations in active motor numbers at either side, which would effectively make the cargo move in 8nm steps towards a specific direction [70]. Even though there is some experimental evidence for that model both *in vitro* [117] and *in vivo* [118], simple stochastic mechanical tug-of-war cannot explain bidirectional transport *in vivo*, which is likely to require also other regulatory mechanisms [119].

An important parameter to understand how the motors combine their efforts to achieve successful organelle traffic is the stall force i.e. the maximum force a motor can hold before stopping and detaching from the filament. Table 5.1 summarizes some of the previous studies measuring molecular motor forces *in vivo*. The observed values are quite varied, which could be due to both the

variety of force calibration methods and the variety of cell types/organelles. The first measurement for the dynein stall force *in vivo* in [14] gave about 2.6pN in *Reticulomixa* mitochondria, with a 2-3 uncertainty factor due to trap stiffness uncertainty. Another study in *Drosophila* embryo shows lipid droplet stalling at multiples of 1.1pN [22], although this was later attributed to incomplete stall events (detaching before stall) in [38]. Both kinesin and dynein have been shown to have stall force probability peaks at ~ 2.5 pN in *Drosophila* embryo lipid droplets [38, 37], with some events at higher forces that could be associated to the action of a plurality of motors. Other studies show differential features in the inward/outward probability distribution of measured stall forces e.g. studies in macrophage phagosomes [70, 39], or A549 cells [36, 78], as shown in Table 5.1. The stall force probability is shown to be different for opposing motor types, but also vary for the same motor type across the literature, which makes it difficult to extract a general conclusion on the actual stall force of each motor.

An example indicating the relevance of stall force measurements for a better understanding of transport mechanisms is shown in [78], where they use the AP method (in its laser-driving form) for calibrating the optical trap *in situ*. Their *in vivo* inward stall force measurements are compatible with multiple dynein motors pulling from the cargo (assuming ~ 1 pN stall force per dynein), while outward stall forces are lower than expected for kinesin (typically 5-7pN on *in vitro* measurements). Complementary *in vitro* experiments indicate that, while dynein is possibly the main responsible for minus-end microtubule transport, it can also play a role in plus-end transport when a higher load force is applied on the latter direction (e.g. by a kinesin motor). Note that interestingly this requires dynein to move eventually towards the plus end following the kinesin advancement, a bidirectional behaviour that has been also observed for that motor in other studies [101]. In that case the kinesin pulling force on an outward stall force experiment would be balanced not only by the optical trap but also by bound dynein motors. This would likely make the measured optical force lower than the actual kinesin stall force, and that would explain the measured lower stall forces.

5.2 The stall force experiment

A typical stall force measurement on a cytoskeletal motor involves the application of a known opposing force on the motor while it is active. The motor velocity would typically decrease when the opposing force increases, and will become static when the opposing force matches its stall force limit. The motor can stay in a stalling situation for some time (typically for hundreds of ms) without advancing/receding until it eventually dissociates from the cytoskeletal track.

Despite the very small size of molecular motors, optical tweezers can be used to apply varying external force loads onto them, up to tenths of piconewtons, by using the motor cargo itself as a handle (e.g. a lipid droplet [83] or phagocytosed latex microbeads [70]). When a motor is bound to a microtubule and its

Cell type (force handle)	Trap stiffness calibration	Stall forces
[Ashkin1990] <i>Reyculomixa</i> (mitochondria)	<i>Ex situ</i> calibration with viscous drag forces. Extrapolation to the cell using correction factors accounting for internal amoeba viscosity and refractive index. Uncertainty factor of 2-3 from that estimations together with particle size variability.	Dynein motors: 2.6pN (per motor)
[Welte1998] <i>Drosophila</i> embryos (lipid droplets)	<i>Ex situ</i> with viscous drag forces and Brownian motion analysis. Isolated lipid droplets of known sizes are trapped in a sucrose buffer matching cytoplasm refractive index. Extrapolation into cells using an experimental relation between organelle size and stiffness (apparent size correction according to calibration with silica beads)	Organelle stall at multiples of 1.1pN (possible single-motor elementary force, or net force from a complex of different active motors)
[Shubeita2008] <i>Drosophila</i> embryos (lipid droplets)	<i>Ex situ</i> . Refractive index of droplets and cytosol is measured. External calibrations with polystyrene beads of various sizes in a fluid matching the droplet-to-cytosol index ratio.	<u>Outward</u> : average of 4.0 ± 0.5 pN, with peaks at 2.6 pN and 5.2 pN. <u>Inward</u> : average of 3.9 ± 0.2 pN, with peak at 2.4 pN.
[Sims2009] A549 human lung cells (lipid droplets)	<i>Ex situ</i> calibration with Brownian motion analysis in sucrose solution (matching cytoplasm's refractive index). An empirical correlation between trap stiffness and droplet bright field image contrast is used to extrapolate the trap stiffness inside the cell.	<u>Outward</u> : average of ~ 8 pN, with peaks at 3 pN and 6 pN <u>Inward</u> : average of ~ 7 pN, with peaks at 4 pN and 9 pN
[Leidel2012] <i>Drosophila</i> embryos (lipid droplets)	<i>Ex situ</i> calibration with Brownian motion analysis in buffer. A monotone function between stiffness and droplet size (DIC measurements) is used for extrapolating the stiffness in the cell. Apparent size corrected with a calibration curve (from polystyrene beads). 25% Uncertainty.	<u>Outward</u> : peaks at 2.6 pN, 5.3 pN and 8.5 pN Similar elemental stall forces for both kinesin and dynein: ~ 2.5 pN
[Rai2013] J774.2 mouse macrophage cells (phagosomes with latex beads)	<i>Ex situ</i> trap stiffness calibration (Brownian motion analysis) using latex beads of equal characteristics trapped in a sucrose solution with $n=1.367$ (cytosol refractive index). The stiffness is directly extrapolated to internalized beads (same type) for force measurements.	<u>Outward</u> : peaks at 5.8 pN and 10.5 pN. Kinesin works frequently alone. <u>Inward</u> : peaks at 4.3 pN, 6.0 pN, 7.7 pN, 9.7 pN and 12.1 pN. Dynein likely to work collaboratively.
[Hendricks2012] J774A.1 mouse macrophage cells (phagosomes with latex beads)	<i>In situ</i> trap stiffness calibration using TF method. The response of the trapped particle to controlled laser driving allows the local determination of trap stiffness.	(Events > 250 ms) Similar Inward/Outward forces, most in 1-2 pN range. (Events > 1 s): <u>Outward</u> : 1.2 pN, and broader peaks at 3.5 pN, 6.3 pN, 13.2 pN. <u>Inward</u> : 1.6 pN, 2.3 pN, 5.7 pN, 8.0 pN, 11.1 pN (consistent with "elementary" ~ 1.7 pN force)
[Blehm2013] A549 (lipid droplets) & <i>Dictyostelium discoideum</i> (phagosomes)	<i>In situ</i> on-the-fly trap stiffness calibration with FDT method for viscoelastic environments.	Similar forces for both cell types. <u>Outward</u> : broad peak at 2-7 pN (lower than <i>in vitro</i> measurements of 6.8 pN for purified kinesin) <u>Inward</u> : peak within 2-3 pN (more than 1.1 pN <i>in vitro</i> measurements for dynein)
[Yun&Gross2014] HEK293 cells	Comparison of different methods (including momentum-change)	Kinesin. Histogram peaks at 4.6 pN and 9.2 pN

Table 5.1: Examples of *in vivo* kinesin/dynein stall force studies with optical tweezers. A variety of force calibration methods have been used, either *ex situ* or *in situ*. and stall forces distributions for kinesin and dynein vary depending on the experiment and the studied biological system.

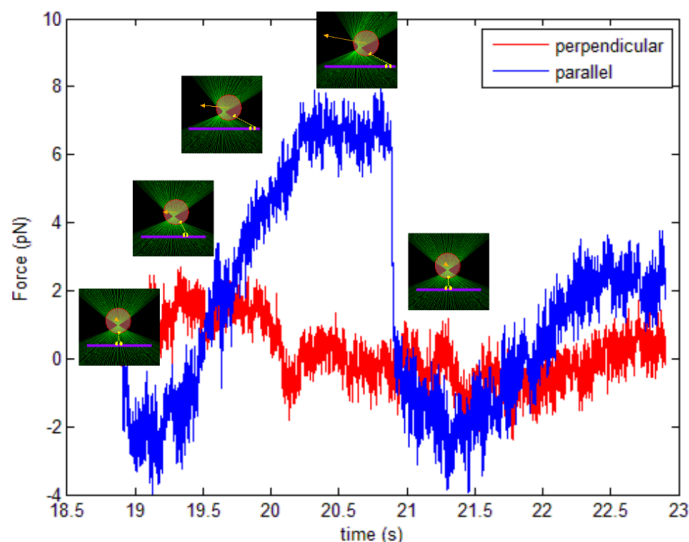


Figure 5.2: Stall force curve reporting motor tension force as the motor advances.

cargo is trapped by the focused light beam, a tension force will immediately be produced on the motor molecule, with a magnitude and direction that depends on the relative position between the cargo position and the trap centre. The optical trap (with an appropriate force detection system) can then be used as a dynamometer to measure the force acting on the cargo.

The stall of a motor can be achieved by keeping the trap at a fixed position while the motor advances, thanks to the force of the optical trap increasing with the distance between the trapped object and the trap centre. The motor ideally perceives no initial tension when the trap is placed at the cargo position, and the tension increases as the motor actively moves away from the trap centre while pulling the cargo along the cytoskeletal track. The optical force becomes higher the further the motor goes (growing phase) until the stall force value is reached and the motor cannot advance any more. At that moment, the measured optical force equals the motor pulling force and there is neither advancement nor retreat for a short time while the forces are balanced (stall force plateau, typically lasting in the order of 100ms). At some point, the motor spontaneously detaches from the cytoskeletal track resulting in the optical force becoming the only relevant force acting on the organelle which, free to move, quickly jumps back to the trap's equilibrium position. Note that Brownian fluctuations within the trap might let the motor/s (still attached to the cargo) eventually bind again to a microtubule, which would allow for consecutive running-and-stalling events with the same organelle. A representative example of stall force curve with the different phases is shown in Figure 5.2.

An alternative approach is keeping the force load invariant using a force clamp system. This involves using a fast feedback loop for moving the trap/stage in real-time in such a way that the force value is kept constant (by keeping the relative trap-bead position unchanged following motor displacements). Force-clamp allows systematic investigation of the motor response (velocity, step size) as it travels under a controlled tunable external force, either pulling forwards, backwards [17] or even on lateral directions [120]. However, for our purpose (measuring the stall force *in vivo* with the light momentum method) it is more convenient to keep the trap still during a measurement, which avoids additional changes on the initial momentum of the beam (baseline) due to cell optical heterogeneity.

For a better understanding of intracellular transport mechanisms and, more specifically, for clarifying discrepancies on the actual dynein stall force, further and extensive *in vivo* force measurements would be required to explore the effects of cell type specificities and reduce uncertainties in data acquisition and analysis [108]. There has been a strong interest within the scientific community to push towards *in vivo* molecular motor force measurements during the last years, with special attention on the way the optical trap is calibrated in the cell [121, 69]. The ultimate goal is to understand the regulatory mechanisms which allow molecular motors to coordinate and effectively transport cargoes within cells [122].

In this chapter we apply the momentum method on the measurement of molecular motor stall forces, and we show that the method is able to determine molecular motor stall forces *in vivo* with the convenience of not having to recalibrate the trap for each specific organelle. This makes data acquisition easier and increases the amount of data that can be collected compared to other approaches, since a force signal is obtained from the very first moment a vesicle is trapped.

5.3 Stall force measurements in A549 cells

5.3.1 Intracellular traffic in A549 cells

A549 cell type, described in the previous chapter, was used in one of the few previous kinesin and dynein *in vivo* stall force studies [36]. Most of the organelle traffic within the cytoplasm takes place within a 2D-like space, particle defocusing is rarely observed during active transport. Directed organelle traffic within A549 cell cytoplasm was found to be more scarce than in other cell types (like *Albium cepa*), but still much more relevant than in *S. Pombe* cells (where directed traffic was not visually observed) Lipid Droplets (LDs) in A549 were normally diffusing on a Brownian fashion and, eventually, some of them described clear linear trajectories over a range of a few microns, typically lasting a few seconds. An example is shown in Figure 5.3, where particle tracking over 100s shows some particle trajectories. Most of them are confined to their original positions but some particles made excursions in a clearly linear fashion, eventually mov-

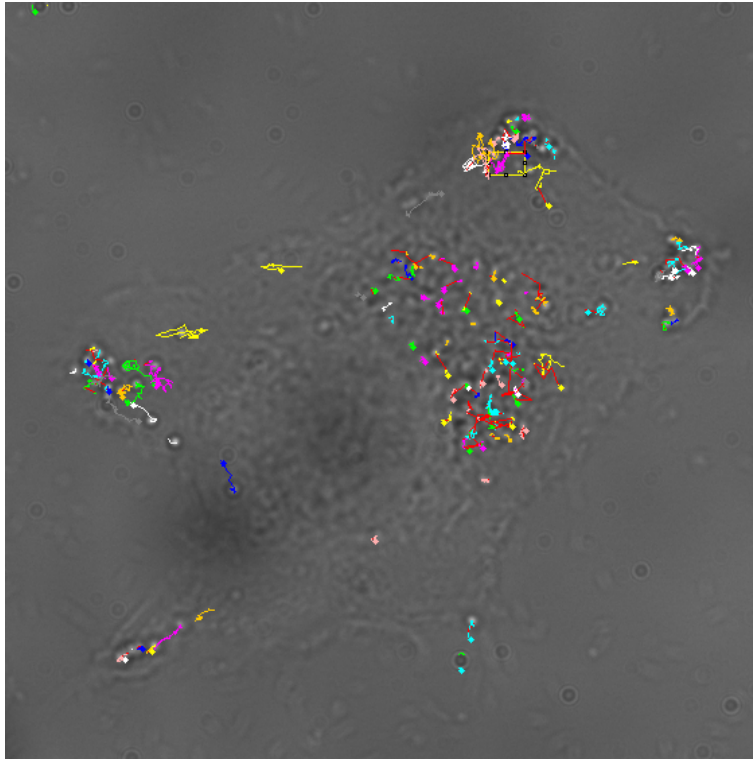


Figure 5.3: A549 cell image with organelle trajectories over a period of 100s (the full field of view is $58.1\mu\text{m}$ long in both dimensions). A few organelles describe unidirectional trajectories (black circles), either one way or in a back-and-forth fashion. Other organelles do not significantly move from their original location, or describe an erratic trajectory (note that red lines are not actual trajectories but lost-and-found issues of the tracking algorithm). Particle tracking was carried out using MOSAIC Suite for ImageJ.

ing back-and-forth over the same line. This quietness allows performing stall force measurements on a given organelle with few spurious organelles frequently jumping into the trap, and this is convenient for getting clear molecular motor data.

5.3.2 Comments on trapping power

The trap power plays an important role for successfully measuring molecular motor stall forces. At low powers some of the LDs could not be systematically trapped, or escaped the trap driven by biological forces. Using higher power increases the ability to trap organelles (since trap stiffness is directly proportional to power), but this has the drawback of reducing the natural extent of

the Brownian motion of the trapped particles. Brownian oscillations are key for letting the molecular motors on the trapped organelle eventually bind to a cytoskeletal track and become active. Typically the motor is unbound after the organelle is first trapped (and possibly pulled apart from its original position) or after a stall event (where the organelle has jumped to the trap centre following motor detachment). Small random excursions of the unbound bead within the trap can randomly create favourable geometrical conditions for the motor to rebind to a cytoskeletal track. Hence if the trap is too tight molecular motors on the bead might not be able to successfully bind again to the track, especially if the trap is not exactly positioned on top of a MT, and that leads to a decreased probability of recording molecular motor force data (rather the organelle is kept on the trap centre for a long time).

In our case laser powers in the range of 140-230mW (1064nm wavelength) at the sample² proved to be enough for reproducibly trapping the majority of LDs without any apparent photodamage to the cells, while allowing consecutive stall events with the same organelle. This amount of power is still below the threshold mentioned in [2], where organelle trapping with 1064nm light is not expected to cause relevant cell damage when trapping organelles with 340mW at the sample and holding them for a number of minutes. Laser-induced cell heating is not expected to play a significant role in our experiments. E.g. a temperature increase of (1.15 ± 0.25) °C/100mW has been reported in CHO cells using a 1064nm laser trap (1.3NA 100X objective) [123]. Since we use lower NA (1.2 60X WI objective) the energy density at the spot will be even lower than in the mentioned situation. We estimate a local temperature increase $<5^\circ\text{C}$ in our experiments so, considering the ambient lab temperature was in the range of 18°C - 25°C , it is very unlikely that we get local cell heating above 37°C .

5.3.3 Nocodazole assay

The directed events are presumably related to the action of molecular motors. In order to ensure this is related to microtubule motors (i.e. kinesin and dynein) we used Nocodazole, a drug that is known to disrupt the cell microtubule network by impeding tubulin polymerization. For that test cells in culture were first checked to be on a healthy state (flat and with active traffic) and then incubated in culture medium with 5mg/mL Nocodazole (Sigma M-1404) for 30min (at 37°C and 5% CO_2). After incubation, succeeding observations showed that directional vesicle traffic had completely ceased; only Brownian motion was observed on the cell organelles at that point after microtubule disruption. Next, cells were washed with PBS and re-incubated with fresh normal growth medium (30min, 37°C , 5% CO_2) to let the cells reconstruct their tubulin cytoskeleton. The following observations showed that directed transport activity in the cells was restored, proving that the previous traffic freezing was due to the actual

²Power at the sample was calculated on each experiment from the PSD signal (SUM channel) taking into account the pre-calibrated detector efficiency and the transmittance of additional filters that were included on the force detection system for working at higher powers.

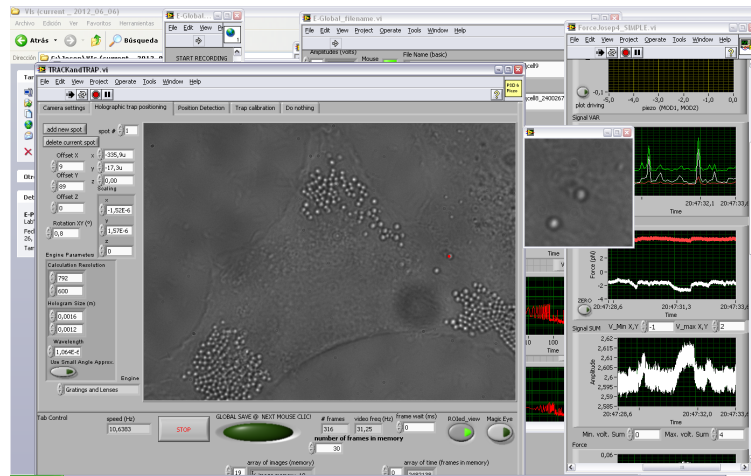


Figure 5.4: LabVIEW interface for recording of force and video signals from trapped objects

depolymerizing action of Nocodazole, rather than cell death. With that, we can associate the observed directed organelle traffic events to the microtubule network, and hence to the action of kinesin and dynein molecular motors.

5.3.4 Experiment protocol

Cell samples were prepared as described in Chapter 4. Prior to the experiments samples were inspected looking for active organelle traffic in the cells, which was used as an indicator of the cells being on a healthy state. As opposed to the experiments in the previous chapter, here only reasonably isolated cells with clear geometry were chosen (with their nucleus and cell contour unambiguously identified). To improve the chances of finding isolated cells, here experiments were carried out preferably within 1-2 days after cell passage, and always before cells reaching high confluence. Samples or sample regions with highly confluent cells were not considered for this study, since individual cell borders were not clearly distinguished from the microscope images. This selection allowed us to establish the inward-outward directions for each vesicle with respect to the cell nucleus, to separate between likely dynein-mediated or kinesin-mediated transport. Target LDs were chosen preferably at the cell periphery to avoid any eventual spurious scattering effects from the nucleus itself, and also for a more accurate determination of the inward/outward direction.

A custom LabVIEW software (Figure 5.4) was used for experimental control and data acquisition³. A mouse-click on any organelle on the live microscope

³Part of the software (specifically the click-and-drag LabVIEW panel for holographic trap positioning) was based on “Blue Tweezers”, a package for holographic tweezers created at the University of Glasgow, which we modified for our purposes

image of the cells triggered the holographic positioning of the trap at the target location and the simultaneous start of the force signal and video acquisition. At first a CCD snapshot of the whole field of view was automatically captured just after the mouse click, with a mark indicating the trap position (the laser beam was not visible, since a short-pass filter was used in the imaging path to prevent camera saturation). These images were later used to determine the inward/outward directions in order to identify the molecular motor species responsible for the movement, as described later in this chapter. Force signals from the NI-DAQ card, and video images from the CCD within a small region around the particle of interest were simultaneously acquired. The automatic configuration of a region of interest at the start of the experiment allowed for a faster acquisition, while monitoring the vesicle under study during the course of the experiment. Live video images were inspected to keep track of spurious particles in the surrounding area that could eventually get into the trap and spoil the measurements. Signals were acquired for 1-3min, and were manually stopped if a spurious organelle was seen to jump into the trap, or the original LD escaped.

The experiment was repeated for 236 different LDs distributed over 70 cells on 10 different samples.

5.4 Data analysis

5.4.1 Automatic stall event inspection

Force signals from the PSD were automatically processed off-line for detecting and analysing stall events for each experiment, by following these steps:

- Loading PSD time series (S_X, S_Y, SUM) in volts, sampled at 15kHz.
- Data smoothing: moving average over the whole series using a 50ms averaging window.
- Calculation of time derivative for S_X and S_Y signals.
- Detecting spikes in the derivatives indicating fast signal variations (force jumps), potentially indicating motor detachments from the microtubule after stall. A minimum absolute variation of 0.15V/s was used as a threshold for listing stall event candidates, both in X and Y time series.
- The time-coordinates for the detected force jumps were saved.

Then, for each listed time coordinate, two-dimensional analysis was performed to find the direction of the force jump and the parallel and perpendicular force curves around that event:

- **DEFINING DIRECTION:** A span of 0.1s before and after the spike's time coordinate was used to determine the direction of the force jump on the XY plane. Event direction was taken as the slope of a linear fit on (S_X, S_Y)

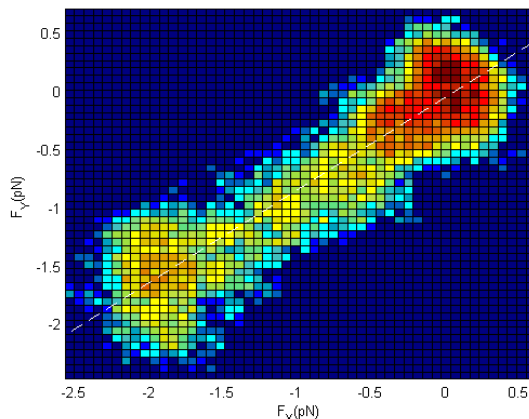


Figure 5.5: Force map (2D histogram of X and Y force components) from a 1s time window containing a complete stall force event. The pulling direction (white dashed line) is defined from a linear fit across the force jump.

data within that small fraction of time, as in the example shown in Figure 5.5

- **PARALLEL PROJECTION:** Force signals were projected onto a new set of axis defined by the direction of the force jump (parallel component), and its perpendicular direction. Parallel and perpendicular force components were plotted on a 4s window (centred on the jump) to show complete stall force curves (including pulling phase, stall, jump, and final equilibrium position), as shown in Figure 5.5
- **DIRECTION:** Motor pulling direction was defined as the opposite direction of the final force jump. The quadrant on the PSD axis was unambiguously determined according to the sign of ΔS_X and ΔS_Y increments over the force jump.
- **FORCE MEASUREMENT:** Stall force was measured on the parallel component as the difference between the plateau value (mean value of a 0.1s window immediately before the jump) and the final value (mean value of a 0.1s window after the jump). Making a differential measurement rather than absolute force measurement would take into account the local force offset conditions. Further discussion on baseline issues can be found in Section 5.4.4.

Automatic analysis delivered a large collection of events including any sharp jump on the force signal, with measured direction and force magnitude for each

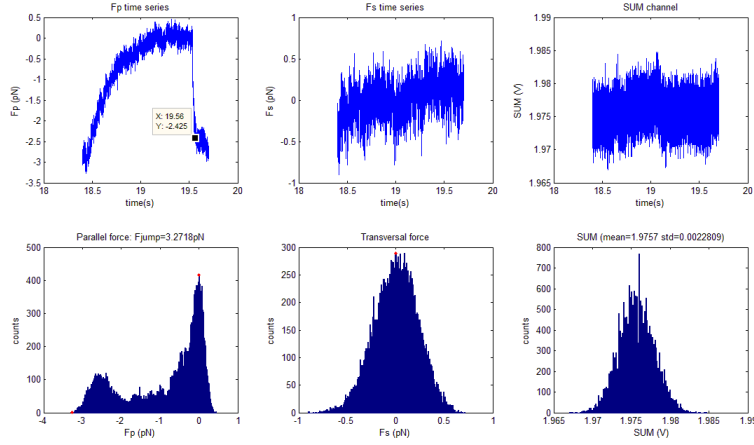


Figure 5.6: Parallel (F_p) and perpendicular (F_s) force projections corresponding to the event shown in Figure 5.5. The force jump in the parallel direction shows a difference of 2.5pN.

detected force step. However not all the automatically detected events could be directly related to the action of a stalling molecular motors. Actually, the cytoplasm of a living cell is a complex environment, with a dynamic cytoskeleton and a variety of membranous structures and organelles that can interact mechanically with the trapped object. Step-force events can arise from other sources apart from motors (e.g. binding with membranous structures, microtubule growth, collision or interaction with other organelles,...). Moreover, not all the particle excursions ended up being clear a stall events, in some cases the pulling force curve finished before reaching a situation of stall (i.e. a plateau on which a motor is pulling with no advancement). Additionally, the recorded experiments might not be perfectly unidimensional depending on the relative position of the trap and the cytoskeletal track where the motor is bound.

Hence further event filtering and correction was done through visual inspection of each short-listed event, as described in the following sections.

5.4.2 Identification of clear motor-stalling events

Visual inspection was carried out to pick-up only complete and clear stall events, which could be fairly attributed to molecular motor activity. For that purpose each event was checked to contain a complete stall force curve: force starting to grow from the baseline (motor pulling phase), a stalling plateau (motor pulling but not advancing) followed by a backwards force jump (motor detachment) towards a final constant signal (detached organelle staying at the trap equilibrium position with brownian motion only). Incomplete events (e.g. force jumps with no preceding growing curve), or force steps that were too small for reliably

measuring a force difference (e.g. changes smaller than 0.5pN, that could barely be discriminated from noise) were not considered.

Another detail to take into account is the fact that a motor can detach before reaching a stall situation. In a complete stall event the slope of the force curve would decrease as the motor advances (while its speed is reducing) finally reaching a plateau (null velocity) before detaching. However some of the detected events did not have a clear null slope region (plateau) before the detachment, and the succeeding force jump might not necessarily account for the actual motor stall force. Those events not showing a stable plateau (typically for at least 100ms before motor detachment) were disregarded.

5.4.3 Identification of one-dimensional experiments

Ideally a unidimensional experiment (with the optical trap perfectly centred on the cytoskeletal track) would show a pulling force growing along the same line as the final backwards jump (but in the opposite direction). However, since the actual track is not seen on the microscope images, in some cases the trap might have been originally positioned at a certain lateral distance from the microtubule at the beginning of the experiment. Also, the actual microtubules can bend [124] and drift over time, which might also result on the trap becoming off-centre respect to the filament, even if the original position was right.

This has two main consequences: first the applied optical force is not entirely tangent to the motor advancement, instead part of the force F_{\parallel} will be acting along the MT while part of the force F_{\perp} is being applied on the lateral direction. Even if the oblique component does not directly oppose the molecular motor advancement it is known to affect motor kinetics differently [120]. Even if only the parallel component was contributing to the motor stall, force measurements would show the total force $F = \sqrt{F_{\parallel}^2 + F_{\perp}^2}$ leading to an overestimation of the characteristic motor stall force. Another effect of non-unidimensionality is the force vector changing direction as the motor advances along the MT (off-trap), which makes the final force jump not entirely parallel to the actual cytoskeletal track. This has implications for the determination of the MT local direction from the PSD signals, which is used afterwards for inward/outward event classification.

The force component along the perpendicular direction (respect to the direction defined by the force jump) was monitored for every stall event to evaluate whether its variations were significant compared to the parallel component, specially during the growing phase of the force curve. A one-dimensional stall force experiment dataset was built by selecting those events with no major variations in the perpendicular direction (compared to the variations in the parallel component). This is to ensure that the measured force is essentially tangential to the MT (and hence contributing to the motor stall) and that the direction of the MT can be accurately determined from the direction of the force jump. Some illustrative examples containing significant variations in the perpendicular component during motor advancement are shown in Figure 5.7.

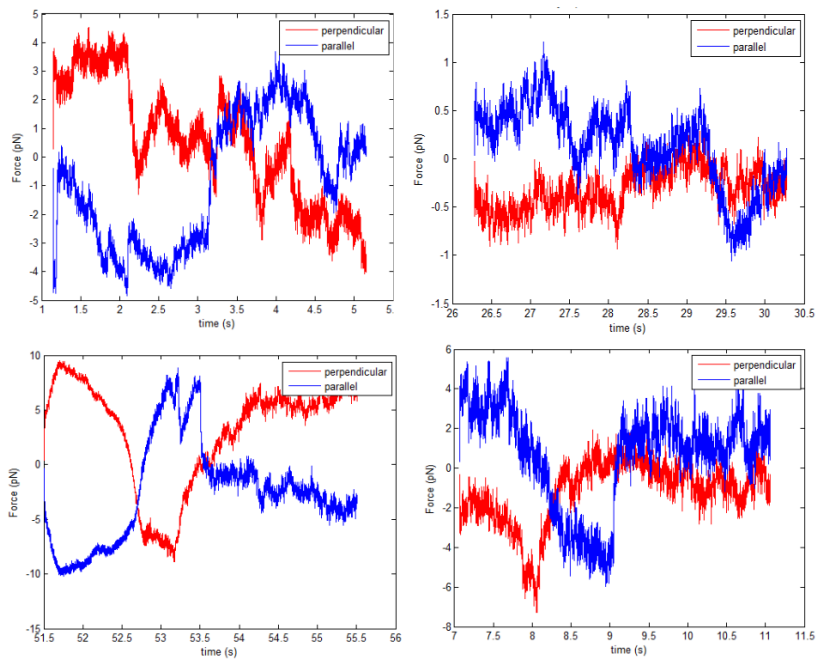


Figure 5.7: Sample stall curves with significant variations on the lateral direction (red), compared to the variations on the actual direction of the force jump (blue). For comparison clear stall force measurements are shown later in the results section of this chapter.

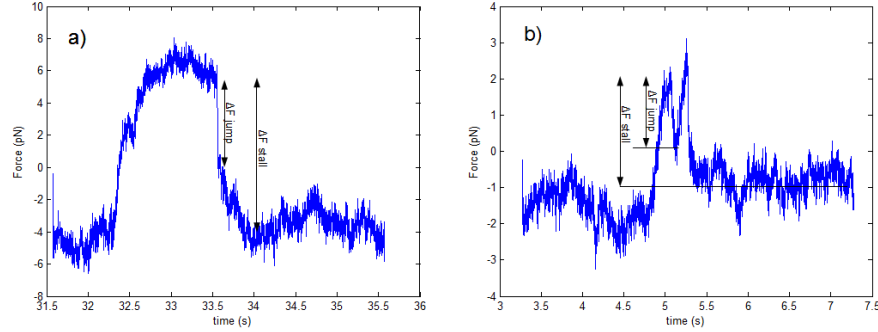


Figure 5.8: Examples where a better baseline estimation can be obtained from the event context rather than the force jump alone due to a) slow relaxation curve before reaching the baseline or b) other motor activity (e.g. a second stall curve) activity starting before the organelle reaching a stable position.

5.4.4 Baseline correction in stall force measurements

The baseline (or force offset) is the force signal with respect to which the stall force is measured, which corresponds to the trapped object staying at the trap equilibrium position (no tension applied on the motor). The signal corresponding to the initial momentum of the beam depends on each trapped object, as described in Chapter 4. This can be due to cell heterogeneities (e.g. cell membrane curvature, other cellular organelles), but also to the holographic efficiency for spot positioning at different sample locations, and the alignment of the detection system. For a given position (organelle), we expect the structural system offset to be constant, but the contributions from dynamic cellular structures may vary along the experiment. Hence, it is recommended that the baseline is determined for every stall event at the instant of motor unbinding, to take into account the updated local environmental conditions.

During the automatic analysis described in Section 5.4.1 the baseline for each stall force measurement was estimated as the mean signal immediately after the force jump (on a window of 0.1s). Visual inspection of each event over a window of 4s revealed that the force value immediately after the jump was not always corresponding to the ultimate relaxed position of the organelle (estimated trap equilibrium position). In fact, some curves described further small variations on the force signals following the sharp jump before reaching a final stable force value. This could be due e.g. to further motor activity starting after the unbinding before the organelle reaching the trap centre (Figure 5.8b). Also, a short relaxation phase could be observed in some cases (Figure 5.8a) as the organelle travels fast from the stall position to the trap centre after motor detachment, which is likely due to local cytoplasm viscoelasticity.

5.4.5 Comments on global baseline fluctuations

Even if a short baseline is observed after a stall event (within a 4s window), there can be long-term force fluctuations/drifts measured on a given organelle over the whole experiment (e.g. on a 60s long measurement). These global baseline fluctuations were observed in some organelles, while other ones had a stable baseline for the whole time series (apart from eventual stall events). Both situations could be observed on the same cell, on different organelles, or even on the same organelle at different times. A couple of examples showing the PSD signals over the course of a complete experiment are shown in Figure 5.9.

This effect can be due on one hand to spurious cell organelles moving in the vicinity of the trapped object along the experiment (or part of the experiment), which would add varying contributions on the initial momentum of the beam, even when the spurious bead is not evident on bright field images (e.g. if it is out of focus). The presence of scattering structures also results in additional light losses (due to back-scattering) and these experiments might also show fluctuations on the SUM channel of the PSD, as described in Section 5.4.6.

On the other hand, other biological force sources could be acting on the trapped organelle apart from the motor/s under investigation. This makes *in vivo* stall force measurements more difficult to interpret as opposed to *in vitro* experiments where all the active elements are under control. Our best approach for discriminating molecular motor force data from other sources is considering clean stall force events only, as already described in Section 5.4.2. We expect instantaneous differential force measurements (with respect to the local baseline) to account for the motor stall force.

Hence, apart from the analysis performed on all locally clear stall events, a subset of data was built using only those measurements from experiments with a global baseline. On those cases we expect no ambiguity on the reference beam momentum. The choice of stable experiments was based on the analysis of S_X and S_Y signal's standard deviation together with visual inspection. Experiments with standard deviation lower than 0.5pN in both channels were selected. Experiments with higher standard deviations in one or both channels were included only if the baseline was visually stable (i.e. events with stronger force variations, but consistently coming back to the same reference signal after motor activity). If baseline fluctuations were observed to begin at a specific point of an experiment (e.g. due to a spurious bead spontaneously getting into the proximity of the trapped bead), only experiments within the stable part for the experiments were considered for this subset. An example of force signals where conditions changed at some point during a measurement is shown in Figure 5.10.

5.4.6 Evaluation of light losses

Accuracy of force measurements using the momentum method is relying on the capture of most of the scattered light onto the PSD. Since the SUM channel of the PSD is proportional to the power of the collected beam, we can check the

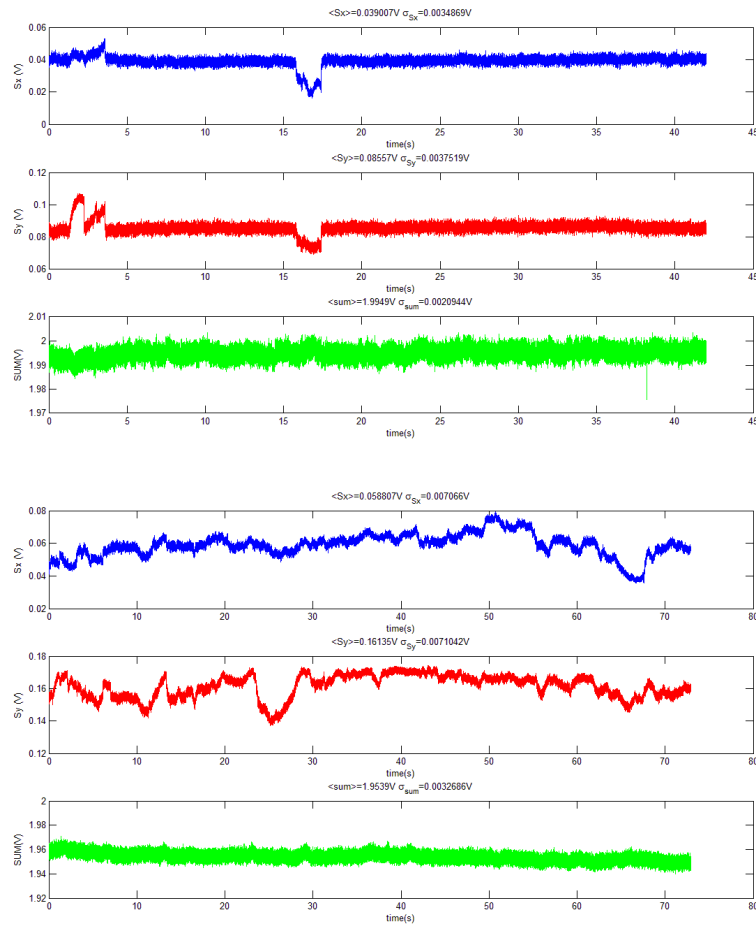


Figure 5.9: Examples of PSD signals S_x (blue), S_y (red) and SUM (green) on two trapped LD in A549 cells. Some stall events are visible along the signals. However, the first case (a) has a stable reference line, where the LD stays after every stall event, while in (b) the baseline fluctuates along the experiment. In (c) something happened during the experiment, as clearly seen in the

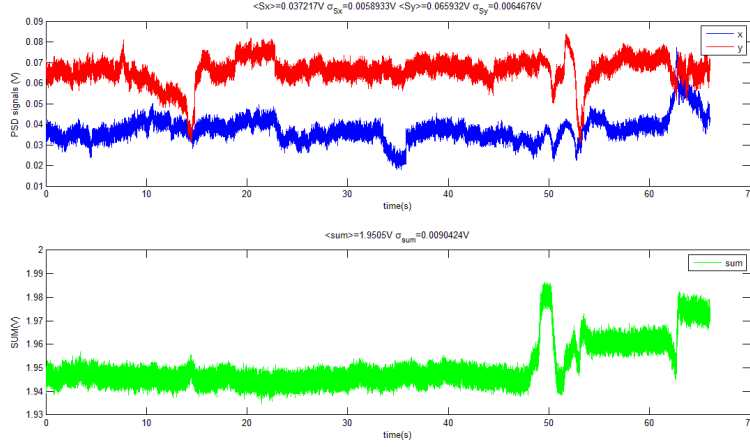


Figure 5.10: Example of time series instabilities started around $t=48s$ (as seen specially in the SUM channel). Force jumps after this point were not considered for the "stable baseline" subset.

variability on this signal for detecting eventual light losses as the particle moves away from the trap centre during a stall event. We measured the fluctuations in the SUM channel over a window of 4s centred on the jumps following motor stall. Relative power variations (SUM standard deviation / SUM mean) were found to be 0.12% in average (with 0.05% standard deviation), and 95% of the events all falling within a range of 0.08%-0.18% (Figure 5.11a) Power fluctuations on stall events are reasonably low, and we do not expect any important bias on stall force measurements due to light losses.

If we analyse the global fluctuations on the SUM channel over the whole time series for each experiment (typically lasting $\sim 60s$) we observe higher variations (standard deviation / mean): 0.32% in average (with 0.33% standard deviation), and 95% of the experiments falling within a range of 0.09%-0.88%. Variations in collected power are higher in the global time series (Figure 5.11b) than in the stall event surrounding time (Figure 5.11a). This is possibly associated to the movements or changes in other cell structures, that may be more relevant on longer time scales, as well as possible particle defocus if the bead is pushed away from the trapping plane. Changes in the beam scattering profile would also be affecting the baseline for force measurements which motivates determining the local baseline at the time of each stall event as described in Section 5.4.4, rather than using a global baseline reference.

5.4.7 Estimation of error in stall force measurements

Essentially there are two main contributors to the error in our stall force measurement: the accuracy of the momentum method inside cells and the accuracy

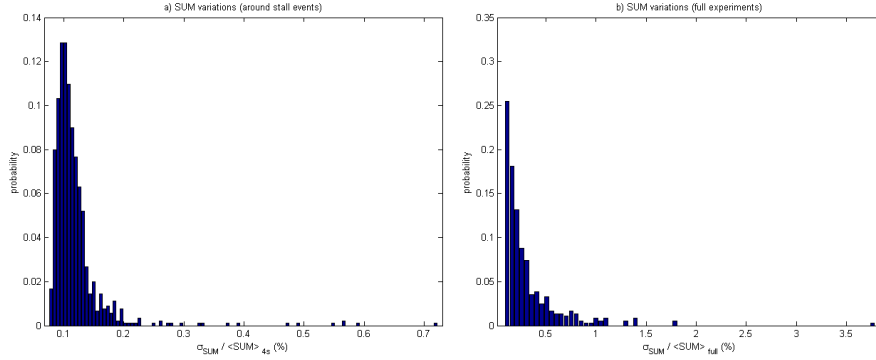


Figure 5.11: Histograms of relative fluctuations on the power measured by the PSD calculated as the quotient between standard deviation and mean value of the SUM channel a) for 4s time windows around detected stall events b) for the full time series of measurements at fixed organelles/positions.

in determining the local baseline and the plateau. The first one can be estimated from the intracellular system calibrations (based on active-passive measurements), which have coefficient of variation of of 24% (as seen in Chapter 4). The second error contribution depends on the stability of the baseline and plateau, and the ability to identify a reference force value from the context. We estimate an uncertainty of 0.5pN each, which gives an uncertainty of 0.7pN in the force difference. That corresponds to 18% uncertainty for the average stall force measurement of ~ 4 pN.

5.4.8 Determination of inward/outward directions of stall events

In order to associate each event to a particular motor type, the pulling direction of the motor (plus or minus end) has to be determined. Even if a set of radial MT is a simplistic description of the actual cytoskeletal network we expect that statistically most of the outward-directed transport (towards the cell periphery) comes from kinesin activity (moving towards MT plus end) while most of the inward-directed transport (towards the cell nucleus) is due to dynein activity (moving towards MT minus end). This is a common assumption in other *in vivo* organelle traffic and stall force studies [36, 78].

Each event was classified according to its relative orientation with respect to the cell geometry. This is done by first estimating the cell inward/outward direction at each trapped organelle location (with respect to the cell nucleus), and then evaluating the motor pulling directions with respect to the inward/outward axis as described in the following sections.

5.4.8.1 Cell polarity

Under normal cell growing conditions microtubules are expected to be mostly distributed in a radial fashion, nucleating from the MTOC (typically located next to the cell nucleus) and growing towards the cell periphery. However the MT cytoskeleton is a dynamic system that changes at the pace of tubulin dimer polymerization/depolymerization over the whole cell cytoplasm. They also can bend forming a complicated dynamic network, being molecular motors an important player on the cytoskeleton shaping process as well [125].

The cell outward direction at the position of each specific organelle was determined as the line going from the centre of the nucleus to the trapped organelle (being the inward direction the opposite one). Note that this is just an estimation of the expected MT direction, since the actual position of the MTOC is not known (although it should be next to the nucleus). Also MTs are dynamic and do not necessarily describe perfect straight lines from the centre to the cell periphery. Hence a certain acceptance cone centred on the estimated inward/outward directions will be used for motor classification, as described further ahead in this chapter.

Nucleus size in the A549 cells in our samples is in the range of 4-10 μ m diameter (average value of 7.3 μ m diameter). The MTOC can sit at any position adjacent to the nucleus. Fluorescent labelling on fixed cells (immunofluorescence) or even on living cells (transfection) could help clarifying cell geometry and the exact MTOC position. However we did not use it on the final stall force- experiments to avoid any light losses due to the interaction of the trapping beam with fluorophores. Indirect evidence suggests that increased light absorption may take place in cells containing fluorescent materials even if the incident light is out of the absorption spectra of the fluorophores, e.g. due to multi-photon processes. Cell nucleus could be easily identified from bright-field images. Ambiguity on MT polarity due to unknown MTOC location was reduced by considering only LDs far from the nucleus. Experiments closer than twice the average nucleus radius were not considered on the inward/outward datasets to reduce the chances of miss-classified events.

5.4.8.2 Relative orientation of PSD and CCD axis

The direction of stall events could not be systematically determined from CCD images, specially for small organelle excursions (e.g. in cases with high trap stiffness). This is due to the limited spatial and temporal resolution on video images, which challenges displacement measurements, especially in those cases with a strong trap, where organelle excursions are very small. However PSD signals already give a precise measurement of the pulling force direction for each stall event on the XY plane (on PSD axis), which can be converted to CCD directions as long as the relative orientation of the two detectors is known.

The relation between PSD and CCD axis was measured by recording the response of an optically trapped 1 μ m polystyrene bead in water under the effect of drag forces on a variety of directions. A piezoelectric stage was used to

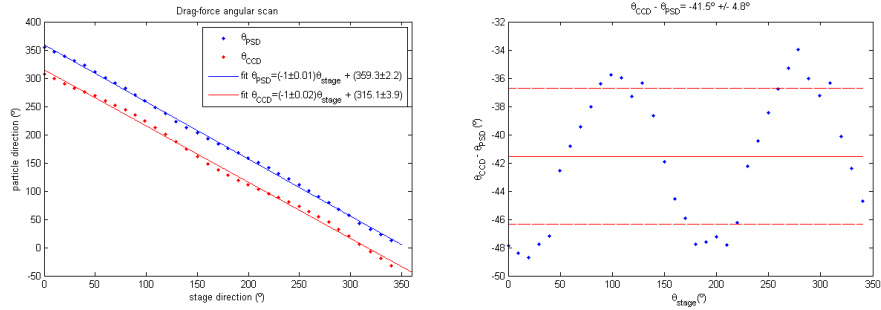


Figure 5.12: a) Direction of the trajectory of a $1\mu\text{m}$ bead trapped in water for different directions of the applied drag force (stage). b) Angular difference between CCD movement and PSD movement for different stage directions, with mean value (solid line) \pm standard deviation (dashed lines).

oscillate the sample at 5Hz for 1s at a tunable direction over a range of 360° . A linear fit both on PSD and CCD (particle tracking) XY trajectories showed the direction of particle motion as seen by each detector. The quadrant of the angle was unambiguously determined from the X and Y signals on the initial part of the oscillation. The obtained relation between the direction of PSD trajectories (θ_{PSD}) and CCD trajectories (θ_{CCD}) was a simple axis rotation (angle shift in shown in Figure 5.12), with an average angular difference of:

$$\theta_{CCD} - \theta_{PSD} = -45.5^\circ \pm 4.8^\circ \quad (5.1)$$

From the linear fit in Figure 5.12a, we get:

$$\begin{aligned} \theta_{PSD} &= (-1,011 \pm 0.011)\theta_{stage} + (359.3 \pm 2.2)^\circ \\ \theta_{CCD} &= (-1,00 \pm 0.02)\theta_{stage} + (315.1 \pm 3.9)^\circ \end{aligned} \quad (5.2)$$

with 95% confidence bounds. Hence, another estimate for the relative orientation of the two devices is, which is compatible with the average value given in Eq. 5.1

Even if the particle direction responds smoothly as the external drag force turns around, interestingly a closer look at the residuals of the linear fits in Figure 5.12a as well as the PSD vs. CCD anomalies (Figure 5.12b) reveals a sinusoidal trend with twice the periodicity of the drag force rotation, especially on the video trajectories. This periodic anomaly is presumably given by the asymmetry of the optical trap. Trap lateral stiffness is known to be slightly different for different directions e.g. due to small beam aberrations and polarization effects on high-NA focusing optics, that usually makes the optical traps elliptical. This small asymmetry would make the particle respond differently depending on the direction of the applied external drag force (which is parallel to the stage's velocity).

5.4.8.3 Classification of inward/outward events

For each event, the direction of the force was translated to CCD axes using Eq. 5.1 and then the angular distance between the motor pulling and the cell outward direction was evaluated. Those experiments where the outward/inward axis for the trapped organelle was not clear (e.g. vesicles closer than 10 μ m to the nucleus centre, or unclear cell geometry due to higher confluence) were excluded from the polarity classification.

Those events falling inside a cone of $\pm 60^\circ$ from the outward direction were classified as plus-end events, and those events with a pulling direction falling inside a cone of $\pm 60^\circ$ from the inward direction (i.e. 120° - 240° from the outward direction) were classified as minus-end events. The rest of the events were also excluded for the separate inward/outward statistics, but they were still taken into account for the global stall force histograms. Some illustrative examples of cells with indicated motor pulling directions on a given organelle are shown in Figure 5.13. Note that events are usually repeated along a line (microtubule direction). However in some experiments there are more than one axis, presumably due to the trapped organelle being close to different microtubules, and alternating between different tracks.

5.5 Results

5.5.1 Stall force measurements

Measured stall forces mostly fall in the range of 1-10pN, with a distribution shown in Figure 5.14, and statistics summarized in Table 5.2. A variety of grouping criteria have been used for the separate analysis of relevant subsets of measurements, including automatic detection of force jumps, visual checks for stall-like events, and global stability of the baseline:

- I. All automatically detected force jumps.
- II. Stall-like events. These events passed visual checks, with local baseline estimations based on a 4s time window around the force jump time coordinate.
- III. Stall-like events with globally stable baseline only.
- IV. Stall-like events with globally unstable baseline only.

All histogram bin sizes (h) were chosen following Freedman-Diaconis rule⁴:

$$h = 2 \text{IQR} n^{-1/3} \quad (5.3)$$

where IQR is the interquartile range of the dataset, and n the number of elements. This choice is less sensitive to outliers than other methods based on

⁴Note that the fitting routine works directly with the data, independently of the histogram bin size (which is only used for display purposes).

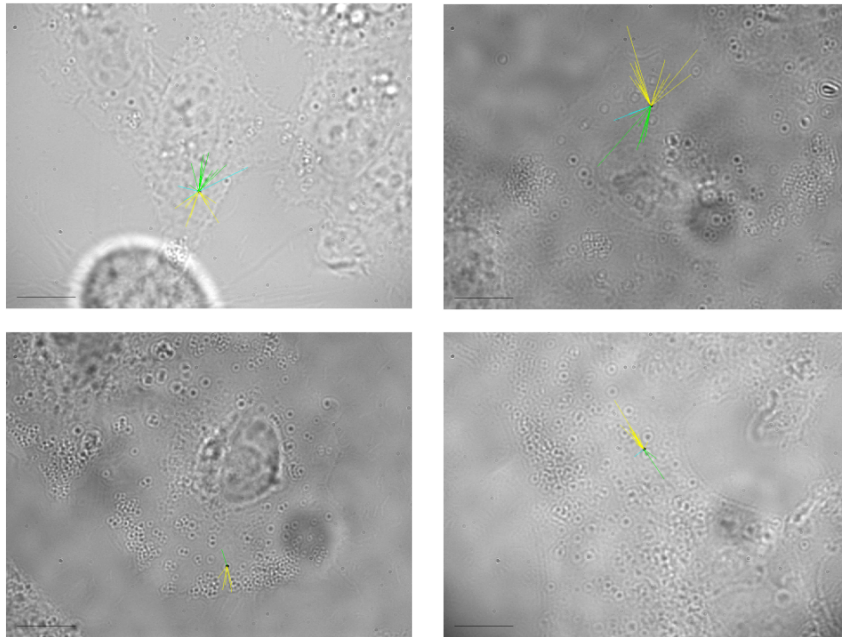


Figure 5.13: Microscopy images of A549 cells with measured stall force vectors (color lines) starting from the trapped organelle position. The scale bar corresponds to 10pN (for force vectors) and 10 μ m (cell image). Yellow/green lines indicate events that are classified as outward/inward respectively, while cyan lines indicate events that are not classified (do not fall within the $\pm 60^\circ$ cone from the nucleus-organelle).

Group	N	Mean	σ	Median	Max	95% perc.	>15pN
(I) All force jumps	14505	1.8	2.1	1.4	84.6	5.0	0.2%
(II) Stall-like	1232	4.1	2.4	3.6	28.6	8.7	2.7%
(III) Stable baseline	252	3.8	2.2	3.2	12.3	8.5	0%
(IV) Unstable baseline	980	4.2	2.5	3.6	28.6	8.7	0.5%

Table 5.2: Statistical parameters (N, mean μ , standard deviation σ , median, maximum, 95th percentile and fraction of events above 15pN) of force measurements datasets. Units are piconewton for the all the the columns (except for N events which are counts). Groups I-IV correspond to different selection criteria: (I) All automatically detected force jumps, (II) clear stall force curves (visually checked) with local baseline estimation within a 4s window around the force jump. (III) and (IV) are subsets of group (II) with globally stable or unstable baseline respectively.

	Dir.	N	μ	σ	Med.	Max	95% perc	>15pN	p_{KS}	p_{WRS}
II	Out	343	4.2	2.5	3.6	19.0	8.8	0.6%	0.926	0.938
	In	347	4.1	2.2	3.6	16.5	8.5	0.3%		
III	Out	50	4.5	2.6	3.5	11.3	9.7	0%	0.374	0.261
	In	57	3.7	2.0	3.5	10.8	7.7	0%		

Table 5.3: Separate statistics for inward/outward-directed stall-force events for groups II (all stall-like events) and III (only those stall-like events in vesicles with globally stable baseline). Units for mean (μ), standard deviation (σ), median, maximum, and 95th percentile are in piconewton. The two last columns show the p-value of the Kolmogorof Smirnov (KS) and Wilcoxon Rank Sum (WRS) tests comparing inward and outward datasets.

the standard deviation of the data. Note that data binning is used for histogram representation purposes only, and this choice does not affect the statistical analysis.

5.5.2 Inward/outward events

Stall-like force events were then classified in subsets based on movement direction with respect to the cell polarity as described in Section 5.4.8. The outward/inward subgroups are presumably dominated by kinesin activity (towards microtubule “+” end) and dynein activity (towards microtubule “-” end) respectively. Sample curves for the two directions are shown in Figure 5.15. The key statistics for stall-like events (considering globally stable baseline or not) are shown in Table 5.3. Two statistical tests have been used to compare the inward-outward stall force distributions.

The two-sample Kolmogorov-Smirnov test determines whether two populations are drawn from the same continuous population. We used “kstest2” from MATLAB statistical toolbox for testing the null hypothesis of the two

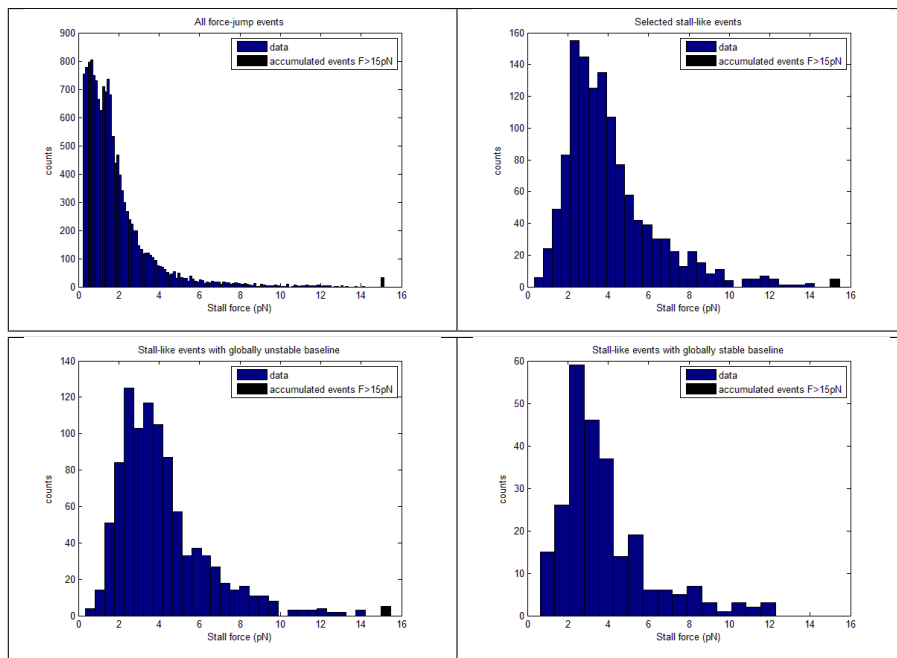


Figure 5.14: Histogram of measured stall forces grouped according to the listed selection criteria I to IV.

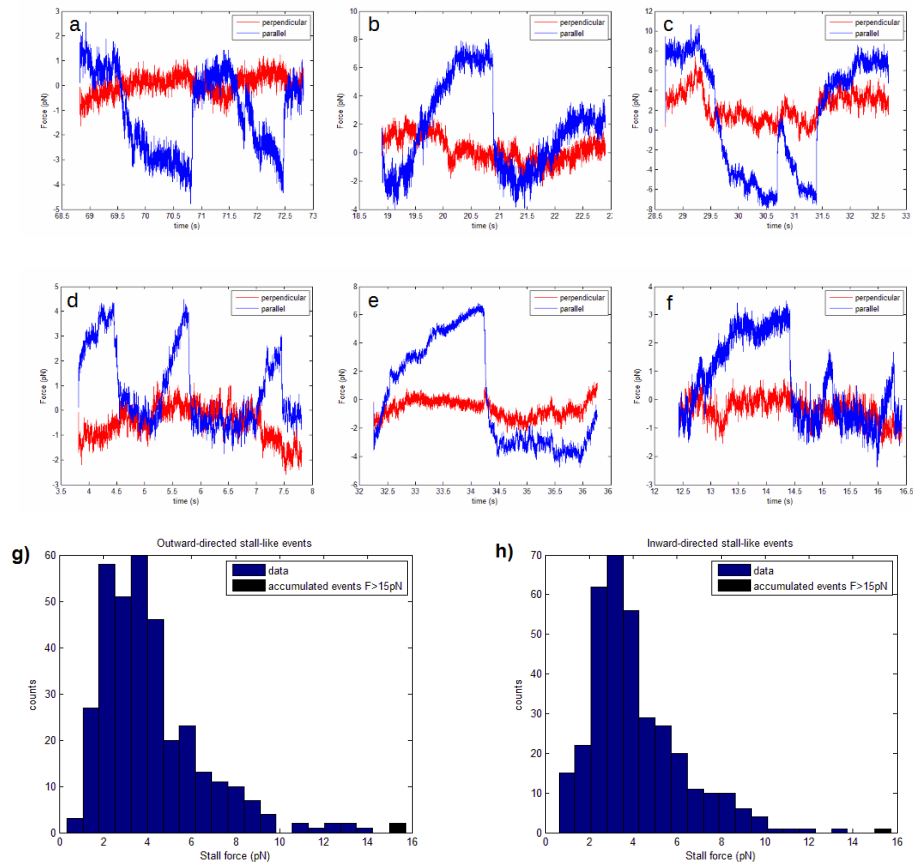


Figure 5.15: Sample stall curves pulling towards the outward cell direction (a-c) and inward cell direction (d-f), and stall force histograms in the outward (g) and inward (h) directions.

samples being equal against the alternative hypothesis of samples being unequal, with 0.05 significance level. A Wilcoxon-Rank Sum tests the hypothesis that two independent samples come from a distribution with equal medians. We used “ranksum” from MATLAB statistical toolbox to compare the inward / outward substes.

Both statistical tests failed to detect significant differences between the inward and outward groups. In all comparisons the p-values are above the 0.05 significance level, as shown in Table , and hence the null hypothesis of the two samples being the same cannot be rejected.

One would expect that outward/inward events to be mostly kinesin/dynein mediated respectively and hence the force distributions should be different if the motors behave similarly as *in vitro* studies. However, our measurements show similar force distributions for both outward and inward directed events. This is more in line with what was observed in [78] also in A549 cells, suggesting a possible tug-of-war situation in our experiments as well. The force distributions are less comparable e.g. to [36] or [70], where clear peaks at approximate multiples of an elementary force were observed for both inward and outward events.

Stall experiments inside living cells are more complex than *in vitro* experiments, and further work is required to build a better understanding on how motors coordinate inside cells and how other elements in the cell (e.g. cytoskeletal filaments, obstacles) may be interfering with the stall force measurements. A tug-of-war behaviour inside the cells we studied, rather than single motor experiments, could be the reason for the force distributions we observe, as suggested in [78].

5.5.3 Evidences of multiple motors in force measurements

Some stall events showed a split force jump instead of a single sharp decay from the stall value to the baseline. This has been observed both in outward and inward directed events, and may be an indicator of multiple motors sharing the force load. On a multiple-motor scenario the motor-trap force balance is lost after one motor unbinds. Other active motors would then unbind in cascade unable to hold the trap force by themselves. This can happen straight away resulting in single sharp high force jump corresponding to the total motor force. But there could also be a delay before secondary motor detachments, especially if secondary motors are bound to the microtubule far behind the leading motor and they do not all detach from the microtubule at the same time.

In the examples shown in Figure 5.16 there is some evidence of the presence of multiple motors. In the first case (a) two stall events take place consecutively, the second one with twice the force of the first one (that could be the elementary force of one single motor). In the second example (b) there is a split stall event, in which there is a partial jump before reaching the final baseline, as well as a temporary halt at an intermediate stage of the next stall curve, at half the total force. The split-step behaviour on the force jump could be because of two motors being bound to the MT at significantly different positions so that the force load is not shared evenly. In that situation, the stall of one (leading) motor

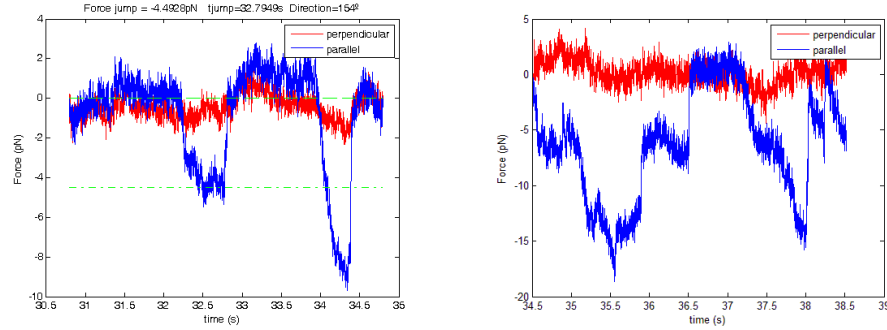


Figure 5.16: a) Two consecutive stall curves with approximately double the force. This event was towards the inward cell direction. Note one first stall of 4.5 pN followed by a second stall event of 9.4 pN. b) Stalls at different stages, there is some intermediate stall situation at 6-7 pN, but in some cases the motor bead proceeds further, up to ~ 14 pN, which could be explained by the combined efforts of two motors of the same kind.

would not imply the stall of the motor behind (which could be holding a lower amount of force due to its different relative position to the vesicle centre). In that case only after the vesicle journey towards the trap centre starts (following the first unbinding) would the tension on the secondary motors increase enough to stall them, creating a short secondary plateau before they also unbind.

If multiple molecular motors of the same type pull simultaneously with additive forces, as it happens *in vitro*, one would expect stall force histograms to follow a distribution with peaks at multiples of an elementary force, e.g. as observed for kinesin-1 in [112]. In our case we observe one main peak around 3 pN in the stall force histograms, together with smaller concentrations of events at higher forces (up to 9 pN, and then again some events around 12 pN). A common approach is fitting a mixture of Gaussian functions to the force distribution to detect peaks at specific forces. e.g. in [70] they observe clear peaks at 2.6 pN and 5.2 pN in their stall force distribution.

We used “`gmdistribution.fit`” function from MATLAB Statistical Toolbox for fitting the force distribution to a Gaussian mixture model. The optimum number of Gaussian functions to fit was chosen after running the fitting routine for 1 to 10 Gaussian functions, and using the minimum in Akaike Information Criterion (AIC) and Bayesian Information Criteria (BIC) for choosing the best model, as shown in Figure 5.17 This allows to find the fairest number of parameters for describing our force distributions without risk of over parametrizing the system. Note that the multiple-Gaussian fitting routine uses the original dataset rather than the histogram points, so there is no loss of statistical information on data binning. Fitted curves were normalized so that the total area under the curves matches the total area of the histogram, while keeping the relative weight for each Gaussian as given by the fitting routine.

Only data up to 10pN was considered for the multimodal fit. Forces higher than 10pN represent less than 3% of the data, and are not relevant for fitting peaks within the 2-8pN region, which is where the main peaks are. However, it is relevant to know that there are some events above 10pN forces, which may only be achieved by molecular motor cooperation, or eventually by additional force sources within the cell (e.g. microtubules or bundles of cytoskeletal filaments drifting across the cytoplasm). The amount of detected higher force events is scarce in our data, since most vesicles would escape the trap at higher forces (for a given trapping power). However this does not mean that higher force events are rare within the cell, but rather that the way we detect them was limited. In order to increase the amount of detected events at higher forces without increasing the trapping power too much to create a thermal shock on the cells, alternative methods could be used. For example, artificially-induced high-refractive index organelles could be used as handles for intracellular force experiments, as described in [24], or one could potentially use phagocytosed beads with high refractive index or anti-reflection coatings as in [126] to enable higher trapping forces inside cells.

The main lower force peak around 3pN we observe in Figure 5.14 for both outward and inward events could potentially be associated to single motor stall events, while higher forces (with a broader distribution around 6pN, or occasionally up to 19pN) would likely be accomplished by multiple motor collaboration. The results of the multimodal Gaussian fits are shown in Figure 5.17.

For the inward direction, we found peaks at 3.1pN (with 1.1pN width, accounting for 70% of the events) and 6.2pN (with 3.1pN width, accounting for 30% of the events). For the outward direction, there is a discrepancy in the best number of Gaussian components to fit according to AIC or BIC criteria. If 2 Gaussian functions are used (as suggested by AIC criterion), a main peak at 3.0pN (with 1.1pN width, accounting for 67% of the events) and a secondary 5.9pN peak (with 3.4pN width, accounting for 33% of the events) are found. The 3 Gaussian fitting found peaks at 2.2pN (0.4pN width, 29% of events), 3.7pN (0.7pN width, 44% of events) and 6.3pN (width 2.9pN, 27% of events) for the outward distribution.

Overall, the presence of peaks at multiples of an elementary force is less clear in our data than in other studies e.g. [70, 36], but our distributions are more in line with the observations in [78], also in A549 cells. Here they suggest the possibility of different motor types competing on a tug-of-war fashion in intracellular traffic, which effectively may result in a broader distribution of peaks that look more like a plateau at higher forces rather than actual peaks. In that case, the measured optical forces we observe would rather account for the force imbalance between different number of opposing motors. The fact that a mixture of motor types could be acting together for both outward and inward directed transport could explain why the outward-inward force distributions look more similar than one would expect from transport events dominated by one single motor type for each direction.

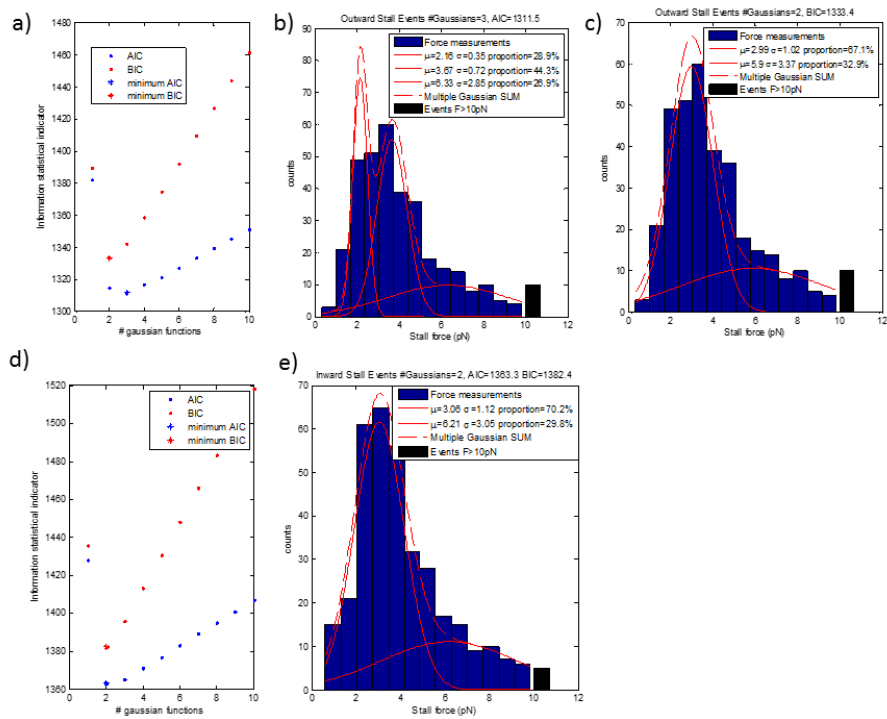


Figure 5.17: Multiple Gaussian fitting in Outward (a-c) and inward (d-e) clear stall force distributions. The values of the Akaike Information Criterion (AIC) and Bayesian Information Criterion (BIC) for each dataset are displayed in a) and d), showing the minimum values that allowed us to choose the most suitable appropriate number of Gaussians to take into account for the multimodal distribution.

5.6 Further comments on intracellular force measurements

The main advantage for the momentum method with respect to trap stiffness calibration methods is the fact that force signals are already meaningful from the start as soon as any vesicle is trapped. This offers the freedom for easily moving from one vesicle to another based on the observed activity, with no need of spending time in calibrations for each vesicle separately from data acquisition.

Another potential advantage of the momentum method for *in vivo* experiments is the possibility of measuring forces beyond the linear region of the optical trap. This can reduce the amount of power needed for stalling molecular motors, or may provide useful force data even in those experiments where a vesicle may be escaping from the trap for higher force events.

For trap stiffness-based measurements, like the rest of published intracellular studies so far, it is crucial to keep the conditions in which the trap was calibrated, hence particle defocus and drifts may be a problem over long measurements. This is less of an issue with the momentum method, as long as a local baseline can be reliably determined for each event after motor detachment, once the trapped organelle jumps into the centre of the trap.

The classification accuracy between inward/outward events could be improved in further studies e.g. using fluorescent techniques to label the MTOC in living cells, so that the position where the microtubules originate from and grow to can be unambiguously determined, rather than guessing the microtubule polarity from the vesicle position relative to the cell nucleus. When combining trapping studies with fluorescent labelling, it is important to make sure that the fluorescent marker does not interfere with the trapping light. Future experiments in specific regions of highly polarized cells (e.g. neurons or NG108 cells, with vesicle traffic along the axons) would also allow to unambiguously classify inward-outward events and make sure of which is the leading motor type that is being stalled in each experiment.

Regarding biological activity (which can affect the force baseline, and the actual motor activity), there could be some dependence on the phase of the cell cycle (e.g. interphase, cellular division, . . .), which is something we did not explore in this study. However, cells are known to spend 90% of their life in a growing phase (interphase), and only a small portion of their life in other stages involved in cell division, so we expect most of our cells to be in the interphase. Depending on the addressed biological problem, one could decide to restrict to a specific phase on the cell cycle, e.g. for studying motor interactions with the mitotic spindle during cell division [127].

Other biological problems such as micro-rheology in cells or the study of membrane protein dynamics [128] could benefit from the force technique we presented here, whose potential applications in live sciences go beyond the study of molecular motors we introduced in this chapter.

Chapter 6

Final conclusions

With the work presented in this thesis we reached the following conclusions.

Regarding the holographic manipulation of groups of traps:

- It is possible to manipulate rigid blocks of particles in holographic optical tweezers in real time, with no need for intensive hologram calculations, by using an hybrid method combining pre-computed Gerchberg-Saxton holograms with random mask spatial multiplexing.
- The efficiency of the hybrid method (quantified as the average trap stiffness on an array of trapped microbeads) decreases as the inverse of the number multiplexed holograms.
- For a fixed number of traps, the average trap stiffness decreases as well as a power law of the number of multiplexed blocks.

Regarding the active-passive calibration:

- It is possible to optically trap organelles inside living cells and use the active-passive calibration method (based on the Fluctuation Dissipation Theorem) to quantify the trap stiffness and the viscoelastic parameters of the local environment.
- Trap stiffness measurements have been demonstrated in *S. Pombe* (living yeast) cells. Trap stiffness at constant power varies significantly across different trapped objects, remarking the need for local calibration for each trapped object.
- Trap stiffness calibrations are independent of the perturbation frequency within the explored 5Hz-75Hz range, and the trap force increases linearly with the laser power, as expected from any optical trap.
- Biological activity may introduce uncontrolled perturbations on the system during the calibration process. This can be detected and taken into account during data analysis.

- The measured viscoelastic moduli in *S. Pombe* cells are reasonable, and comparable to microrheological studies by alternative methods.
- We designed a custom-made user-friendly MATLAB interface to automatically analyse active-passive calibration data.

Regarding the momentum method:

- It is possible to combine both momentum-force and active-passive calibration on a single set-up, provided that the most restrictive conditions of both methods are met.
- The direct force calibration constant method (based on beam momentum changes) is compatible with active-passive calibration results on trapped intracellular organelles in living A549 cells, as long as the conditions for both methods are met.
- The force constant is compatible with active-passive calibration results at the higher frequencies (64-70Hz). The discrepancies at lower frequencies can be potentially attributed to noise due to biological activity, which seems to be more remarkable in A549 than in *S. Pombe* cells.
- Hence, the effect of the cellular membrane in A549 cells does not suppose a significant problem for calibration-free momentum based measurements inside living cell culture monolayers.
- The signal offset for force measurements is dependent on the trapped object, and needs to be determined for each experiment.

Regarding molecular motor forces measured in living A549 cells

- The potential of calibration-free force measurements has been illustrated by measuring molecular motor forces in living cells.
- Clear stall force curves are observed in both outward and inward directions.
- The obtained stall force measurements with local baseline corrections are comparable to other molecular motor studies in the literature.
- We do not observe clear statistical differences between inward-directed and outward-directed stall events.
- Evidence of multiple-motor activity is found in some of the detected signals.

Nomenclature

AOD	Acousto-Optic Deflector
BFP	Back Focal Plane
CGH	Computer-generated holograms
DF	Direct Force method based on optical momentum measurement
FDT	Fluctuation Dissipation Theorem
FFT	Fast Fourier Transform
GS	Gerchberg-Saxton
HOT	Holographic Optical Tweezers
LD	Lipid Droplet
PSD	Position Sensing Detector
QPD	Quadrant Photodiode
RM	Random Mask
ROI	Region of Interest
SLM	Spatial Light Modulator
YPD	Yeast extract Peptone Dextrose

Agraïments / Acknowledgements

The research presented in this thesis is the result of the joined efforts of many people that, one way or another, helped me bringing this PhD work to a conclusion. I am extremely thankful to all the colleagues and friends that have been part of this process. Agraïixo el finançament rebut per part del Ministeri d'Educació, Cultura i Esport a través del programa de "Formació de Professorat Universitari (FPU)".

Vull agraïr a l'Estela i en Mario el fet d'haver acceptat dirigir-me la tesi doctoral i orientar-me en aquest procés d'aprenentatge, per la seva disponibilitat, i per ajudar-me a avançar al llarg d'aquests anys, especialment en els moments més difícils. Un fort agraïment a l'Arnau i la Carol que, a part de compartir amb mi la seva experiència en pinces òptiques, mesures de força, i treball amb cèl·lules vives, han estat també un referent i un punt de suport durant el doctorat que valoro molt. També vull dedicar un agraïment especial a l'A. Carnicer pel seu guiatge en els meus primers passos en el món de la investigació, així com també al traspassat D. Petrov per la seva dedicació i confiança durant la meva etapa de Summer Fellow a l'ICFO. Un record agraït a tots els companys de despatx, passadís, i de facultat en general, amb qui he tingut el gust d'aprendre, treballar, i compartir estones fantàstiques durant aquests anys!

I would like to thank the Optical Trapping Group in the NBI and DTU in Denmark that made my short 4 month-stay (back in 2010) a very productive and enjoyable experience. Special thanks to Lene and Kirstine for hosting me and supervising the project, and to Andrew and Nader for being extremely helpful in the lab.

And finally a huge THANK YOU to all friends I've met during this years living in Barcelona, Denmark and, more recently, Scotland. Thank you all for all the great moments we've shared, and looking forward for more to come! I really appreciate all support and encouragement I've received from so many people, specially during the writing process.

Vull acabar agraït de tot cor a la meva família i amics més propers pel seu suport incondicional en aquest procés de creixement professional i personal. Moltes gràcies!

List of publications

Part of the work carried out during the development of this thesis is presented in the publications listed below.

Articles in scientific journals

- A. Carnicer, J. Mas, J. Cuadros, I. Juvells, and X. de Pedro, “Seguimiento del aprendizaje mediante análisis de trazas en una simulación de trampas ópticas,” *Óptica Pura y Apl.*, vol. 43, no. 2, pp. 119–125, 2010.
- J. Mas, A. Farre, J. Cuadros, I. Juvells, and A. Carnicer, “Understanding Optical Trapping Phenomena: A Simulation for Undergraduates,” *IEEE Trans. Educ.*, vol. 54, no. 1, pp. 133–140, Feb. 2011
- J. Mas, M. S. Roth, E. Martín-Badosa, and M. Montes-Usategui, “Adding functionalities to precomputed holograms with random mask multiplexing in holographic optical tweezers,” *Appl. Opt.*, vol. 50, no. 10, p. 1417, Mar. 2011.
- I. Verdeny, A. Farré, J. Mas, C. López-quesada, E. Martín-Badosa, and M. Montes-Usategui, “Optical trapping: A review of essential concepts,” *Óptica Pura y Apl.*, vol. 44, no. 3, pp. 527–551, 2011.
- J. Mas, A. C. Richardson, S. N. S. Reihani, L. B. Oddershede, and K. Berg-Sørensen, “Quantitative determination of optical trapping strength and viscoelastic moduli inside living cells,” *Phys. Biol.*, vol. 10, no. 4, p. 46006, Jul. 2013.

Conference proceedings

- J. Mas, A. Farré, C. López-Quesada, X. Fernández, E. Martín-Badosa, M. Montes-Usategui, A. Farre, C. Lopez-Quesada, X. Fernandez, E. Martin-Badosa, and M. Montes-Usategui, “Measuring stall forces in vivo with optical tweezers through light momentum changes,” in *Proceedings of SPIE*, 2011, vol. 8097, pp. 809726-809726–10.

- J. Mas, A. Farré, J. Sancho-Parramon, E. Martín-Badosa, and M. Montes-Usategui, “Force measurements with optical tweezers inside living cells,” in Proceedings of SPIE - The International Society for Optical Engineering, 2014, vol. 9164, p. 91640U.
- A. Farré, J. Mas, F. Marsà, F. Català, J. Sancho-Parramon, E. Martín-Badosa, and M. Montes-Usategui, “Force measurements in complex samples with optical tweezers,” in Optical Trapping Applications, OTA 2015, 2015.

Book chapters

- C. M. Ritter, J. Mas, L. Oddershede, K. Berg-Sørensen, “Quantifying force and viscoelasticity inside living cells using an active-passive calibrated optical trap”, in the book edited by A. Gennerich “Optical Tweezers: Methods and Protocols”, Methods in Molecular Biology, 1486, Springer, 2017

Patents

- E. Martín-Badosa, M. Montes-Usategui, A. Farré, and J. Mas, "Method for manipulating microscopic samples and measuring forces acting thereon," Patent (application ES 201130783) (2011).

Bibliography

- [1] K. C. Neuman and S. M. Block, “Optical trapping,” *Review of Scientific Instruments*, vol. 75, no. 9, pp. 2787–2809, 2004.
- [2] S. Gross, “Application of optical traps In Vivo,” *Methods in enzymology*, vol. 361, no. 1998, pp. 162–174, 2003. [Online]. Available: <http://linkinghub.elsevier.com/retrieve/pii/S0076687903610104>
- [3] M. Fischer and K. Berg-Sørensen, “Calibration of trapping force and response function of optical tweezers in viscoelastic media,” *Journal of Optics A: Pure and Applied Optics*, vol. 9, no. 8, pp. S239–S250, aug 2007. [Online]. Available: <http://stacks.iop.org/1464-4258/9/i=8/a=S18?key=crossref.eacad321af850272c18f0adbdb7bebf4>
- [4] M. Fischer, A. C. Richardson, S. N. S. Reihani, L. B. Oddershede, and K. Berg-Solžrensen, “Active-passive calibration of optical tweezers in viscoelastic media,” *Review of Scientific Instruments*, vol. 81, no. 1, p. 015103, jan 2010. [Online]. Available: <http://www.ncbi.nlm.nih.gov/pubmed/20113125http://scitation.aip.org/content/aip/journal/rsi/81/1/10.1063/1.3280222>
- [5] S. B. Smith, Y. Cui, and C. Bustamante, “Optical-trap force transducer that operates by direct measurement of light momentum.” *Methods in enzymology*, vol. 361, no. 1994, pp. 134–62, jan 2003. [Online]. Available: <http://www.ncbi.nlm.nih.gov/pubmed/12624910>
- [6] A. Farré and M. Montes-Usategui, “A force detection technique for single-beam optical traps based on direct measurement of light momentum changes.” *Optics express*, vol. 18, no. 11, pp. 11 955–68, may 2010. [Online]. Available: <http://www.ncbi.nlm.nih.gov/pubmed/20589058>
- [7] A. Farré, F. Marsà, and M. Montes-usategui, “Optimized back-focal-plane interferometry directly measures forces of optically trapped particles,” *Optics Express*, vol. 20, no. 11, p. 12270, may 2012. [Online]. Available: <http://www.opticsinfobase.org/abstract.cfm?URI=oe-20-11-12270https://www.osapublishing.org/oe/abstract.cfm?uri=oe-20-11-12270>

- [8] A. Ashkin, "Acceleration and trapping of particles by radiation pressure," *Physical review letters*, vol. 24, no. 4, pp. 156–159, 1970. [Online]. Available: [http://www.uni-ulm.de/fileadmin/website_{_}uni_{_}ulm/nawi.inst.220/lehre/HauptSem_{_}WS2007/1970_{_}ashkin.pdf](http://www.uni-ulm.de/fileadmin/website/_uni/_ulm/nawi.inst.220/lehre/HauptSem_{_}WS2007/1970_{_}ashkin.pdf)
- [9] A. Ashkin, J. M. Dziedzic, J. E. Bjorkholm, and S. Chu, "Observation of a single-beam gradient force optical trap for dielectric particles," *Optics Letters*, vol. 11, no. 5, p. 288, may 1986. [Online]. Available: <https://www.osapublishing.org/abstract.cfm?URI=ol-11-5-288>
- [10] R. J. Hopkins, L. Mitchem, A. D. Ward, and J. P. Reid, "Control and characterisation of a single aerosol droplet in a single-beam gradient-force optical trap," *Physical Chemistry Chemical Physics*, vol. 6, no. 21, p. 4924, 2004.
- [11] J. P. Gordon and A. Ashkin, "MOTION OF ATOMS IN A RADIATION TRAP," *Phys. Rev. A*, vol. 21, no. 5, pp. 1606–1617, 1980.
- [12] D. J. Stevenson, F. Gunn-Moore, and K. Dholakia, "Light forces the pace: optical manipulation for biophotonics." *Journal of biomedical optics*, vol. 15, no. 4, p. 041503, 2010. [Online]. Available: <http://www.ncbi.nlm.nih.gov/pubmed/20799781>
- [13] C. Bustamante, J. C. Macosko, and G. J. Wuite, "Grabbing the cat by the tail: manipulating molecules one by one." *Nature reviews. Molecular cell biology*, vol. 1, no. 2, pp. 130–6, 2000. [Online]. Available: <http://www.ncbi.nlm.nih.gov/pubmed/11253365>
- [14] A. Ashkin, K. Schütze, J. M. Dziedzic, U. Euteneuer, and M. Schliwa, "Force generation of organelle transport measured in vivo by an infrared laser trap." *Nature*, vol. 348, no. 6299, pp. 346–8, nov 1990. [Online]. Available: <http://www.ncbi.nlm.nih.gov/pubmed/2250707>
- [15] S. M. Block, L. S. Goldstein, and B. J. Schnapp, "Bead movement by single kinesin molecules studied with optical tweezers." pp. 348–52, nov 1990. [Online]. Available: <http://www.nature.com/nature/journal/v348/n6299/abs/348348a0.html><http://www.ncbi.nlm.nih.gov/pubmed/2174512><http://www.nature.com/doi/10.1038/348348a0><http://dx.doi.org/10.1038/348348a0>
- [16] J. T. Finer, R. M. Simmons, and J. a. Spudich, "Single myosin molecule mechanics: piconewton forces and nanometre steps," *Nature*, vol. 368, no. 6467, pp. 113–119, mar 1994. [Online]. Available: [http://diyhl.us/{~}bryan/papers2/bodybuilding/Singlemyosinmoleculemechanics-piconewtonforcesandnanometresteps.pdf](http://diyhl.us/~bryan/papers2/bodybuilding/Singlemyosinmoleculemechanics-piconewtonforcesandnanometresteps.pdf)<http://www.nature.com/doi/10.1038/368113a0>
- [17] K. Visscher, M. J. Schnitzer, and S. M. Block, "Single kinesin molecules studied with a molecular force clamp." *Nature*, vol. 400, no. 6740, pp.

- 184–9, 1999. [Online]. Available: <http://www.ncbi.nlm.nih.gov/pubmed/10408448>
- [18] M. S. Kellermayer, S. B. Smith, H. L. Granzier, and C. Bustamante, “Folding-unfolding transitions in single titin molecules characterized with laser tweezers,” *Science (New York, N.Y.)*, vol. 276, no. 5315, pp. 1112–1116, 1997. [Online]. Available: <http://kellermayer{ }1997{ }titin{ }molecular{ }spring.pdf>
- [19] S. Oddos, C. Dunsby, M. a. Purbhoo, A. Chauveau, D. M. Owen, M. a. a. Neil, D. M. Davis, and P. M. W. French, “High-speed high-resolution imaging of intercellular immune synapses using optical tweezers.” *Biophysical journal*, vol. 95, no. 10, pp. L66–8, nov 2008. [Online]. Available: <http://www.pubmedcentral.nih.gov/articlerender.fcgi?artid=2576363&tool=pmcentrez&rendertype=abstract>
- [20] K. C. Neuman and A. Nagy, “Single-molecule force spectroscopy : optical tweezers , magnetic tweezers and atomic force microscopy,” vol. 5, no. 6, pp. 491–505, 2008.
- [21] L. B. Oddershede, “Force probing of individual molecules inside the living cell is now a reality,” *Nature Chemical Biology*, vol. 8, no. 11, pp. 879–886, oct 2012. [Online]. Available: <http://www.ncbi.nlm.nih.gov/pubmed/23076067><http://www.nature.com/doifinder/10.1038/nchembio.1082>
- [22] M. a. Welte, S. P. Gross, M. Postner, S. M. Block, and E. F. Wieschaus, “Developmental Regulation of Vesicle Transport in Drosophila Embryos: Forces and Kinetics,” *Cell*, vol. 92, no. 4, pp. 547–557, feb 1998. [Online]. Available: <http://www.ncbi.nlm.nih.gov/pubmed/9491895><http://linkinghub.elsevier.com/retrieve/pii/S0092867400809472>
- [23] A. Farré, C. López-Quesada, J. Andilla, E. Martín-Badosa, and M. Montes-Usategui, “Holographic optical manipulation of motor-driven membranous structures in living NG-108 cells,” *Optical Engineering*, vol. 49, no. 8, p. 085801, aug 2010. [Online]. Available: <http://opticalengineering.spiedigitallibrary.org/article.aspx?doi=10.1117/1.3475950>
- [24] C. López-Quesada, a. S. Fontaine, a. Farré, M. Joseph, J. Selva, G. Egea, M. D. Ludevid, E. Martín-Badosa, and M. Montes-Usategui, “Artificially-induced organelles are optimal targets for optical trapping experiments in living cells,” *Biomedical Optics Express*, vol. 5, no. 7, p. 1993, may 2014. [Online]. Available: <http://www.opticsinfobase.org/abstract.cfm?URI=boe-5-7-1993>
- [25] A. M. Whited and P. S.-H. Park, “Atomic force microscopy: a multifaceted tool to study membrane proteins and their interactions with ligands.” *Biochimica et biophysica acta*, vol. 1838, no. 1 Pt A, pp. 56–68, 2014.

- [Online]. Available: <http://www.pubmedcentral.nih.gov/articlerender.fcgi?artid=3779510&tool=pmcentrez&rendertype=abstract>
- [26] T. a. Nieminen, V. L. Y. Loke, A. B. Stilgoe, G. Knöner, A. M. Brańczyk, N. R. Heckenberg, and H. Rubinsztein-Dunlop, “Optical tweezers computational toolbox,” *Journal of Optics A: Pure and Applied Optics*, vol. 9, no. 8, pp. S196–S203, aug 2007. [Online]. Available: <http://stacks.iop.org/1464-4258/9/i=8/a=S12?key=crossref.d1eab395deb5f624839dcc58c9c5235b>
- [27] Y. Harada and T. Asakura, “Radiation forces on a dielectric sphere in the Rayleigh scattering regime,” *Optics Communications*, vol. 124, no. 5, pp. 529–541, 1996.
- [28] J. Mas, A. Farre, J. Cuadros, I. Juvells, and A. Carnicer, “Understanding Optical Trapping Phenomena: A Simulation for Undergraduates,” *IEEE Transactions on Education*, vol. 54, no. 1, pp. 133–140, feb 2011. [Online]. Available: <http://ieeexplore.ieee.org/lpdocs/epic03/wrapper.htm?arnumber=5451098>
- [29] A. Ashkin, “Forces of a single-beam gradient laser trap on a dielectric sphere in the ray optics regime,” *Biophysical Journal*, vol. 61, no. 2, pp. 569–582, 1992.
- [30] M. Capitano, G. Romano, R. Ballerini, M. Giuntini, F. S. Pavone, D. Dunlap, and L. Finzi, “Calibration of optical tweezers with differential interference contrast signals,” *Review of Scientific Instruments*, vol. 73, no. 4, p. 1687, 2002. [Online]. Available: <http://link.aip.org/link/RSINAK/v73/i4/p1687/s1&Agg=doi>
- [31] S. F. Tolic-Nožirelykke, E. Schäffer, J. Howard, F. S. Pavone, F. Jüllicher, and H. Flyvbjerg, “Calibration of optical tweezers with positional detection in the back focal plane,” *Review of Scientific Instruments*, vol. 77, no. 10, p. 103101, 2006. [Online]. Available: <http://link.aip.org/link/RSINAK/v77/i10/p103101/s1&Agg=doihttp://scitation.aip.org/content/aip/journal/rsi/77/10/10.1063/1.2356852>
- [32] K. Visscher, S. Gross, and S. Block, “Construction of multiple-beam optical traps with nanometer-resolution position sensing,” *IEEE Journal of Selected Topics in Quantum Electronics*, vol. 2, no. 4, pp. 1066–1076, 1996. [Online]. Available: <http://ieeexplore.ieee.org/lpdocs/epic03/wrapper.htm?arnumber=577338>
- [33] R. M. Simmons, J. T. Finer, S. Chu, and J. a. Spudich, “Quantitative measurements of force and displacement using an optical trap.” *Biophysical journal*, vol. 70, no. 4, pp. 1813–22, apr 1996. [Online]. Available: <http://www.pubmedcentral.nih.gov/articlerender.fcgi?artid=1225151&tool=pmcentrez&rendertype=abstract>

- [34] K. Svoboda and S. M. Block, "Biological applications of optical forces." *Annual review of biophysics and biomolecular structure*, vol. 23, pp. 247–85, jan 1994. [Online]. Available: <http://www.ncbi.nlm.nih.gov/pubmed/7919782>
- [35] K. Berg-Sørensen and H. Flyvbjerg, "Power spectrum analysis for optical tweezers," *Review of Scientific Instruments*, vol. 75, no. 3, p. 594, 2004. [Online]. Available: <http://link.aip.org/link/RSINAK/v75/i3/p594/s1>{&}Agg=doi
- [36] P. a. Sims and X. S. Xie, "Probing Dynein and Kinesin Stepping with Mechanical Manipulation in a Living Cell," *ChemPhysChem*, vol. 10, no. 9-10, pp. 1511–1516, jul 2009. [Online]. Available: <http://www.ncbi.nlm.nih.gov/pubmed/19504528><http://doi.wiley.com/10.1002/cphc.200900113>
- [37] C. Leidel, R. A. Longoria, F. M. Gutierrez, and G. T. Shubeita, "Measuring molecular motor forces in vivo: implications for tug-of-war models of bidirectional transport." *Biophysical journal*, vol. 103, no. 3, pp. 492–500, aug 2012. [Online]. Available: <http://linkinghub.elsevier.com/retrieve/pii/S0006349512007278><http://www.pubmedcentral.nih.gov/articlerender.fcgi?artid=3414874>{&}tool=pmcentrez{&}rendertype=abstract
- [38] G. T. Shubeita, S. L. Tran, J. Xu, M. Vershinin, S. Cermelli, S. L. Cotton, M. a. Welte, and S. P. Gross, "Consequences of motor copy number on the intracellular transport of kinesin-1-driven lipid droplets," *Cell*, vol. 135, no. 6, pp. 1098–107, dec 2008. [Online]. Available: <http://www.pubmedcentral.nih.gov/articlerender.fcgi?artid=2768369>{&}tool=pmcentrez{&}rendertype=abstract
- [39] A. K. Rai, A. Rai, A. J. Ramaiya, R. Jha, and R. Mallik, "Molecular adaptations allow dynein to generate large collective forces inside cells." *Cell*, vol. 152, no. 1-2, pp. 172–82, jan 2013. [Online]. Available: <http://linkinghub.elsevier.com/retrieve/pii/S0092867412014328><http://www.ncbi.nlm.nih.gov/pubmed/23332753>
- [40] J. E. Curtis, B. A. Koss, and D. G. Grier, "Dynamic holographic optical tweezers," *Optics Communications*, vol. 207, no. 1-6, pp. 169–175, 2002.
- [41] J. Mas, M. S. Roth, E. Martín-Badosa, and M. Montes-Usategui, "Adding functionalities to precomputed holograms with random mask multiplexing in holographic optical tweezers," *Applied Optics*, vol. 50, no. 10, p. 1417, mar 2011. [Online]. Available: <http://www.ncbi.nlm.nih.gov/pubmed/21460909><http://www.opticsinfobase.org/abstract.cfm?URI=ao-50-10-1417>
- [42] J. R. Moffitt, Y. R. Chemla, S. B. Smith, and C. Bustamante, "Recent advances in optical tweezers." *Annual review of biochemistry*, vol. 77,

- pp. 205–28, jan 2008. [Online]. Available: <http://www.ncbi.nlm.nih.gov/pubmed/18307407>
- [43] E. A. Abbondanzieri, W. J. Greenleaf, J. W. Shaevitz, R. Landick, and S. M. Block, “Direct observation of base-pair stepping by RNA polymerase,” *Nature*, vol. 438, no. 7067, pp. 460–465, nov 2005. [Online]. Available: <http://www.pubmedcentral.nih.gov/articlerender.fcgi?artid=1356566&tool=pmcentrez&rendertype=abstracthttp://www.nature.com/doifinder/10.1038/nature04268>
- [44] M. C. Noom, B. V. D. Broek, J. V. Mameren, and G. J. L. Wuite, “Visualizing single DNA-bound proteins using DNA as a scanning probe,” vol. 4, no. 12, pp. 1031–1036, 2007.
- [45] M. T. Valentine, N. R. Guydosh, B. Gutiérrez-Medina, A. N. Fehr, J. O. Andreasson, and S. M. Block, “Precision steering of an optical trap by electro-optic deflection,” *Optics Letters*, vol. 33, no. 6, pp. 599–601, 2008. [Online]. Available: [http://ol.osa.org/abstract.cfm?URI=ol-33-6-599\\$delimiter"026E30F\\$nhhttp://www.opticsinfobase.org/DirectPDFAccess/E79B4A93-D80C-39CA-61D71FD866F3441D_{_}154867/ol-33-6-599.pdf?da=1{id=154867{&seq=0{&mobile=no\\$delimiter"026E30F\\$nhhttp://www.opticsinfobase.org/ol/abstract.cfm?uri=ol-33-6-599](http://ol.osa.org/abstract.cfm?URI=ol-33-6-599$delimiter)
- [46] W. H. Guilford, J. A. Tournas, D. Dascalu, and D. S. Watson, “Creating multiple time-shared laser traps with simultaneous displacement detection using digital signal processing hardware,” *Analytical Biochemistry*, vol. 326, no. 2, pp. 153–166, 2004.
- [47] Y. Hayasaki, M. Itoh, T. Yatagai, and N. Nishida, “Nonmechanical optical manipulation of microparticle using spatial light modulator,” *Optical Review*, vol. 6, no. 1, pp. 24–27, 1999. [Online]. Available: <http://www.springerlink.com/index/N734003925391575.pdf>
- [48] D. G. Grier, “A revolution in optical manipulation.” *Nature*, vol. 424, no. 6950, pp. 810–6, aug 2003. [Online]. Available: <http://www.ncbi.nlm.nih.gov/pubmed/12917694>
- [49] J. Shane, R. Serati, H. Masterson, and S. Serati, “A holographic optical tweezers module for the International Space Station,” in *Proc. of SPIE*, K. Dholakia and G. C. Spalding, Eds., vol. 9922, no. 303, sep 2016, p. 992222. [Online]. Available: <http://proceedings.spiedigitallibrary.org/proceeding.aspx?doi=10.1117/12.2238984>
- [50] R. W. Bowman, A. J. Wright, and M. J. Padgett, “An SLM-based Shack-Hartmann wavefront sensor for aberration correction in optical tweezers,” *Journal of Optics*, vol. 12, no. 12, p. 124004, dec 2010. [Online]. Available: <http://stacks.iop.org/2040-8986/12/i=12/a=124004?key=crossref.e1ca45d79a43c4190053589e27b86a1c>

- [51] S. Zwick, T. Haist, Y. Miyamoto, L. He, M. Warber, A. Hermerschmidt, and W. Osten, "Holographic twin traps," *Journal of Optics A: Pure and Applied Optics*, vol. 11, no. 3, p. 034011, mar 2009. [Online]. Available: <http://stacks.iop.org/1464-4258/11/i=3/a=034011?key=crossref.07bff7abda069c80d4e2280d2e02a57e>
- [52] J. A. Grieve, A. Ulcinas, S. Subramanian, G. M. Gibson, M. J. Padgett, D. M. Carberry, and M. J. Miles, "Hands-on with optical tweezers: a multitouch interface for holographic optical trapping," *Optics Express*, vol. 17, no. 5, p. 3595, mar 2009. [Online]. Available: <https://www.osapublishing.org/abstract.cfm?URI=oe-17-5-3595>
- [53] K. Castelino, S. Satyanarayana, and M. Sitti, "Manufacturing of two and three-dimensional micro/nanostructures by integrating optical tweezers with chemical assembly," *Robotica*, vol. 23, no. 4, pp. 435–439, jun 2005. [Online]. Available: http://www.journals.cambridge.org/abstract/_S0263574704000864
- [54] R. E. Holmlin, M. Schiavoni, C. Y. Chen, S. P. Smith, M. G. Prentiss, and G. M. Whitesides, "Light-driven microfabrication: Assembly of multicomponent, three-dimensional structures by using optical tweezers," *Angewandte Chemie - International Edition*, vol. 39, no. 19, pp. 3503–3506, oct 2000. [Online]. Available: <http://www.ncbi.nlm.nih.gov/pubmed/11091403>
- [55] C. M. Creely, G. Volpe, G. P. Singh, M. Soler, and D. V. Petrov, "Raman imaging of floating cells," *Optics Express*, vol. 13, no. 16, p. 6105, aug 2005. [Online]. Available: <http://www.opticsinfobase.org/viewmedia.cfm?uri=oe-13-16-6105&seq=0&html=truehttps://www.osapublishing.org/abstract.cfm?URI=oe-13-16-6105>
- [56] R. Agarwal, K. Ladavac, Y. Roichman, G. Yu, C. M. Lieber, and D. G. Grier, "Manipulation and assembly of nanowires with holographic optical traps," *Optics Express*, vol. 13, no. 22, p. 8906, 2005. [Online]. Available: http://www.opticsinfobase.org/DirectPDFAccess/3EC4E65B-E77C-9AF9-6C86932C1D286475_86057/oe-13-22-8906.pdf?da=1&id=86057&seq=0&mobile=nohttps://www.osapublishing.org/oe/abstract.cfm?uri=oe-13-22-8906
- [57] G. Gibson, D. Carberry, G. Whyte, J. Leach, J. Courtial, J. Jackson, D. Robert, M. Miles, and M. Padgett, "Holographic Assembly Workstation for Optical Manipulation," *Journal of Optics A: Pure and Applied Optics*, vol. 10, no. 044009, pp. 1–6, 2008. [Online]. Available: <http://eprints.gla.ac.uk/32329/>
- [58] E. Martín-Badosa, M. Montes-Usategui, a. Carnicer, J. Andilla, E. Pleguezuelos, and I. Juvells, "Design strategies for optimizing

- holographic optical tweezers set-ups,” *Journal of Optics A: Pure and Applied Optics*, vol. 9, no. 8, pp. S267–S277, aug 2007. [Online]. Available: <http://stacks.iop.org/1464-4258/9/i=8/a=S22?key=crossref.2bd2ab2a268a95bc614f8bfb3a70cc6b>
- [59] R. Di Leonardo, F. Ianni, and G. Ruocco, “Computer generation of optimal holograms for optical trap arrays,” *Optics express*, vol. 15, no. 4, pp. 1913–1922, 2007.
- [60] R. W. Gerchberg, W. O. Saxton, B. R. W. Gerchberg, and W. O. Saxton, “A Practical Algorithm for the Determination of Phase from Image and Diffraction Plane Pictures,” *Optik*, vol. 35, no. 2, pp. 237–246, jun 1972. [Online]. Available: <http://ci.nii.ac.jp/naid/10010556614/http://stacks.iop.org/1063-7818/39/i=6/a=A06?key=crossref.08ac46f1c5d5b70d17b930a813765f44>
- [61] M. Polin, K. Ladavac, S.-H. Lee, Y. Roichman, and D. Grier, “Optimized holographic optical traps.” *Optics express*, vol. 13, no. 15, pp. 5831–45, jul 2005. [Online]. Available: <http://www.ncbi.nlm.nih.gov/pubmed/19498588>
- [62] G. C. Spalding, J. Courtial, and R. Di Leonardo, “Holographic Optical Tweezers,” in *Structured Light and Its Applications*. Elsevier, 2008, pp. 139–168. [Online]. Available: <http://linkinghub.elsevier.com/retrieve/pii/B9780123740274000062>
- [63] M. Reicherter, S. Zwick, T. Haist, C. Kohler, H. Tiziani, and W. Osten, “Fast digital hologram generation and adaptive force measurement in liquid-crystal-display-based holographic tweezers,” *Applied Optics*, vol. 45, no. 5, p. 888, feb 2006. [Online]. Available: <https://www.osapublishing.org/abstract.cfm?URI=ao-45-5-888>
- [64] S. Bianchi and R. Di Leonardo, “Real-time optical micro-manipulation using optimized holograms generated on the GPU,” *Computer Physics Communications*, vol. 181, no. 8, pp. 1444–1448, aug 2010. [Online]. Available: <http://dx.doi.org/10.1016/j.cpc.2010.04.012http://linkinghub.elsevier.com/retrieve/pii/S0010465510001232>
- [65] J. Liesener, M. Reicherter, T. Haist, and H. Tiziani, “Multi-functional optical tweezers using computer-generated holograms,” *Optics Communications*, vol. 185, no. 1-3, pp. 77–82, nov 2000. [Online]. Available: <http://linkinghub.elsevier.com/retrieve/pii/S0030401800009901>
- [66] J. E. Curtis, C. H. Schmitz, and J. P. Spatz, “Symmetry dependence of holograms for optical trapping,” *Optics Letters*, vol. 30, no. 16, p. 2086, aug 2005. [Online]. Available: <https://www.osapublishing.org/abstract.cfm?URI=ol-30-16-2086>

- [67] M. Montes-Usategui, E. Pleguezuelos, J. Andilla, and E. Martín-Badosa, “Fast generation of holographic optical tweezers by random mask encoding of Fourier components,” *Optics Express*, vol. 14, no. 6, p. 2101, mar 2006. [Online]. Available: <https://www.osapublishing.org/abstract.cfm?URI=oe-14-6-2101>
- [68] J. A. Davis and D. M. Cottrell, “Random mask encoding of multiplexed phase-only and binary phase-only filters,” *Optics Letters*, vol. 19, no. 7, p. 496, apr 1994. [Online]. Available: <https://www.osapublishing.org/abstract.cfm?URI=ol-19-7-496>
- [69] Y. F. Dufrêne, E. Evans, A. Engel, J. Helenius, H. E. Gaub, and D. J. Müller, “Five challenges to bringing single-molecule force spectroscopy into living cells.” *Nature methods*, vol. 8, no. 2, pp. 123–7, feb 2011. [Online]. Available: <http://www.nature.com/doi/10.1038/nmeth0211-123><http://www.ncbi.nlm.nih.gov/pubmed/21278722>
- [70] A. G. Hendricks, E. L. F. Holzbaur, and Y. E. Goldman, “Force measurements on cargoes in living cells reveal collective dynamics of microtubule motors.” *Proceedings of the National Academy of Sciences of the United States of America*, vol. 109, no. 45, pp. 18447–52, nov 2012. [Online]. Available: <http://www.ncbi.nlm.nih.gov/pubmed/23091040><http://www.pubmedcentral.nih.gov/articlerender.fcgi?artid=3494964&tool=pmcentrez&rendertype=abstract>
- [71] J. Mas, A. C. Richardson, S. N. S. Reihani, L. B. Oddershede, and K. Berg-Sørensen, “Quantitative determination of optical trapping strength and viscoelastic moduli inside living cells,” *Physical Biology*, vol. 10, no. 4, p. 046006, jul 2013. [Online]. Available: <http://www.ncbi.nlm.nih.gov/pubmed/23820071>
- [72] H. Lee, J. M. Ferrer, F. Nakamura, M. J. Lang, and R. D. Kamm, “Passive and active microrheology for cross-linked F-actin networks in vitro,” *Acta Biomaterialia*, vol. 6, no. 4, pp. 1207–1218, 2010. [Online]. Available: <http://dx.doi.org/10.1016/j.actbio.2009.10.044>
- [73] A. Palmer, T. G. Mason, J. Xu, S. C. Kuo, and D. Wirtz, “Diffusing Wave Spectroscopy Microrheology of Actin Filament Networks,” *Biophysical Journal*, vol. 76, no. 2, pp. 1063–1071, 1999. [Online]. Available: <http://linkinghub.elsevier.com/retrieve/pii/S0006349599772711>
- [74] C. Wilhelm, “Out-of-Equilibrium Microrheology inside Living Cells,” *Physical Review Letters*, vol. 101, no. 2, p. 028101, jul 2008. [Online]. Available: <http://link.aps.org/doi/10.1103/PhysRevLett.101.028101>
- [75] G. Guigas, C. Kalla, and M. Weiss, “Probing the nanoscale viscoelasticity of intracellular fluids in living cells.” *Biophysical journal*, vol. 93, no. 1, pp. 316–23, 2007. [Online].

Available: <http://www.pubmedcentral.nih.gov/articlerender.fcgi?artid=1914431&tool=pmcentrez&rendertype=abstract>

- [76] D. Robert, T. H. Nguyen, F. Gallet, and C. Wilhelm, "In vivo determination of fluctuating forces during endosome trafficking using a combination of active and passive microrheology," *PLoS ONE*, vol. 5, no. 4, 2010.
- [77] I. Tolić-Nørrelykke, E.-L. Munteanu, G. Thon, L. Oddershede, and K. Berg-Sørensen, "Anomalous Diffusion in Living Yeast Cells," *Physical Review Letters*, vol. 93, no. 7, pp. 1–4, aug 2004. [Online]. Available: <http://link.aps.org/doi/10.1103/PhysRevLett.93.078102>
- [78] B. H. Blehm, T. a. Schroer, K. M. Trybus, Y. R. Chemla, and P. R. Selvin, "In vivo optical trapping indicates kinesin's stall force is reduced by dynein during intracellular transport." *Proceedings of the National Academy of Sciences of the United States of America*, no. 8, feb 2013. [Online]. Available: <http://www.ncbi.nlm.nih.gov/pubmed/23404705>
- [79] S. M. Barnett, "Resolution of the Abraham-Minkowski Dilemma," *Physical Review Letters*, vol. 104, no. 7, p. 070401, feb 2010. [Online]. Available: <http://link.aps.org/doi/10.1103/PhysRevLett.104.070401>
- [80] A. Farré, F. Marsà, and M. Montes-Usategui, "Beyond the Hookean Spring Model: Direct Measurement of Optical Forces Through Light Momentum Changes," in *Optical Tweezers: Methods and Protocols, Methods in Molecular Biology*, A. Gennerich, Ed., 2017, vol. 1486, ch. 3.
- [81] J. Mas, A. Farré, C. López-Quesada, X. Fernández, E. Martín-Badosa, M. Montes-Usategui, A. Farre, C. Lopez-Quesada, X. Fernandez, E. Martin-Badosa, and M. Montes-Usategui, "Measuring stall forces in vivo with optical tweezers through light momentum changes," in *Proceedings of SPIE*, vol. 8097, 2011, pp. 809 726–809 726–10. [Online]. Available: <http://link.aip.org/link/PSISDG/v8097/i1/p809726/s1?Agg=doi>
- [82] I. Verdeny, A. Farré, J. Mas, C. López-quesada, E. Martín-Badosa, and M. Montes-Usategui, "Optical trapping: A review of essential concepts," *Óptica Pura y Aplicada*, vol. 44, no. 3, pp. 527–551, 2011. [Online]. Available: <http://www.sedoptica.es/OPA/Pdfs/OPA44-3-527.pdf>
- [83] T. F. Bartsch, R. A. Longoria, E.-L. Florin, and G. T. Shubeita, "Lipid droplets purified from Drosophila embryos as an endogenous handle for precise motor transport measurements." *Biophysical journal*, vol. 105, no. 5, pp. 1182–91, sep 2013. [Online]. Available: <http://dx.doi.org/10.1016/j.bpj.2013.07.026><http://www.sciencedirect.com/science/article/pii/S0006349513008424><http://www.ncbi.nlm.nih.gov/pubmed/24010661>

- [84] H. Turlier, D. A. Fedosov, B. Audoly, T. Auth, N. S. Gov, C. Sykes, J.-F. Joanny, G. Gompper, and T. Betz, “Equilibrium physics breakdown reveals the active nature of red blood cell flickering,” *Nature Physics*, vol. 12, no. 5, pp. 513–519, 2016. [Online]. Available: <http://dx.doi.org/10.1038/nphys3621>
- [85] D. Mizuno, C. Tardin, C. F. Schmidt, and F. C. Mackintosh, “Nonequilibrium mechanics of active cytoskeletal networks.” *Science*, vol. 315, no. 5810, pp. 370–3, 2007. [Online]. Available: <http://www.ncbi.nlm.nih.gov/pubmed/17234946>
- [86] J. Howard, “Molecular motors: structural adaptations to cellular functions.” *Nature*, vol. 389, no. 6651, pp. 561–7, oct 1997. [Online]. Available: <http://www.ncbi.nlm.nih.gov/pubmed/9335494><http://www.nature.com/doi/10.1038/39247>
- [87] M. Schliwa and G. Woehlke, “Molecular motors.” *Nature*, vol. 422, no. 6933, pp. 759–65, apr 2003. [Online]. Available: <http://link.springer.com/content/pdf/10.1007/3-540-29623-9{ }3980>.
<pdfhttp://www.ncbi.nlm.nih.gov/pubmed/12700770>
- [88] R. D. Vale, “The Molecular Motor Toolbox for Intracellular Transport,” *Cell*, vol. 112, no. 4, pp. 467–480, feb 2003. [Online]. Available: <http://linkinghub.elsevier.com/retrieve/pii/S0092867403001119><http://www.sciencedirect.com/science/article/pii/S0092867403001119>
- [89] H. Higuchi and S. A. Endow, “Directionality and processivity of molecular motors,” *Current Opinion in Cell Biology*, vol. 14, no. 1, pp. 50–57, feb 2002. [Online]. Available: <http://linkinghub.elsevier.com/retrieve/pii/S0955067401002939>
- [90] D. J. Sharp, G. C. Rogers, and J. M. Scholey, “Microtubule motors in mitosis.” *Nature*, vol. 407, no. 6800, pp. 41–7, sep 2000. [Online]. Available: <http://www.ncbi.nlm.nih.gov/pubmed/10993066>
- [91] R. D. Vale, “The Way Things Move: Looking Under the Hood of Molecular Motor Proteins,” *Science*, vol. 288, no. 5463, pp. 88–95, apr 2000. [Online]. Available: <http://www.sciencemag.org/cgi/doi/10.1126/science.288.5463.88>
- [92] M. Tominaga, H. Kojima, E. Yokota, H. Orii, R. Nakamori, E. Katayama, M. Anson, T. Shimmen, and K. Oiwa, “Higher plant myosin XI moves processively on actin with 35 nm steps at high velocity.” *The EMBO journal*, vol. 22, no. 6, pp. 1263–72, mar 2003. [Online]. Available: <http://www.pubmedcentral.nih.gov/articlerender.fcgi?artid=151065{&}tool=pmcentrez{&}rendertype=abstract>
- [93] V. Levi, V. I. Gelfand, A. S. Serpinskaya, and E. Gratton, “Melanosomes transported by myosin-V in *Xenopus melanophores* perform slow 35 nm

- steps.” *Biophysical journal*, vol. 90, no. 1, pp. L07–9, jan 2006. [Online]. Available: <http://www.pubmedcentral.nih.gov/articlerender.fcgi?artid=1367043&tool=pmcentrez&rendertype=abstract>
- [94] N. Hirokawa and R. Takemura, “Molecular motors and mechanisms of directional transport in neurons.” *Nature reviews. Neuroscience*, vol. 6, no. 3, pp. 201–14, mar 2005. [Online]. Available: <http://www.ncbi.nlm.nih.gov/pubmed/15711600>
- [95] A. Gennerich and R. D. Vale, “Walking the walk: how kinesin and dynein coordinate their steps.” *Current opinion in cell biology*, vol. 21, no. 1, pp. 59–67, feb 2009. [Online]. Available: <http://www.pubmedcentral.nih.gov/articlerender.fcgi?artid=2668149&tool=pmcentrez&rendertype=abstract>
- [96] K. Svoboda, C. F. Schmidt, B. J. Schnapp, and S. M. Block, “Direct observation of kinesin stepping by optical trapping interferometry.” *Nature*, vol. 365, no. 6448, pp. 721–7, oct 1993. [Online]. Available: <http://www.ncbi.nlm.nih.gov/pubmed/8413650>
- [97] K. Svoboda and S. M. Block, “Force and velocity measured for single kinesin molecules.” *Cell*, vol. 77, no. 5, pp. 773–84, jun 1994. [Online]. Available: <http://www.ncbi.nlm.nih.gov/pubmed/8205624>
- [98] W. J. Walter, B. Brenner, and W. Steffen, “Cytoplasmic dynein is not a conventional processive motor.” *Journal of structural biology*, vol. 170, no. 2, pp. 266–9, may 2010. [Online]. Available: <http://www.ncbi.nlm.nih.gov/pubmed/19961937>
- [99] R. Mallik, B. C. Carter, S. a. Lex, S. J. King, and S. P. Gross, “Cytoplasmic dynein functions as a gear in response to load.” *Nature*, vol. 427, no. 6975, pp. 649–52, feb 2004. [Online]. Available: <http://www.ncbi.nlm.nih.gov/pubmed/14961123>
- [100] S. Toba, T. M. Watanabe, L. Yamaguchi-Okimoto, Y. Y. Toyoshima, and H. Higuchi, “Overlapping hand-over-hand mechanism of single molecular motility of cytoplasmic dynein,” *Proceedings of the National Academy of Sciences*, vol. 103, no. 15, pp. 5741–5745, 2006. [Online]. Available: <http://www.pnas.org/cgi/doi/10.1073/pnas.0508511103>
- [101] A. Gennerich, A. P. Carter, S. L. Reck-Peterson, and R. D. Vale, “Force-induced bidirectional stepping of cytoplasmic dynein.” *Cell*, vol. 131, no. 5, pp. 952–65, nov 2007. [Online]. Available: <http://www.ncbi.nlm.nih.gov/pubmed/18045537><http://www.pubmedcentral.nih.gov/articlerender.fcgi?artid=2851641&tool=pmcentrez&rendertype=abstract>
- [102] J. D. Alper, M. Tovar, and J. Howard, “Displacement-weighted velocity analysis of gliding assays reveals that *Chlamydomonas*

- axonemal dynein preferentially moves conspecific microtubules." *Biophysical journal*, vol. 104, no. 9, pp. 1989–98, may 2013. [Online]. Available: <http://www.pubmedcentral.nih.gov/articlerender.fcgi?artid=3647177&tool=pmcentrez&rendertype=abstract>
- [103] a. Ishijima, H. Kojima, H. Higuchi, Y. Harada, T. Funatsu, and T. Yanagida, "Multiple- and single-molecule analysis of the actomyosin motor by nanometer-piconewton manipulation with a microneedle: unitary steps and forces." *Biophysical journal*, vol. 70, no. 1, pp. 383–400, jan 1996. [Online]. Available: <http://www.pubmedcentral.nih.gov/articlerender.fcgi?artid=1224937&tool=pmcentrez&rendertype=abstract>
- [104] K. Barlan, M. J. Rossow, and V. I. Gelfand, "The journey of the organelle: teamwork and regulation in intracellular transport." *Current opinion in cell biology*, vol. 25, no. 4, pp. 483–8, aug 2013. [Online]. Available: <http://www.ncbi.nlm.nih.gov/pubmed/23510681>
- [105] J. R. Kardon and R. D. Vale, "Regulators of the cytoplasmic dynein motor." *Nature reviews. Molecular cell biology*, vol. 10, no. 12, pp. 854–65, dec 2009. [Online]. Available: <http://www.ncbi.nlm.nih.gov/pubmed/19935668><http://www.pubmedcentral.nih.gov/articlerender.fcgi?artid=3394690&tool=pmcentrez&rendertype=abstract>
- [106] J. Huang, A. J. Roberts, A. E. Leschziner, and S. L. Reck-Peterson, "Lis1 acts as a "clutch" between the ATPase and microtubule-binding domains of the dynein motor." *Cell*, vol. 150, no. 5, pp. 975–86, aug 2012. [Online]. Available: <http://www.pubmedcentral.nih.gov/articlerender.fcgi?artid=3438448&tool=pmcentrez&rendertype=abstract>
- [107] V. Belyy, M. A. Schlager, H. Foster, A. E. Reimer, A. P. Carter, and A. Yildiz, "The mammalian dynein-actin complex is a strong opponent to kinesin in a tug-of-war competition," *Nature Cell Biology*, no. February, 2016. [Online]. Available: <http://www.ncbi.nlm.nih.gov/pubmed/27454819><http://www.nature.com/doi/10.1038/ncb3393>
- [108] S. Reck-Peterson, R. D. Vale, and A. Gennerich, "Motile properties of cytoplasmic dynein," in *Handbook of dynein*, K. Hirose and L. A. Amos, Eds. Pan Stanford Publishing, 2011, ch. 8, pp. 145–172. [Online]. Available: www.panstanford.com/files/publication/{}_pdf/MotilePropertiesOfCytoplasmicDynein.pdf
- [109] J. Gagliano, M. Walb, B. Blaker, J. C. Macosko, and G. Holzwarth, "Kinesin velocity increases with the number of motors pulling against viscoelastic drag." *European biophysics journal : EBJ*, vol. 39, no. 5, pp. 801–13, apr 2010. [Online]. Available: <http://www.ncbi.nlm.nih.gov/pubmed/19921171>

- [110] D. St Johnston, "Counting motors by force." *Cell*, vol. 135, no. 6, pp. 1000–1, dec 2008. [Online]. Available: <http://www.ncbi.nlm.nih.gov/pubmed/19070567>
- [111] D. K. Jamison, J. W. Driver, A. R. Rogers, P. E. Constantinou, and M. R. Diehl, "Two kinesins transport cargo primarily via the action of one motor: implications for intracellular transport." *Biophysical journal*, vol. 99, no. 9, pp. 2967–77, nov 2010. [Online]. Available: <http://www.pubmedcentral.nih.gov/articlerender.fcgi?artid=2966006&tool=pmcentrez&rendertype=abstract>
- [112] M. Vershinin, B. C. Carter, D. S. Razafsky, S. J. King, and S. P. Gross, "Multiple-motor based transport and its regulation by Tau." *Proceedings of the National Academy of Sciences of the United States of America*, vol. 104, no. 1, pp. 87–92, jan 2007. [Online]. Available: <http://www.pubmedcentral.nih.gov/articlerender.fcgi?artid=1765483&tool=pmcentrez&rendertype=abstract>
- [113] A. Kunwar, M. Vershinin, J. Xu, and S. P. Gross, "Stepping, strain gating, and an unexpected force-velocity curve for multiple-motor-based transport." *Current biology : CB*, vol. 18, no. 16, pp. 1173–83, aug 2008. [Online]. Available: <http://www.ncbi.nlm.nih.gov/pubmed/18701289http://www.pubmedcentral.nih.gov/articlerender.fcgi?artid=3385514&tool=pmcentrez&rendertype=abstract>
- [114] J. Xu, Z. Shu, S. J. King, and S. P. Gross, "Tuning multiple motor travel via single motor velocity." *Traffic (Copenhagen, Denmark)*, vol. 13, no. 9, pp. 1198–205, sep 2012. [Online]. Available: <http://www.pubmedcentral.nih.gov/articlerender.fcgi?artid=3418377&tool=pmcentrez&rendertype=abstract>
- [115] C. Kural, H. Kim, S. Syed, G. Goshima, V. I. Gelfand, and P. R. Selvin, "Kinesin and dynein move a peroxisome in vivo: a tug-of-war or coordinated movement?" *Science (New York, N.Y.)*, vol. 308, no. 5727, pp. 1469–72, jun 2005. [Online]. Available: <http://www.ncbi.nlm.nih.gov/pubmed/15817813http://www.sciencemag.org/cgi/doi/10.1126/science.1108408>
- [116] S. P. Gross, M. a. Welte, S. M. Block, and E. F. Wieschaus, "Dynein-mediated cargo transport in vivo. A switch controls travel distance." *The Journal of cell biology*, vol. 148, no. 5, pp. 945–56, mar 2000. [Online]. Available: <http://www.pubmedcentral.nih.gov/articlerender.fcgi?artid=2174539&tool=pmcentrez&rendertype=abstract>
- [117] A. G. Hendricks, E. Perlson, J. L. Ross, H. W. Schroeder, M. Tokito, and E. L. F. Holzbaur, "Motor coordination via a tug-of-war mechanism drives bidirectional vesicle transport." *Current biology : CB*, vol. 20, no. 8, pp. 697–702, apr 2010. [Online].

Available: <http://www.pubmedcentral.nih.gov/articlerender.fcgi?artid=2908734&tool=pmcentrez&rendertype=abstract>

- [118] V. Soppina, A. K. Rai, A. J. Ramaiya, P. Barak, and R. Mallik, "Tug-of-war between dissimilar teams of microtubule motors regulates transport and fission of endosomes." *Proceedings of the National Academy of Sciences of the United States of America*, vol. 106, no. 46, pp. 19381–6, nov 2009. [Online]. Available: <http://www.pubmedcentral.nih.gov/articlerender.fcgi?artid=2770008&tool=pmcentrez&rendertype=abstract>
- [119] A. Kunwar, S. K. Tripathy, J. Xu, M. K. Mattson, P. Anand, R. Sigua, M. Vershinin, R. J. McKenney, C. C. Yu, A. Mogilner, and S. P. Gross, "Mechanical stochastic tug-of-war models cannot explain bidirectional lipid-droplet transport." *Proceedings of the National Academy of Sciences of the United States of America*, vol. 108, no. 47, pp. 18960–5, nov 2011. [Online]. Available: <http://www.pnas.org/content/early/2011/11/07/1107841108.short><http://www.pubmedcentral.nih.gov/articlerender.fcgi?artid=3223464&tool=pmcentrez&rendertype=abstract>
- [120] S. M. Block, C. L. Asbury, J. W. Shaevitz, and M. J. Lang, "Probing the kinesin reaction cycle with a 2D optical force clamp." *Proceedings of the National Academy of Sciences of the United States of America*, vol. 100, no. 5, pp. 2351–6, mar 2003. [Online]. Available: <http://www.pubmedcentral.nih.gov/articlerender.fcgi?artid=151344&tool=pmcentrez&rendertype=abstract><http://www.ncbi.nlm.nih.gov/pubmed/12591957><http://www.pubmedcentral.nih.gov/articlerender.fcgi?artid=PMC151344>
- [121] C. Veigel and C. F. Schmidt, "Moving into the cell: single-molecule studies of molecular motors in complex environments." *Nature reviews. Molecular cell biology*, vol. 12, no. 3, pp. 163–76, mar 2011. [Online]. Available: <http://www.nature.com/doi/10.1038/nrm3062><http://www.ncbi.nlm.nih.gov/pubmed/21326200>
- [122] E. L. F. Holzbaur and Y. E. Goldman, "Coordination of molecular motors: from in vitro assays to intracellular dynamics." *Current opinion in cell biology*, vol. 22, no. 1, pp. 4–13, feb 2010. [Online]. Available: <http://www.pubmedcentral.nih.gov/articlerender.fcgi?artid=2846361&tool=pmcentrez&rendertype=abstract><http://www.ncbi.nlm.nih.gov/pubmed/20102789><http://www.pubmedcentral.nih.gov/articlerender.fcgi?artid=PMC2846361>
- [123] Y. Liu, D. K. Cheng, G. J. Sonek, M. W. Berns, C. F. Chapman, and B. J. Tromberg, "Evidence for localized cell heating induced by infrared optical tweezers." *Biophysical journal*, vol. 68, no. 5, pp. 2137–44, may 1995. [Online]. Available: <http://www.pubmedcentral.nih.gov/articlerender.fcgi?artid=1282119&tool=pmcentrez&rendertype=abstract>

- [124] N. Shekhar, S. Neelam, J. Wu, A. J. Ladd, R. B. Dickinson, and T. P. Lele, "Fluctuating Motor Forces Bend Growing Microtubules." *Cellular and molecular bioengineering*, vol. 6, no. 2, pp. 120–129, jun 2013. [Online]. Available: <http://www.pubmedcentral.nih.gov/articlerender.fcgi?artid=3768200&tool=pmcentrez&rendertype=abstract>
- [125] J. Wu, G. Misra, R. J. Russell, A. J. C. Ladd, T. P. Lele, and R. B. Dickinson, "Effects of dynein on microtubule mechanics and centrosome positioning." *Molecular biology of the cell*, vol. 22, no. 24, pp. 4834–41, dec 2011. [Online]. Available: <http://www.pubmedcentral.nih.gov/articlerender.fcgi?artid=3237626&tool=pmcentrez&rendertype=abstract>
- [126] D. Craig, A. McDonald, M. Mazilu, H. Rendall, F. Gunn-Moore, and K. Dholakia, "Enhanced Optical Manipulation of Cells Using Antireflection Coated Microparticles," *ACS Photonics*, vol. 2, no. 10, pp. 1403–1409, 2015.
- [127] J. Ferraro-Gideon, R. Sheykhan, Q. Zhu, M. L. Duquette, M. W. Berns, and A. Forer, "Measurements of forces produced by the mitotic spindle using optical tweezers." *Molecular biology of the cell*, vol. 24, pp. 1375–86, 2013. [Online]. Available: <http://www.pubmedcentral.nih.gov/articlerender.fcgi?artid=3639049&tool=pmcentrez&rendertype=abstract>
- [128] K. Norregaard, L. Jauffred, K. Berg-Sørensen, and L. B. Oddershede, "Optical manipulation of single molecules in the living cell." *Physical chemistry chemical physics : PCCP*, vol. 16, no. 25, pp. 12614–24, jul 2014. [Online]. Available: <http://www.ncbi.nlm.nih.gov/pubmed/24651890>